
UNIVERSITÀ DI TRENTO
Department of Industrial Engineering

XXXVII cycle

Doctoral School in Materials, Mechatronics and System Engineering

# Cyber-physical systems to monitor the efficiency and sustainability of human-centric manufacturing systems

**Andrea Sbaragli**

January 2025

# Cyber-physical systems to monitor the efficiency and sustainability of human-centric manufacturing systems

Andrea Sbaragli

Email: andrea.sbaragli@unitn.it

| Approved by: | Ph.D. Commission: |
|---|---|
| Prof. Francesco Pilati, Supervisor<br>Dep. of Industrial Engineering<br>*University of Trento* | Prof. Matteo Brunelli<br>Dep. of Industrial Engineering<br>*University of Trento* |
| Prof. Ejsmont, Krzysztof, Reviewer<br>Fac. of Mechanical and Industrial Engineering<br>*Warsaw University of Technology* | Prof. Alexandra Lagorio<br>Dep. of Management, information and Production Engineering<br>*University of Bergamo* |
| Prof. Xi Wang, Reviewer<br>Dep. of Production Engineering<br>*KTH Royal Institute of Technology* | Prof. Sebastian Thiede<br>Dep. of Design, Production and Management<br>*University of Twente* |

University of Trento

Department of Industrial Engineering

January 2025

**University of Trento - Department of Industrial Engineering**

**Doctoral Thesis**

**Andrea Sbaragli - January 2025**
**Published in Trento (Italy) - by University of Trento**

I would like start this work by quoting *Dante's Divina Commedia*. You may wonder why I cite these excerpts, among the others I want to contrast the interpretation process with an exact science such as engineering. You will not find any reference to the *Paradiso* because satisfaction is a complex and floating achievement.

*"Di fuor dorate son, sì ch'elli abbaglia;*
*ma dentro tutte piombo, e gravi tanto,*
*che Federigo le mettea di paglia."*
(Inferno, XXIII, 63-66)

*"E tutti li altri che tu vedi qui,*
*seminator di scandalo e di scisma*
*fuor vivi, e però son fessi così."*
(Inferno, XXVIII, 31-36)

*"e disse: «Il temporal foco e l'etterno*
*veduto hai, figlio; e se' venuto in parte*
*dov'io per me più oltre non discerno.»"*
(Purgatorio, XXVII, 127-129)

## Copyright Notice

The content of this thesis is the result of the author's original research work. Permission to include the following published material for non-commercial purposes is granted by the publishers' copyright policy. The published works are cited in the bibliography and are listed below.

- Tomelleri, F., **Sbaragli, A.**, Picariello, F., & Pilati, F. (2024). Digital ergonomic assessment to enhance the physical resilience of human-centric manufacturing systems in Industry 5.0. Journal of Manufacturing Systems, 77, 246-265.
- Pilati, F., **Sbaragli, A.**, Ruppert, T., & Abonyi, J. (2024). Goal-oriented clustering algorithm to monitor the efficiency of logistic processes through real-time locating systems. International Journal of Computer Integrated Manufacturing, 1-17.
- Pilati, F., & **Sbaragli, A.** (2023). Learning human-process interaction in manual manufacturing job shops through indoor positioning systems. Computers in Industry, 151, 103984.
- Pilati, F., **Sbaragli, A.**, Papini, G. P. R., & Capuccini, P. (2023, June). An Artificial Neural Network Architecture to Classify Workers' Operations in Manual Production Processes. In International Conference on Flexible Automation and Intelligent Manufacturing (pp. 805-812). Cham: Springer Nature Switzerland.
- Wolf, M., Rantschl, M., Auberger, E., Preising, H., **Sbaragli, A.**, Pilati, F., & Ramsauer, C. (2022). Real time locating systems for human centered production planning and monitoring. IFAC-PapersOnLine, 55(2), 366-371.

## Material Submitted for Publication

This thesis contains material that is currently submitted for publication.

- **Sbaragli, A.**, Ghafoorpoor Yazdi, P., Thiede, S., Pilati, F. A cyber-physical architecture to monitor human-centric reconfigurable manufacturing systems. Journal of Intelligent Manufacturing, 3rd round of reviews ongoing.

# Abstract

The manufacturing domain has been experiencing several revolutions over the years that have been shaping not only the design and management of processes but also their core drivers and value propositions. Industry 4.0 unleashes many enabling technologies such as the Internet of Things sensors and machine learning algorithms to boost industries' productivity through data-driven process monitoring, rather than relying on operation manager experience. However, this fourth revolution does not set as strategic goals sustainability drivers (e.g., social and environmental) triggered by external forces that undermine modern societies. European policymakers address this structural limitation by defining the Industry 5.0 paradigm focused on human-centric and sustainable value creations.

In this fast-paced landscape, this doctoral thesis targets the limitations of Industry 4.0 related contributions and defines three research questions to demonstrate the competitive advantages in designing cyber-physical systems to monitor the efficiency and sustainability of human-centric manufacturing environments. The human-centricity is an important feature of this work because, despite the rise of automation, workers represent a strategic and fragile resource in industrial plants. Therefore, Internet of Things technologies are leveraged to achieve a digital representation of workers. The acquired measurements are fed into computational algorithms to appreciate data-driven managerial insights based on the returned Key Performance and Risk indicators. The contributions of this thesis can be conceptually divided into two separate streams.

The first demonstrates the relevance of enhancing the operational visibility of in-plant operations by exploiting Real Time Locating Systems acquisition layers. Although this technology indoor locates whichever (manufacturing) entity and asset in a defined coverage area, the returned workers' positions fail to evaluate systems' performances and sustainability. For this purpose, density-based machine learning algorithms and neural networks are introduced and validated to embed operational metrics into Decision Support Systems. Multidimensional managerial insights prove the consistency of this methodology in three different manufacturing environments. Considering production settings, managers appreciate the uptimes of workers and resource utilizations while evaluating the layout configurations

and the related efficiency in manual material handling activities. This twofold level of analysis enables to eventually increase in-plant productivity while optimizing workers' efforts in replenishment routes. The logistic investigation offers similar takes by monitoring the Overall Equipment Effectivness of manual forklifts and the distribution of picking/depositing activities in storage areas. Potential inefficiencies provide valid input to optimize the performances while reducing the energy consumption of logistics vehicles.
The second stream focuses on workers' physical resilience during task executions. To achieve this purpose, ergonomic indices are largely adopted to mitigate work-related musculoskeletal disorders in the workforce. The European Assembly Worksheet screening tool is the most complete one focusing on several parameters ranging from working postures to exterted forces. The developed cyber-physical system mirrors in digital spaces workers' operations through a multi-device acquisition layer. While a four-channel surface ElectroMyoGraphy and a network of markerless cameras acquire muscular contractions in upper limbs and body joints, a radio-frequency-based smart glove detects process interactions such as tool usages and component pickings and thus segments production activities. These digital measurements are fed into computational algorithms to automate the mentioned ergonomic assessment. The experimental campaign validates the proposed cyber-physical systems and draws several managerial insights. For instance, strong bending postures may highlight a poor workplace design suggesting the need of self-adjustable workstations to accommodate a diverse workforce. At the same time, worrisome exerted forces could require line rebalancing to fairly redistribute muscular activity rates among operators.
In summary, this thesis represents a significant advancement in digital manufacturing, offering ready-to-deploy systems while outlining future research opportunities and applications.

# Contents

# List of Figures

# List of Tables

# List of Abbreviations

| | |
|---|---|
| **ADC** | Analog-to-Digital Converter |
| **AN** | Anchor |
| **AoA** | Angle of Arrival |
| **CPS** | Cyber-physical systems |
| **CMS** | Cellular Manufacturing Systems |
| **CHI** | Calinski-Harabasz Index |
| **DMS** | Dedicated Manufacturing Systems |
| **DB** | Density Based |
| **DBI** | Davies-Bouldin Index |
| **DSS** | Decision Support System |
| **EAWS** | European Assessment Worksheet |
| **FMS** | Flexible Manufacturing Systems |
| **FP** | False positives |
| **FN** | False negatives |
| **GDPR** | General Data Privacy Regulation |
| **GPS** | Global Positioning System |
| **HPI** | Human process interaction |
| **IoT** | Internet of Things |
| **KPIs** | Key Performing Indicators |
| **KRIs** | Key Risk Indicators |
| **LSTM** | Long Short Term |
| **ML** | Machine Learning |
| **MMH** | Manual Material Handling |
| **MOCAP** | Motion capture |
| **MVC** | Maximal Voluntary Contraction |
| **MQTT** | Message Queuing Telemetry Transport |
| **NIOSH** | National Institute for Occupational Safety and Health |
| **OCRA** | Occupational Repetitive Actions |
| **OWAS** | Ovako Working posutre Assessment |
| **PoE** | Power over Ethernet |
| **P/D** | Picking/deposit |

| | |
|---|---|
| **RFID** | Radio Frequency IDentification |
| **RULA** | Rapid Upper Limb Assessment |
| **REBA** | Rapid Entire Body Assessment |
| **RSSI** | Received Signal Strength Index |
| **RTLS** | Real Time Locating Systems |
| **RMS** | Reconfigurable Manufacturing Systems |
| **sEMG** | Surface Electromyography |
| **SSH** | Secure Shell |
| **SI** | Strain Index |
| **SC** | Snook & Ciriello |
| **SIC** | Silhouette Coefficient |
| **SoM** | System on Module |
| **SKU** | Stock Keeping Unit |
| **ToA** | Time of Arrival |
| **TWR** | Two way ranging |
| **TP** | True positives |
| **TN** | True negatives |
| **TDoA** | Time Difference of Arrival |
| **TKEO** | Teager–Kaiser Energy Operator |
| **UWB** | Ultrawide band |
| **WMSD** | Work-related musculoskeletal disorders |
| **WS** | Workstation |

# List of Symbols

This list of symbols sums lists the indeces and parameters of the following Chapters.

**Indices**

$a, a^{'} = 1, ..., A$: Sub-area of the monitored job-shop or logistic system
$b = 1, 2$: Forklift tag type
$c = 1, 2$: Azure Kinect camera
$f, f^{'}, f^{*} = 1, ..., F$: RTLS and RFID time frame
$g, g^{'} = 1, ..., G$: Vectorial body joint structures
$h = 1, ..., 4$: MMH posture
$i = 1, ..., I$: Sub-trajectory
$j = 1, ..., 25$: Body joint
$k = 1, ..., K$: Industrial entity
$l = 1, ..., L$: Forklift
$m = 1, ..., 4$: Recording channel
$n = 1, ..., N$: sEMG acquisition
$o = 1, ..., O$: Temporal occurence
$p = 1, ..., P$: EAWS body postures
$q = 1, ..., Q$: Azure Kinect recording frame
$r = 1, ..., 22$: Assembly activity
$s = 1, ..., S$: Sliding window
$t = 1, ..., T$: Tool usage
$u, u' = 1, ..., U$: BITalino recording frame
$v = 1, ..., V$: Relevant MMH event
$w = 1, ..., W$: Tagged workers
$z = 1, ..., Z$: Process interaction

**Parameters**

$\alpha$: greatest duration to merge consecutive process interactions
$\beta$: greatest distance between $p^{w,a}_{i,f^*,z}$ and $O^{w,a}_{z+1,i}$ to merge consecutive process interactions'
$\gamma$: greatest distance between process interactions' centers to be merged

$\lambda$: Hyper-parameter to discard tool usage
$\tau$: Hyper-parameter to merge consecutive tool usage
$\pi$: Minimum duration to hold a posture
$\omega$: Threshold for significant MMH events
$\theta_f^w$: angle assumed by the w-th worker during the f-th time frame
$\theta_{i,f',f'+1,z}^{w,a}$: the angle assumed by the w-th worker from the point $f'$ and $f'+1$ in the a-th sub-area
$\theta_{i,f',k,z}^{w,a}$:represents the angle assumed by the same worker and the centroid of the k-th industrial entity
$\Theta_{g-g',k}^{a}$: Angle between the muscular body joint groups $g$ and $g'$ during the $q$-th Kinect frame for the $r$-th assembly activity
$\eta$: Gaussian distributed acceleration noise
$\delta$t: sampling time of RFID and RTLS technologies
$\phi$: greatest distance between the first and last point of process interactions
$ADAFS^r$: Activity-driven Action Force Score for the $r$-th assembly activity
$ADBPS_m^r$: Activity-driven Basic Posture Score for the $m$-th muscle during the $r$-th assembly activity
$ADBPS^r$: Activity-driven Basic Posture Score during the $r$-th assembly activity
$AMMC_{m,s}$: Absolute magnitude of muscular contractions for the $m$-th channel during the $s$-th sliding window
$ADMMHS^r$: Activity-driven Manual Material Handling Score during the $r$-th assembly activity
$AS_f$: Activity-related passive RFID string scanned during the $f$-th frame
$AT_f$: Timestamp related to $AS_f$
$\overline{a}_{z,i}^{w,a}$: : mean acceleration of the z-th process interaction occurred in the i-th sub-trajectory for the w-th worker in the a-th sub-area
$B_k$: geometric centroid of the k-th industrial entity
$C_{z,i}^{w,a}$: z-th process interaction occurred in the i-th sub-trajectory of the w-th operator in the a-th sub-areas
$C_{z,i,b}^{l,a}$: z-th process interaction occurred in the i-th sub-trajectory of the l-th forklift with b-th tag type in the a-th sub-areas
$CL_{j,q}^c$: Confidence level related to $Pos_{j,q}^c$
$d^*$: greatest radius to create $\epsilon$ temporal sequences
$D_p^r$: Duration of holding the $p$-th EAWS posture during the $r$-th assembly activity
$D_{p,o}^r$: Duration of holding the $p$-th EAWS posture for the $o$-th occurrence during the $r$-th assembly activity
$D_m^n$: Duration to achieve the MVC for the $m$-th channel and $n$-th acquisition
$D_m$: Duration to achieve the MVC for the $m$-th channel
$DMMC_{m,s}$: Duration related to the absolute magnitude of muscular contractions for the $m$-th channel during the $s$-th sliding window
$D_v^r$: Duration of the $v$-th manual material handling event during the $r$-th assembly

activity
$DFScore^{r}_{m,s}$: EAWS Duration Force Score for the $m$-th channel during the $s$-th sliding window and $r$-th assembly activity
$Dist^{w,a}_{z,k}$: Euclidean distance from the z-th process interaction to the k-th industrial entity for the w-th worker in the a-th sub-area
$dur^{w,a}_{z,i}$: duration of the z-th process interaction occurred during the i-th sub-trajectory for the w-th worker in the a-th sub-area
$FO^{w,a}_{z,i}$: objective function to assign the z-th process interaction occurred in the i-th sub-trajectory for the w-th worker in the a-th sub-area to the k-th industrial entity
$FScore^{r}_{m,s}$: EAWS Action Force Score for the $m$-th channel during the $s$-th sliding window and $r$-th assembly activity
$F_v$: Repetition rate of the $v$-th material handling event over the entire working cycle
$GAFS$: Global Action Force Score
$GBPS$: Global Basic Posture Score
$GMMHS$: Global Manual Material Handling Score
$L^{w,a}_{f',k}$: orientation during the f-th time frame to the k-th industrial entity for the w-th operator in the a-th sub-area
$L^{w,a}_{z,k}$: final orientation during the z-th process interaction to the k-th industrial entity for the w-th operator in the a-th sub-area
$MA_{m,s}$: Muscular activation for the $m$-th channel during the $s$-th sliding window
$MA^{r}_{m,s}$: Muscular activation for the $m$-th channel during the $s$-th sliding window and $r$-th assembly activity
$MVC^{n}_{m}$: Maximal voluntary contraction for the $m$-th channel and $n$-th acquisition
$MVC_{m}$: Maximal voluntary contraction for the $m$-th channel
$MMHPS^{r}_{h,v}$: EAWS Score related to the $h$-th posture during the $v$-th manual material handling event and $r$-th assembly activity
$MMHPS^{r}_{v}$: EAWS Posture Score during the $v$-th manual material handling event and $r$-th assembly activity
$MMHFS_{v}$: EAWS Score related to $F_v$
$m_D$: distance weight of the objective function
$m_\theta$: orientation weight of the objective function
$MAD^{w}$: median absolute deviation of velocities of the w-th worker
$NPts$: required number of points to create a process interaction
$noise^{n}_{m}$: sEMG acquisition noise in resting scenarios for the $m$-th channel and $n$-th acquisition
$noise_{m}$: sEMG acquisition noise in resting scenarios for the $m$-th channel
$over_{m}$: Duration of overlap of the sliding windows for the $m$-th channel
$O^{w,a}_{z,i} = \{Ox^{w,a}_{z,i}, Oy^{w,a}_{z,i}\}$: 2D center of the z-th process interaction occured in the i-th sub-trajectory for the w-th worker in the a-th sub-area
$O^{l,a}_{z,i,b} = \{Ox^{l,a}_{z,i,b}, Oy^{l,a}_{z,i,b}\}$: 2D center of the z-th process interaction occured in the i-th sub-trajectory for the l-th forklift with b-th tag type in the a-th sub-area

$p_{i,f}^{w,a} = \{px_{i,f}^{w,a}, py_{i,f}^{w,a}, ts_{i,f}^{w,a}\}$: f-th time frame of a spatio-temporal point belonging to the i-th sub-trajectory of the w-th worker in the a-th area
$p_{i,f,b}^{w,a} = \{px_{i,f,b}^{l,a}, py_{i,f,b}^{l,a}, ts_{i,f}, b^{l,a}\}$: f-th time frame of a spatio-temporal point belonging to the i-th sub-trajectory of the l-th forklift with b-th tag type in the a-th area
$p_{i,f,q}^{w,a}$:f-th time frame of a spatio-temporal point belonging to the i-th sub-trajectory and q-th $\epsilon$ temporal sequence of the w-th worker in the a-th area
$p_{i,f,z}^{w,a}$:f-th time frame of a spatio-temporal point belonging to the i-th sub-trajectory and z-th process interaction of the w-th worker in the a-th area
$Pos_{j,q}$: Reconstructed 3D position for the $j$-th body joint during the $q$-th Kinect frame
$Pos_{j,q}^{c}$: 3D body position of the $j$-th body joint during the $q$-th Kinect frame for the $c$-th camera
$S_r$: Passive assembly tag of the $r$-th assembly activity
$S_t$: Passive tool tag of the $t$-th tool usage
$Scan_r$: Scanning list of $AT_f$ belonging to the same $r$-th assembly activity
$Scan_t$: Scanning list of $TT_{f'}$ belonging to the same $t$-th tool usage
$S_{i,q}^{w,a}$: q-th $\epsilon$ temporal sequence occurred in the i-th sub-trajectory for the w-th worker in the a-th sub-area
$T$: set of trajectories recorded
$T^w$: set of trajectories recorded for the w-th worker
$ts_{i,f}^{w,a}$: timestamp of the i-th trajectory during the f-th time frame for the w-th worker in the a-th sub-area
$t_i^{w,a}$: i-th sub-trajectory of the w-th worker in the a-th sub-area
$t_{i,b}^{l,a}$: i-th sub-trajectory of the l-th forklift and b-th tag type in the a-th sub-area
$T_r$: Starting timestamp of the $r$-th assembly activity
$TS_{f'}$: Tool-related passive RFID string scanned during the $f'$-th frame
$Tstart_p^r$: Starting timestamp of $D_p^r$
$Tend_p^r$: Ending timestamp of $D_p^r$
$TT_{f'}$: Timestamp related to $TS_{f'}$
$TTstart_t$: Starting timestamp related to the $t$-th tool usage
$TTend_t$: Ending timestamp related to the $t$-th tool usage
$Tstart_v^r$: Starting timestamp related to the $v$-th manual material handling event
$Tend_v^r$: Ending timestamp related to the $v$-th manual material handling event
$thr_m$: Threshold value for the $m$-th channel
$v^{max}$: greatest expected velocity of human walking
$v_f^{max}$: velocity of the w-th worker during the f-th time frame
$V_{g,q}^r$: Vectorial structure of the $g$-th body joint group during the $q$-th Kinect frame for the $r$-th assembly activity
$\overline{v}_{z,i}^{w,a}$ : mean velocity of the z-th process interaction occurred in the i-th sub-trajectory for the w-th worker in the a-th sub-area
$Wdur_m$: Duration of the overlapping sliding windows for the $m$-th channel
$WS^r$: EAWS Weight Score related to the $r$-th assembly activity

$x_{i,m}$: sEMG during the $i$-th acquisition frame for the $m$-th channel
$x_r$: Binary variable associated with MMH events
$x^w_{f|f-1}$: state of the model during the f-th time frame given the f-1 for the w-th worker
% $VC_m$: Percentage of voluntary contraction for the $m$-th channel
%$VC_{m,s}$: Percentage of voluntary contraction for the $m$-th channel during the $s$-th sliding window
%$VC^r_{m,s}$: Percentage of voluntary contraction for the $m$-th channel during the $s$-th sliding window and $r$-th assembly activity

# Preface

"Listen to me now
I need to let you know
You don't have to go it alone
And it's you when I look in the mirror
And it's you when I don't pick up the phone
Sometimes you can't make it on your own"
*– U2, Sometimes you can't make it on your own, 2004*

This thesis aims to sum up an effort-intense doctoral journey that lasted three years. Coming from a management engineering background, I realized that deploying data-driven solutions requires multi-disciplinary skills (not only) in the digital manufacturing domain. The University of Trento ecosystem turned out an excellent playground to learn new competencies ranging from the deployment of Internet of Things systems to the application of state-of-the-art machine learning algorithms as well as conceptualize and address innovative research questions.
Based on this limited academic background, this work discusses and aims to demonstrate the strategic role of cyber-physical systems in monitoring the operational efficiency and the sustainability of human-centric manufacturing systems. Cyber-physical systems mirror processes functioning in digital environments through a set of enabling technologies and then process data streams with computational algorithms to derive managerial metrics. This information has a pivotal role in eventually optimizing in-plant productivity and increasing the sustainability of human-centric manufacturing systems. The trend of mirroring process executions in digital environments starts with the conceptualization of Industry 4.0 in Germany at Hannover Messe in 2011.Different enabling technologies ranging from computing and automation to the Internet of Things sensors are presented as a necessary condition to boost in-plant performances and thus compete in dynamic and volatile markets.

However, the value-creation of this industrial revolution is believed inadequate after almost 15 years of its conceptualization. Indeed, the recent societal and environmental threats have triggered the definition of the Industry 5.0 paradigm. This revolution exploits the already-established digital technologies to promote resilient and sustainable value creations. Within this ever-evolving societal and manufacturing landscape, the human factor still plays a strategic role despite the progressive adoption of automation in industries. Workers represent the most flexible resource that performs a wide range of value-added activities by interacting with different assets. Therefore, achieving digital representation of the human factor during task executions is a necessary condition for modern manufacturing systems. According to the latest two industrial revolutions, the target of these investigations must ensure desired productivity rates while safeguarding the workforce's physical resilience in a massively aging European population.
This thesis presents four different cyber-physical systems to meet both value-creation of Industry 4.0 and 5.0 while addressing three research questions to advance the knowledge in cyber-physical systems applications. The main thread of these methodologies is to leverage a Pareto approach and thus equip the operator with as few sensors as possible and infer as many metrics as possible to manage these human-centric environments. Among the adopted Internet of Things sensors, Real Time Locating Systems are the most exploited wearable due to the intrinsic value of industrial entities' (e.g., workers and forklifts)indoor locations during process executions. The process of indoor locating industrial entities requires the deployment of a reference anchors' infrastructure that estimates tag-equipped entities. This Internet of Things acquisition layer is validated together with machine learning-based algorithms. These layers leverage both supervised and unsupervised approaches. On one hand, a Long Short Term Memory neural network leverages positioning data due to its superior capabilities in learning time-driven patterns. On the other hand, the Industrial DB scan improves the standard formulation of this density-based algorithm to detect process interactions from workers' positions. In the manufacturing domain, a process interaction occurs whenever workers perform manual activities in industrial entities (e.g., machines and workbenches). Regardless of the computational algorithm, classified outputs are post-processed in Decision Support Systems or dashboards to offer plant multi-criteria decision-making variables. Moreover, these cyber-physical systems are tested and validated in different industrial environments where managerial insights are extensively discussed. Besides the adoption of Real Time Locating Systems, the same methodological approach is adopted to digitize the European Assembly Worksheet. This ergonomic tool evaluates workers' physical resilience by considering different physical features (e.g., posture assumed, carried loads, and exerted forces) throughout its four sections. In particular, this ergonomic tool associates load points with unfavorable physical workload conditions and uses a traffic light scheme to classify risk levels. Based

on this, a digital system exploits three Internet of Things sensors to automate the European Assembly Worksheet assessment instead of relying on time-consuming and commitment-oriented conventional managerial approaches. First, a network of markerless cameras captures the 3D positions of body joints during assembly tasks. Second, four channels of sEMG sensors acquire muscular activations in workers' upper limbs. Third, a wearable Radio Frequency IDentification-based smart glove enables the automatic recognition of components pickings and depositings, and tool usages. The detected process interactions are pivotal information to segment assembly tasks. These data streams are processed by computational algorithms that digitize the first three ergonomic tool sections (i.e., Basic Postures, Action Forces, and Manual Material Handling). Benefitting from the obtained Key Risk Indicators, operation managers analyze the process weaknesses of the considered assembly process in an ergonomic Decision Support System.

To conclude, the final ambitions of this work are multiple. First, it demonstrates that low-cost and human-centric operation monitoring are feasible and the resistance to change should be replaced by the added values of embracing digital transformations. Data-driven decision-making processes are also beneficial to ensure long-term market competitiveness. Indeed, high production flexibilities imposed by modern mass-customized markets further threaten in-plant efficiency and the representativeness of conventional managerial tools. Second, these investigations in addition to validating the methodological approach offer several further research opportunities. I hope these open points are fertile ground to improve the application of human-centric cyber-physical systems in academic and industrial environments. Third and last, I am leaving behind and throughout this work the underlying message that if you do not fit in a social scenario and/or your post-master background does not match your interest there is always room to change.

## Chapter 1

# Introduction

"Imagine no possession
I wonder if you can
No need for greed or hunger
A brotherhood of man"
*– John Lennon, Imagine, 1971*

This first Chapter defines the main thread of this thesis and positions its scientific contributions in the current manufacturing landscape. Starting with industrial paradigms, this work points out the core features and drivers of the fourth industrial revolution. This disruptive paradigm defines several enabling technologies to trigger digital data acquisitions and achieve superior decision-making processes with computational algorithms and/or simulation models [1]. However, the Industry's 4.0 value creation focuses on process efficiencies neglecting the systemic threats that challenge manufacturing environments and on a larger scale modern societies. For this purpose, European policymakers conceptualize the Industry 5.0 paradigm providing a vision for industries to go beyond efficiency and productivity and reinforce the role and contributions of industry to society [2]. This latest industrial revolution complements the previous one by promoting environmentally sustainable, human-centric, and resilient value-creations in manufacturing operations [3]. Subsequently, the investigation is narrowed down to analyze the Real Time Locating Systems (RTLS) as enabling Internet of Things (IoT) technology to monitor the operations of manufacturing assets (e.g., workers and forklifts) based on their time-dependent indoor locations [4]. The discussion highlights the benefits of indoor

localizing industrial entities to enhance process visibility and eventually redesign in-plant operations, besides discussing the most performing communication protocol and available positioning algorithms. The third research area discusses the importance of safeguarding workers' physical resilience based on standardized ergonomic indices. These screening tools evaluate risk degrees to which operators are exposed during production cycles by monitoring a wide spectrum of features ranging from motion profiles to muscular activations [5]. However, their formulations are static, and thus conventional managerial approaches are utterly inadequate for two main points. First, the assessment is strongly affected by evaluators' commitment and experience leading to time-consuming investigations. Second, time aspects are further exacerbated in diversified workforces (e.g., height, gender, etc.) and in mass-customized markets that push companies to offer a wide product portfolio with reduced batch sizes [6]. Therefore, cyber-physical systems (CPS) to automate the development of ergonomic indices are discussed, extensively. Finally, section 1.4 pinpoints multiple research questions that this thesis answers with the ambition to advance CPS applications in manufacturing as well as the outline of this work.

## 1.1 Towards a transformative vision for manufacturing environments

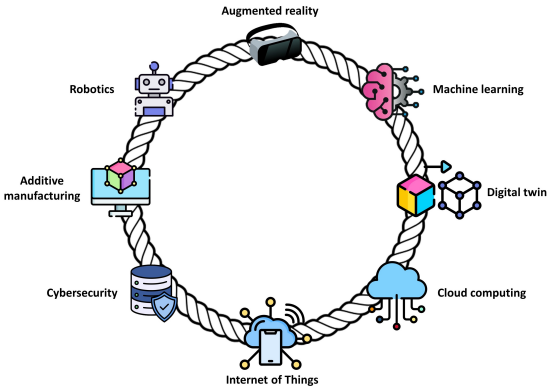


FIGURE 1.1: Industry 4.0 enabling technologies

From the late 18 century to recent days, industrial revolutions have marked significant shifts in manufacturing paradigms, each characterized by groundbreaking innovations [7]. Contrarly to the previous systemic transformations, Industry 4.0

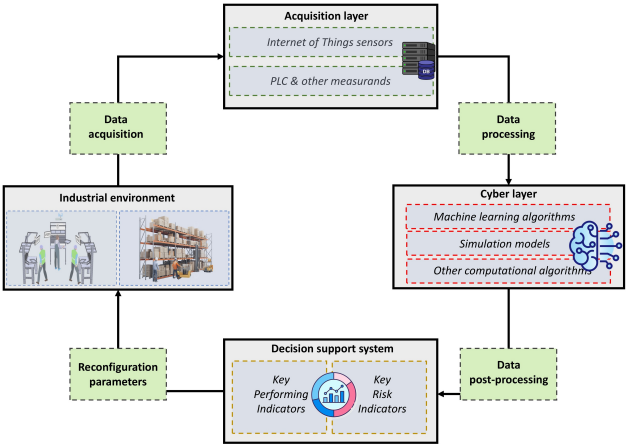


FIGURE 1.2: Structure and data flow of cyber-physical systems

encapsulates several digital technologies to achieve more intelligent and interconnected manufacturing processes [8]. This technology-empowered revolution provides valuable tools to embrace data-driven processes' monitoring and optimizations rather than relying on stakeholders' and shareholders' experience [9]. Fig. 1.1 depicts the enabling technologies of this fourth industrial adapted from [1]. These digital solutions are integrated in order to achieve CPS. The term CPS describes a digital solution that mirrors process executions into virtual environments [10]. A widely adopted schematic representation of CPS is graphically presented in Fig.1.2 [11, 12, 13]. These digital systems are usually broken down into four interconnected layers. First, the industrial environment represents the process under consideration and digitized through the second system's entity (e.g., the acquisition layer). Although a wide range of measurands can acquire manufacturing datastreams, the contributions of this work target human-centric data acquisitions via IoT sensors. Gathered data usually undergoes data processing techniques such as feature extractions and de-noising filters before being fed into cyber layers. This third system entity mines value in raw data by (potentially) leveraging a wide range of algorithms and models. The following Chapters present CPS powered by machine learning (ML) algorithms, therefore similarly to the acquisition layer the following paragraph does not point out the relevant role of the remaining computational algorithms in the digital manufacturing domain. Finally, Decision Support Systems (DSS) or dashboards post-process this information to compute relevant Key Performing Indicators (KPIs) and Key Risk Indicators (KRIs) to eventually reconfigure and optimize process configurations and functioning [14].

IoT devices represent a robust solution to gather distributed data streams from items in the physical world [15]. These measurands can use various types of connections such as Wi-Fi and Bluetooth to share information with desired resolutions with other nodes (e.g., gateways and servers) connected in the same network [16]. Although IoT solutions are deployed in different industrial scenarios to monitor different manufacturing entities, this work targets human-centric data acquisitions. In this regard, the importance of monitoring and assisting the human factor is stressed by Operator 4.0 vision that promotes a human-technology symbiosis [17]. The target is to improve industrial operations performances by empowering workers with IoT technologies and achieving a smarter and more skilled workforce [18]. While [19] draws an Operator 4.0 typology to support the human factor in several use cases, [4] translates these requirements by leveraging RTLS to indoor position workers. Benefitting from these spatio-temporal data, several managerial KPIs on resource utilization and logistic activities can be automated to improve the operational efficiency of human-centric environments [20]. However, the Operator 4.0 represents a high-level framework and thus fall short in discussing the computational algorithms to mine value in acquired data [18, 19]. Computational algorithms are required to handle datasets' high dimensionality and to unlock the potential for processes monitoring and management [16, 21]. One of the most disruptive developments is the deployment of freely available ML algorithms, usually coded in Pytorch[1] and TensorFlow[2] [22]. ML methods have revolutionized the world of data analysis, both by modifying the extraction methods, as well as information processing and interpretation by supporting or even replacing traditional models to perform statistical techniques with automatic sets of general approaches [23, 24]. In short, these intelligent algorithms perform a regression or a classification on output variables given the input features of datasets [22]. While regression determines continuous output values, classification assigns an integer class to input data. Besides this, ML models are distinguished by three different types of learning processes, namely supervised, unsupervised and reinforced. In the first case, labeled data are supplied as input to the system and the output is a mapping of them [25]. However, collecting large amounts of ground truth data may be impractical in industries mainly due to time and privacy constraints [26]. Therefore, unsupervised approaches present several applications in industries due to their ability to handle not labeled data [27]. Among them, density-based clustering methods are increasingly adopted from anomaly detection to operations monitoring [26, 27, 28]. Finally, reinforcement learning deals with dynamic systems where agents learn to make decisions by performing certain actions and receiving rewards or penalties in return. Regardless of the learning process, ML algorithms play a pivotal role in monitoring industrial operations [22, 24]. For instance, [29] demonstrates the potential of Long Short Term Memory (LSTM)

[1]https://pytorch.org/
[2]https://www.tensorflow.org/

based neural networks in preventing machines and components downtimes. Similarly, support vector machines, tree structures, and deep convolutional neural networks are robust methodologies to support workers' quality inspections and reduce in-plant inefficiencies by promptly notifying process deviations [23, 30, 31].
Although the digitalization of industrial operations ensures stable in-plant efficiency, Industry 4.0 as purely purely technology-driven paradigm fails to address the modern societal challenges. Indeed, it presents several limitations from human-centric and environmentally sustainable perspectives. First, maintaining effective and safe collaboration between humans and robots becomes crucial as levels of automation increase. Enabling technologies are required to empower and complement the skills of an aging workforce, with a particular focus on safeguarding operators' well-being during task executions. Second, the vast adoption of IoT technologies is set to increase energy consumption, posing environmental and electronic waste challenges. Besides this, industries and on a larger scale societies are required to reduce their carbon footprint over the years leading to net zero emissions. It is worth noting that environmental sustainability drivers are not key elements of this thesis. Interested readers may appreciate some data-driven investigations in [32, 33]. Addressing these limitations requires a comprehensive approach that considers ethical implications, invests in workforce training, embraces sustainable practices, and fortifies manufacturing systems against potential disruptions achieving resilient environments. In this context, Industry 5.0 leverages the enabling technologies of Industry 4.0 by promoting a human-centric and sustainable value-creation [3, 34]. This industrial revolution prioritizes the resilience of both the workforce and manufacturing systems and defines sustainable practices, focusing on resource efficiency and reduced environmental impact [35]. In particular, Operator 5.0 emerges as the natural evolution of previous technology-driven vision and promotes IoT-based investigations to assist and augment workers' capabilities and skills while safeguarding their self-resilience during value-added activities [3]. Among the different dimensions of self-resilience, physical and occupational health represent pivotal areas of application. Physical resilience is defined as workers' ability to maintain stamina and strength over production cycles [36].
Based on the described drivers that are shaping manufacturing environments, the following two Sections narrow down the discussion to analyze different digital approaches to achieve efficient and socially inclusive manufacturing systems. section 1.2 focuses on the adoption of RTLS to enhance process visibility and traceability. Indeed, this IoT technology indoor locates whichever manufacturing entity enabling to monitor the efficiency and the interdependencies of industrial systems. These KPIs represent pivotal information to achieve sustainable workplaces besides ensuring the desired rate of in-plant performances. Section 1.3 offers an overview of ergonomic indices as well as data-driven investigations to safeguard the well-being of workers during task executions. These risk metrics highlight process weaknesses

TABLE 1.1: RTLS technologies and features

| Protocol | Cost | Coverage | Interference | Accuracy [m] |
|---|---|---|---|---|
| Wi-Fi | Medium/High | High | High | Low/Medium [3-4] |
| Bluetooth | Medium | Low/Medium | Medium/High | Medium [0.5] |
| Infrared | Medium | Low | Low/Medium | Low/Medium |
| **UWB** | **Medium/High** | **Medium/High** | **Low** | **Very High** [0.15-0.5] |
| GPS | High | Outdoor | Not suited for indoors | Low [10-15 ] |

and offer operations supervisors valuable data to eventually redesign industrial workplaces.

## 1.2 Real Time Locating Systems

RTLS represents an active research field with applications in multiple sectors from healthcare to retail [37, 38]. In the digital manufacturing domain, RTLS gained a lot of traction due to their capabilities of indoor localizing different entities (e.g., forklifts and workers) offering valuable inputs to address process complexities and variabilities. Indoor localization is the process of obtaining a device or user location in closed environments and compared to outdoor environments is much more challenging due to noise sources [39, 40]. In short, RTLS networks determine the time-dependent positions of any moving industrial entity equipped with a tag. Tags emit localization signals with a given blink rate to the anchors (ANs) displaced in known positions of the monitored industrial layout. Received signals are transmitted by gateways via LAN or Wi-Fi to a central server that runs positioning algorithms. Tab. 1.1 presents a list of different RTLS technologies along with their technical features [41]. Based on this, the Ultrawide band (UWB) emerges as the best candidate to indoor localize manufacturing entities due to its superior accuracy in industrial environments. Besides a robust operative functioning in non-line-of-sight communications, the UWB-based communication protocol is distinguished by effective multipath resolutions that protect signals from jamming and fading [42]. Interested readers might appreciate a more detailed benchmarking analysis in [43]. As a result, the following chapters leverage UWB-based RTLS acquisition layers to enable CPS to monitor the operational efficiency and sustainability of human-centric manufacturing systems (see Chapters 2, 3, and 4).
The remaining part of this section investigates the RTLS-based positioning algorithms as well as the adoption of locating infrastructure to digitize industrial and human-centric operations (see subsections 1.2.1 and 1.2.2).

### 1.2.1 Positioning algorithms

To implement a UWB-based precise RTLS, different methods are employed to determine the features required by the position estimation algorithm, as depicted in

Fig. 1.3 [43]. Location fingerprinting matches the fingerprint of some location-dependent signal's features. The main challenge of this approach in indoor environments is the signal strength degradation due to reflection, diffraction, and scattering which leads to a laborious and time-consuming calibration process [44]. On the contrary, geometric methods estimate the location of a target based on features like received signal strength index (RSSI), Time of Arrival (ToA), Angle of Arrival (AoA), and Time Difference of Arrival (TDoA) of the signal traveling between the reference ANs and the tag to be localized. ToA and TDoA are the most used ranging techniques. In ToA, two different communication schemes can be exploited: 1) Single-side and 2) double-side two-way ranging (TWR) [45]. With TWR, a synchronization mechanism between nodes is not required. In fact, accurate calibration of the crystal oscillators is sufficient to achieve good accuracy. Similarly, TDoA presents two transmission schemes, namely a centralized and a decentralized TDoA. In the first approach, a tag emits a UWB signal, and the difference in the reception times at the reference ANs side is used to calculate the position of the tag with respect to a reference point [46]. The second transmission scheme mimics a common Global Positioning System (GPS). The ANs continuously broadcast timestamped messages that can be received by listening tags [47]. For the TDoA crystal oscillator trimming is not enough to achieve the desired accuracy. A tighter synchronization between the reference nodes is required.

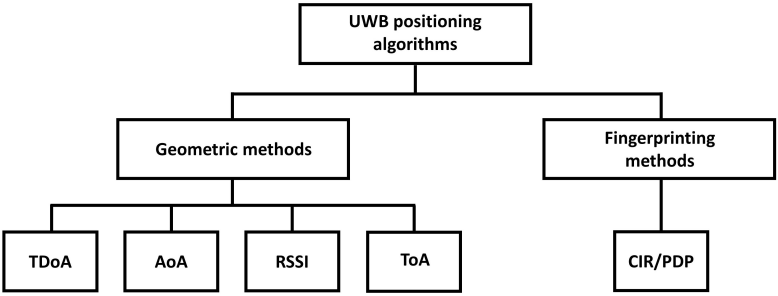


FIGURE 1.3: Summary and comparison of UWB positioning algorithms

### 1.2.2 Industrial use cases

Manufacturing companies are required to constantly monitor their in-plant operational efficiency in order to ensure long-term stability in modern volatile markets. A key challenge is to digitally interconnect automated processes and also involve human operators[41]. The development of RTLS-enabled CPS provides decision-makers with several KPIs to enhance the visibility of human-centric manufacturing

systems [48]. Based on this, several scientific contributions validate data-driven approaches both in production and logistics environments.
Starting to review production settings, [49] automates the Value Stream Map development by tagging workers during task executions. In addition to reducing data collection times, a cyber layer automatically identifies the dynamic human process interactions (HPI) of the monitored system. Upon these outputs, process weaknesses can easily identified and thus addressed to ensure desired performance rates. Another valuable approach is to segment worker activities during working shifts. These insights are strategic to develop KPIs such as average production cycle and traveling times [4]. The monitoring of manual material handling events offers a unique opportunity to analyze the interdependencies of the monitored production environments. This level of detail may eventually trigger re-layout processes to lower traveled distances by operators during the shifts, achieving socially inclusive workplaces based on Industry 5.0 principles [50]. Given RTLS's high degree of flexibility, the scientific research validates this technology by monitoring other industrial assets. For example, [51] demonstrates that tagging products represents a privileged opportunity to reveal weak spots in production lines. This methodology triggers comparisons between the expected throughput times with the actual ones and eventually suggests system modifications such as line rebalancing to increase the performance of assembly operations. A similar approach to maximize in-plant productivity is to indoor position shared manufacturing tools [52, 53]. These CPS offer operations managers two competitive benefits. While workers' searching times can be consistently slashed down, tools' utilization ratio represents a valuable financial metric to adequately design production environment assets capacities.
Despite UWB-based RTLS acquisition layers showing fewer applications in logistic systems, some contributions highlight their potential to improve the operational efficiency of tracked assets [48, 54]. In particular, the vast majority of contributions focus on forklift operations due to their pivotal role during inbound and outbound logistics activities. For instance, [55] automates the spaghetti chart development to monitor forklift operations. Based on this, process bottlenecks are highlighted by monitoring idle and waiting times. Similarly, logistic vehicles are indoor positioned to optimize the routing and the scheduling of picking activities during the order management [56, 57]. The positioning information of industrial entities achieves safer human-centric positioning systems as well. CPS are tested and validated in industrial environments where DSS point out unsafe braking patterns of drivers and calculate optimal routes to avoid congestions and potential collisions [58]. Dynamic speed limits are tested as well [59]. Regardless of the RTLS application area in manufacturing systems, the reviewed CPS are distinguished two structural weaknesses. First, computational units performances in detecting HPIs and the related KPIs are not investigated. Second, the vast majority of algorithms leverage geofencing approaches leading to high exposures in data outliers and reduced capabilities

in detecting recurrent data patterns.
Based on these limitations, this thesis presents three CPSs that couple RTLS-based IoT acquisition layers with ML-driven cyber layers. These investigations leverage both supervised and unsupervised algorithms in different manufacturing environments (e.g., production and logistics). While Chapter 2 and 3 focus on a human-centric job shop and Reconfigurable Manufacturing Systems (RMS), Chapter 4 targets internal logistic systems operations. The common ambition of these contributions is to demonstrate the superior capabilities of these CPS in monitoring manufacturing operations, regardless of the positioned entities (e.g., workers and forklifts) and area of application. Therefore, DSS and industrial dashboards offer multi-criteria decision variables to monitor the efficiency and sustainability of these complex systems

## 1.3 Ergonomic indices

Despite the multitude of industrial revolutions, work-related musculoskeletal disorders (WMSD) still represent a major threat to workers' well-being during task executions [60]. The most frequent disorder targets low back pain whilst more common ones include muscles, tendon sheaths, peripheral nerves, joints, bones, ligaments, etc [5]. As a primary challenge, operations managers are required to design socially inclusive workplaces that safeguard the physical resilience of workers. Ergonomic indices have been massively adopted to highlight process-related weaknesses and lower WMSD, long before the conceptualization of Industry 5.0 [6]. These screening tools evaluate risks involved in work activities, postural loading, effect of vibration, use of tools, coupling, awkward postures, frequency of movements and their duration, work envelopes, and design of ergonomic workstation (WS) [61]. Tab. 1.2 lists the most exploited ergonomic indices in human-centric industrial environments [5, 6, 61].
Although these indices support decision-makers in analyzing process weaknesses, they focus on a limited set of features leading to incomplete ergonomic evaluations. The European Assessment Worksheet (EAWS) fills these limitations by evaluating the physical workload as a function of different manual tasks and hyper-parameters. The EAWS is divided into multiple sections, each focusing on different aspects of physical workload [62]:

- **Section 0 - General**: Provides a comprehensive overview of the identified WS, including overall evaluation, rating of additional physical workload, space for comments and improvements, and consideration of time aspects for repetitive loads of the upper limbs.

- **Section 1 - Basic Postures**: Evaluates static postures and repetitive movements with low physical effort. This section considers symmetrical and asymmetrical postures, and the time spent in these movements is counted to assign a score.
- **Section 2 - Action Forces**: Assesses whole-body forces and hand-finger exertions that exceed the threshold of $30 - 40$ N. Scores are calculated based on the intensity and duration of the force.
- **Section 3 - Manual Materials Handling**: Covers tasks involving loads heavier than $3 - 4$ kg. It evaluates the weight, posture, working conditions, and frequency of handling activities.
- **Section 4 - Upper Limb Load in Repetitive Tasks**: Focuses on the frequency and duration of repetitive upper limb movements, including forces, gripping modes, and postures. This section is aligned with methodologies from other standards like OCRA.

The EAWS assigns load points for unfavorable physical workload conditions and uses a traffic light scheme (e.g., green, yellow, red) to classify the risk levels. This structure helps identify comprehensive ergonomic issues and suggests design improvements. However, besides the limitations of considered physical features, ergonomic analysis implementation and accuracy often rely on conventional managerial approaches, which involve manual data collection and subjective analysis [63]. This can introduce limitations such as human error and time-consuming investigations. To address these limitations, subsection 1.3.1 reviews digital methodologies, where sets of enabling IoT technologies combined with computational algorithms automate ergonomic assessments. This investigation is aligned with Industry 5.0 principles that require socially sustainable value creations in modern manufacturing systems.

### 1.3.1 Digital ergonomic assessments

The digitization of ergonomic indices represents a mature research area and thus indices presented in Tab.1.2 are automated by fusing IoT measurements with computational algorithms. Usually, the index selection is a function of requirements and process weaknesses of final use cases [64, 65]. For instance, [61] leverages a full body motion capture (MOCAP) to compute the Ovako Working posture Assessment (OWAS), Rapid Entire Body Assessment (REBA), and National Institute for Occupational Safety and Health (NIOSH) indices. These KRIs represent pivotal information to eventually redesign the assembly of a water pump and thus safeguard the well-being of workers. Despite several research contributions exploiting IoT-enabled CPS to trigger ergonomic analysis into a diversified workforce, no investigation digitizes multiple EAWS sections [34, 63, 65, 66]. This limitation strongly

affects the validity of ergonomic analysis because the other indices focus on a limited set of parameters (see Tab.1.2). Based on this, it is worth discussing in detail the benefits that decision-makers may appreciate in digitizing all EAWS sections.
The Basic Posture is the most investigated EAWS due to its similar formulation with other tools such as Rapid Upper Limb Assessment (RULA) and REBA [34, 61]. In this regard, MOCAP technologies are extensively adopted to digitize operators' movements during task executions [67]. While IMU-based embedded suits are intrusive and require time-consuming calibration processes, marker-less MOCAP cameras represent a low-invasive and easy-to-deploy solution that suffers from potential body occlusions [34, 68]. Regardless of the hardware selection, algorithms process the acquired 3D body joints and compute the EAWS posture scores to offer valuable insights into potential musculoskeletal disorders of workers, suggesting reconfiguration strategies. [69] demonstrates that these approaches enhance social inclusion and reduce employee turnover.
However, MOCAP data streams fail to evaluate action or exerted forces (e.g., second EAWS section) during manual task executions, leading to limited investigation of workers' physical resilience. While no human-centric CPS have been proposed to digitize this second EAWS section, the relevance of investigating action forces in manual assembly is demonstrated by multiple conventional managerial approaches (e.g., workers' reports or ergonomist evaluations) [70, 71, 72]. For instance, [71] benchmarks Strain Index (SI) and Occupational Repetitive Actions (OCRA) Checklist in 10 manual tasks. At the same time, contributions in other research domains leverage surface ElectroMyoGraphy (sEMG) wearables to monitor muscular strength and activity [73]. The sEMG-based muscular contractions are fed into computational algorithms to detect strain and fatigue [34, 74]. Although these parameters provide valuable insights in designing socially inclusive workspaces, they require extensive datasets and cannot be expressed in EAWS-based force scores. A second approach assesses levels of muscular contractions as a function of the Maximal Voluntary Contraction (MVC), where onsets are detected by evaluating the signal's energy using the Teager–Kaiser Energy Operator (TKEO) [34, 75]. Various protocols have been proposed to isolate muscular groups in isometric contractions [76, 77].
IoT-based CPS to evaluate the third EAWS section (e.g., Manual Material Handling) remains largely unexplored. Similar to the previous EAWS section, the reviewed literature presents Manual Material Handling (MMH) analysis based on conventional approaches and different ergonomic indices (e.g., NIOSH and EAWS) [78, 79]. [79] redesigns three WS based on EAWS scores to lower MMH risks for employees. A successful implementation of this EAWS section strongly relies on an appropriate design of IoT acquisition layers. Indeed, MOCAP cameras and sEMG measurements can be fused to assess postures and exerted forces in carrying loads.
On the contrary, the last EAWS section (e.g., Upper Limb Load in Repetitive Tasks) offers a different picture. Among the others, it ensures a strong focus on hand

movements, exerted forces, and grips during production cycles. Hands' activity recognition is usually assessed using ML-based CPS, where IoT layers leverage different kinds of MOCAP sensors based on the specification of final use cases [80]. However, the identification of motion patterns is not enough to compute the EAWS scores of this section. Additional sensors such as dynamometers and strain gauges are required to complete the analysis and compute EAWS scores [81]. The amount of required measuring nodes also distinguished by poor wearabilities such as dynamometers strongly impacts the validation of this last EAWS section in industrial environments [82].
The limitations of the reviewed contributions offer the unique opportunity to propose an original CPS that by exploiting a Pareto approach digitizes as much as possible the EAWS index by limiting the number of human-centric IoT technologies. For this purpose, the CPS discussed in Chapter 5 leverages a multi-dimensional IoT acquisition layer where MOCAP, RFID and sEMG-based measurements are fed into computational algorithms to derive activity-driven EAWS-based KRIS.

TABLE 1.2: Features and evaluation of ergonomic indeces

| Index | Features | Evaluation |
|---|---|---|
| NIOSH [83] | Load weight limit on gender and spine exerted forces | Lifting & carrying assessments |
| Snook & Ciriello (SC) [84] | Time, distance and objected-driven exerted forces | Pushing & pulling assessment |
| REBA [85] | Categorization of body postures and force, with action levels for assessment | Entire body assessment for dynamic tasks |
| RULA [86] | Categorization of body postures and force, with action levels for assessment | Upper body and limb assessment |
| OCRA [87] | Measures for body posture and force for repetitive tasks | Integrated assessment scores for various types of jobs |
| SI [88] | Combined index of six exposure factors for work tasks | Assessment of risk for distal upper extremity disorder |
| OWAS [89] | Time sampling for body postures and exerted force | Whole body posture recording and analysis |

## 1.4 Research questions & outline

Starting from an overview into current manufacturing trends, this Chapter pointed out some limitations concerning CPS applications to monitor the efficiency and sustainability of human-centric manufacturing systems. Therefore, three research questions (e.g., RQ in the bullet point) are formulated to advance the scientific knowledge as well as (hopefully) scale the adoption rate of CPS for industrial operations monitoring.

- *RQ1 – How can cyber-physical systems powered by Real Time Locating Systems and machine learning algorithms digitize human-centric processes executions?*
- *RQ2 – How can digital ergonomic assessment safeguard workers' physical resilience?*
- *RQ3 – How can key performance and risk indicators be exploited to monitor the operations of industrial environments?*

To adequately address the formulated research questions, the following chapters presents and validate four CPS to monitor the efficiency and well-being of human-centric manufacturing systems.
**Chapter 2** present a CPS that feed the positioning information of workers into the

Industrial Density Based (DB) scan, a novel ML-based clustering algorithm that detects HPI with manufacturing entities over production cycles. A quantitative discussion of this method is outlined in subsection 2.1.2. The obtained output are post-processed in an industrial dashboard that offers operations managers three levels of detail to evaluate the efficiency and the social sustainability of human-centric job shops. This digital systems is validated in an Italian operating industrial environment from two different viewpoint. While section 2.2 investigates the cyber layer performances in detecting process interactions, section 2.3 demonstrates the competitive advantages of monitoring the human-centric job shop through the multidimensional set KPIs.

**Chapter 3** has the ambition to challenge and thus scale the previously validated digital architecture in RMS. Based on the Professor Koren definition in 1999, RMS are *"designed at the outset for rapid change in structure, as well as in hardware and software components to quickly adjust production capacity and functionality within a part family in response to sudden changes in market or in regulatory requirements"* [90]. Targeting the RMS modularity and scalability, a layout and operation-insensitive CPS represent an innovative methodology to segment workers' tasks over working shifts (see section 3.1). Subsection 3.1.1 present the IoT acquisition layer that gather positioning datastreams of WS and operators leveraging an UWB-based RTLS. These spatio-temporal data streams are processed in two steps by a ML-based cyber layer. First, a trained ML-based classifier assigns workers' operations to industrial resources (e.g., WS and storage locations) and detects logistic activities. The Industrial DB scan performances are benchmarked with two supervised algorithms, including a LSTM-based neural network (see subsubsection 3.1.2). Second, resource-specific classifiers are benchmarked to further detail the workers' operations into value-added and non-value-added (see subsubsection 3.1.2). These operator-driven outputs are stored in DSS, where customized callback functions are triggered to develop KPIs to monitor RMS from different viewpoints (see subsection 3.1.3). While performance-oriented metrics evaluate the efficiency of manufacturing systems, another set of metrics evaluates process's interdependencies and social sustainability of production set-ups. The ML-based cyber layer performances are investigated in Section 3.2 with respect to a ground truth labeled dataset involving 40 workers and 7 production set-ups. Finally, Section 3.3 pinpoints the managerial implications of monitoring modular and scalable RMS with the developed CPS.

**Chapter 4** proposes an Industrial DB scan powered CPS to monitor logistic operations during the order management. This third validation of the innovative clustering methods proves its flexibility and elevates it to a pivotal data analysis algorithm for industrial environments. The RTLS-based IoT acquisition layer is designed to acquire the motion patters of forklifts with a cabin and fork tag (see subsection 4.1.1). Subsection 4.1.2 modifies the Industrial DB scan formulation discussed in Chapter 2

to detect value-added forklift operations (e.g., picking and depositing) in warehousing systems. Based on these outputs, a user-friendly Tracking Management System interface develops logistic KPIs to evaluate the efficiency of the vehicles during the order management. Exploiting the advantages of clustering-based methods, the performances of this logistic CPS are validated in a real and operating warehousing system without requiring labeled dataset (see section 4.2). Finally, section 4.3 highlights the benefit for operations supervisor in unleashing digital approaches to monitor interal logistics process executions.

**Chapter 5** fills the limitation of the reviewed ergonomic-centred contributions and proposes a CPS to automate the EAWS assessment. Based on the required operator-centric measurements, subsection 5.1.1 defines a multi-device IoT acquisition layer. While a network of MOCAP cameras and a sEMG-based wearable captures human body joints and muscular contractions of workers during task execution, a Radio Frequency IDentification (RFID) based smart smart glove detects the operators process interactions with strategic manufacturing assets (e.g., storage locations and tools). These data streams are fed into computational algorithms to develop EAWS-informed KRIs, stored in an Ergonomic DSS (see subsections 5.1.2 and 5.1.3). Finally, Section 5.3 discusses the managerial implication in monitoring the physical resilience of workers in assembly processes through the proposed set of KRIs.

Two chapters ends this doctoral thesis. While **Chapter 6** streamlines scientific output and activities conducted during this doctoral journey, **Chapter 7** motivates how this work addresses the formulated research questions and delineates further research opportunities in this digital manufacturing domain.

## Chapter 2

# Digital monitoring of human-centric manufacturing job-shops

"I'm not saying it's your fault
Although you could have done more
Oh you are so naive yet so"
– *The Kooks, Naive, 2006*

Over recent years, manufacturing companies have been facing several disruptions to their in-plant functioning and thus performances. Among the others, mass customization of goods is pushing industrial environments to achieve a wider product portfolio [91]. Consequently, production batch sizes are reduced to meet final customers' requests [92]. This notable market-driven trend requires production environments to constantly monitor in-plant operations to reinforce performances at desired levels.
Based on this, this Chapter proposes a CPS powered by RTLS datastreams and a novel ML-based clustering algorithm. While the locating technology acquires workers' spatio-temporal positions, the density-based method detects HPIs with industrial entities over production cycles. From a manufacturing point of view, an HPI occurs whenever workers perform manual activities in machines or workbenches and pick or deposit materials in stock-keeping units (SKUs) of storage areas. Density-based approaches are widely used in manufacturing due to their ability to process

unlabeled data that shorten CPS deployments [93, 94]. In addition, their quick reconfigurability enables highly customized approaches based on use cases requirements [95]. A stark example is the definition of relevant points of interest (e.g., logistic areas, corridors, SKUs, etc.) to facilitate the detection of specific events or activities [96, 97]. In this domain, several contributions perform activity recognition using DB scan algorithms [98, 99]. However, these formulations may return skewed HPIs detection during production cycles due to two main weaknesses. First, they lack time sensitivity. It is worth noting that workers may visit multiple times the same production and/or storage area in separate temporal instances. A trajectory identification combined with time-driven constraints are required to avoid misclassification of industrial operations. Second, additional merging criteria and related hyper-parameters must mitigate the RTLS measuring error [100, 99]. Therefore, the Industrial DB scan is introduced to address these limitations and thus powers the data mining process of the developed CPS.

## 2.1 Cyber-physical system for human-centric manufacturing job shops

This section represents the original proposal of this Chapter presenting a CPS to monitor the efficiency and social sustainability of manufacturing job shops. The digital system constitute of four layers besides the human-centric environment under analysis (see Fig. 2.1). First, the General Data Privacy Regulation (GDPR)-compliant IoT acquisition layer tags industrial workers through an UWB-based RTLS to anonymously acquire workers' trajectories during the working shift. Second, a ML-based cyber layer leverages spatio-temporal and manufacturing systems data to detect HPIs with strategic industrial entities in manual and low-standardized productive processes. The adopted algorithms adopts both supervised and unsupervised learning processes to achieve a performing data analytics. Third, an industrial dashboard is developed to analyze through strategic KPIs the efficiency and social sustainability of human-centric manufacturing systems on three different levels of detail, namely job-shop, operators and resources. Finally, the List of Symbols section sums up the indices and parameters to ease the reading process of this quantitative section.

### 2.1.1 IoT acquisition layer

The developed IoT layer is an UWB-based RTLS that acquires the dynamic indoor spatio-temporal positions of tagged entities with a given average sampling frequency. The IoT system is based on Decawave commercial modules and is composed of two main systems [101, 102]. First, a set of ANs define the reference region

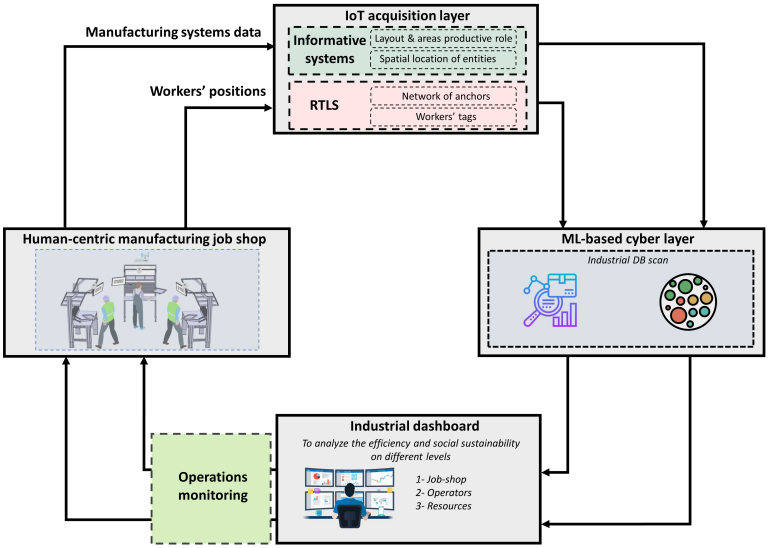


FIGURE 2.1: Developed cyber-physical system to monitor human-centric manufacturing job shops operations

in which are monitored the dynamic positions assumed by wearable and anonymous tags over working shifts. In detail, the UWB-based network of ANs estimates the dynamic positions assumed by tagged human operators over the shift through the TDoA ranging technique. This geometric method calculates the indoor spatio-temporal position of tags by the intersection of two hyperbolas from at least three active ANs [103]. Any AN is based on Raspberry PI 3 connected to a DWM1001 UWB-based radio module. These reference points have to be displaced on the ceiling of the manufacturing environment to be monitored with a distance between each other at greatest equal to 20 meters (Fig. 2.2). This network is connected and hence synchronized through a common Wi-Fi access point. The compact wearable tags are based on Decawave DWM1001 System on Module (SoM) which is configured to use UWB Channel 5 with bandwidth and frequency of 499.2 MHz and 6489.6 MHz, respectively. In addition, the DWM1001 SoM integrates, among the others, a low-power Nordic Semiconductors nRF52 microcontroller. Data sharing and acquisition are achieved by exploiting the Message Queuing Telemetry Transport (MQTT) protocol to enable data transfer to the remote server.

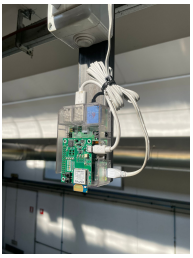

(A) Anchor mounted on the ceiling of an industrial building

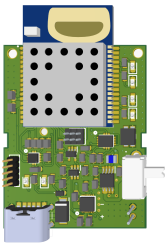

(B) Board of the tag worn by workers

FIGURE 2.2: Adopted UWB-based RTLS

### 2.1.2 Machine learning-based cyber layer

Based on the features of the adopted UWB-based RTLS network, this section extensively describes the steps to leverage the acquired spatio-temporal positioning data in manual and low-standardized manufacturing systems distinguished by value-added areas in which workers perform manual operations and SKUs storage areas (Fig. 2.3). The goal of such analysis is to detect through the original Industrial DB scan manufacturing HPIs with industrial entities such as machines and SKUs to gain unprecedented visibility of manufacturing job shops. For instance, evaluating the utilization ratio of industrial entities and the distances traveled by workers during material replenishment. To ease the reading process, five subsubsection outlines the key steps to be performed in order to meet such ambitious aims.

#### Four step positioning estimation

Before starting the detection of HPIs, a pre-processing step has to be implemented to mitigate the intrinsic interference of manufacturing settings in the anonymous positioning data (Fig. 2.3). First, acquired data are processed by the Savitzky-Golay filter. This data smoothing method fits a discrete set of points into a polynomial curve of a chosen degree using an odd time window [104]. Second, the Cheng Filter [105] detects and thus eliminates outliers whether the following condition is met (Eq. (2.1)).

$$|v_f^w - MAD^w| \geq v^{max} \tag{2.1}$$

Where $v_f^w$ represents the velocity of the $w$-th worker over the $f$-th timeframe and $MAD^w$ is the median absolute deviation with respect to velocities of the $w$-th worker.

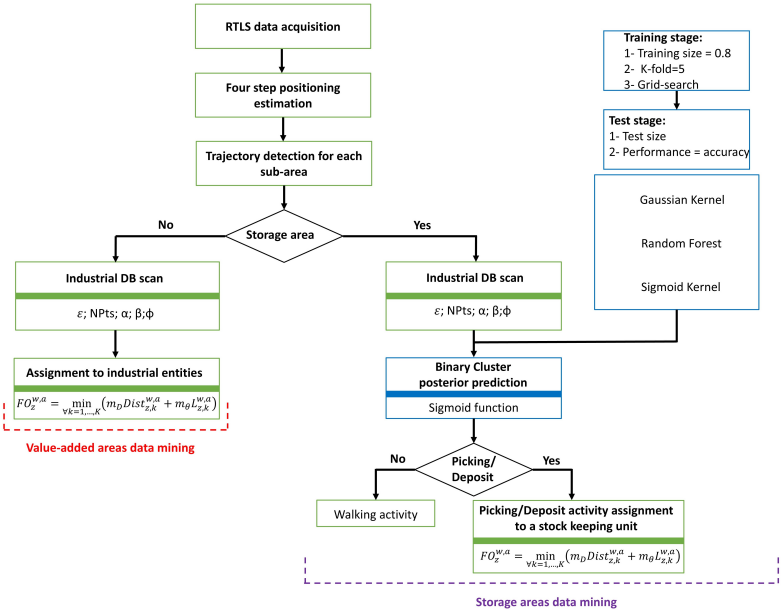


FIGURE 2.3: Heuristic flow diagram of the developed ML-based cyber-layer

Of course, $v^{max}$ is a constant and has to be set appropriately based on the motion patterns of the monitored case study. This data removal is particularly relevant since the following unicycle Extended Kalman Filter is insensitive to outliers in human trajectories [106]. In particular, the forward prediction of the state during the $f$-th timeframe given the previous one is computed as it follows (Eq. (2.2)).

$$x_{f|f-1}^{w} = \begin{bmatrix} px_{f-1}^{w} + \delta t v_{f-1}^{w} \cos\left(\theta_{f-1}^{w}\right) \\ py_{f-1}^{w} + \delta t v_{f-1}^{w} \sin\left(\theta_{f-1}^{w}\right) \\ \theta_{f}^{w} \\ v_{f}^{w} \end{bmatrix} + \begin{bmatrix} 0 & 0 \\ 0 & 0 \\ \delta t & 0 \\ 0 & \delta t \end{bmatrix} \begin{bmatrix} \eta\theta_{f-1}^{w} \\ \eta v_{f-1}^{w} \end{bmatrix} \tag{2.2}$$

Where $\theta_{f-1}^{w}$ and $v_{f-1}^{w}$ represent the worker's trajectory angle and velocity during the time frame $f-1$. In addition, $\eta$ represents the Gaussian distributed noise and $\delta t$ describes the delta time between consecutive indoor positions. The last method of the pre-processing step is to perform a backward estimation of the state at the $f$-1 given the $f$-th time frame through the Rauch-Tung-Striebel smoother [107].

### Trajectory detection for each sub-area

After having performed the noise mitigation, the proposed cyber layer performs a trajectory detection for each operator and sub-area as depicted in Fig. 2.3. Over a defined monitoring period, the set $T = \{T^w, T^{w+1}, ..., T^W\}$ groups sets of trajectories made by the $W$ active workers. Considering whichever industrial job shop, its monitored area can be conceptually divided into $A$ sub-areas based on their functional role in the manufacturing cycle. Where $A$ represents the possible number of sub-areas that should be decided in agreement with industrial plant supervisors. Therefore, $T^w = \{t_i^{w,a}, t_{i+1}^{w,a'}, ..., t_I^{w,a}\}$, where $t_i^{w,a}$ represents the $i$-th sub-trajectory of the $w$-th worker occurred in the $a$-th area of the job shop. Based on this, $t_1^{w,a}$ and $t_2^{w,a'}$ are two consecutive sub-trajectories occurred in different sub-areas (e.g. $a \neq a'$). In addition, any $t_i^{w,a} = \{p_{i,f'}^{w,a}, p_{i,f'+1}^{w,a}, ..., p_{i,f^*}^{w,a}\}$ is a structure where $p_{i,f}^{w,a} = (px_{i,f}^{w,a}, py_{i,f}^{w,a}, ts_{i,f}^{w,a})$ is a spatio-temporal point. In detail, any $f$-th point belonging to a given $t_i^{w,a}$ must meet the following condition(Eq. (2.3)).

$$\forall\, 0 \leq f < f' \leq F \Rightarrow ts_{i,f'}^{w,a} > ts_{i,f}^{w,a} \tag{2.3}$$

Based on the computed $t_i^{w,a}$, the algorithm checks whether sub-trajectories belong to any storage area of the considered manual job shop. As outlined in Fig. 2.3, whenever this check is false, the cyber layer automatically recognizes that the considered trajectory occurs in value-added areas and triggers two data mining steps, Industrial DB scan based, to detect HPIs with strategic industrial entities such as machinery and workbench (subsubsection 2.1.2). Contrarily, supposing the sub-trajectory check is met, specific data mining steps are performed to detect HPIs in storage areas, namely picking/deposit (P/D) activities in SKUs (subsubsection 2.1.2).

### Value-added areas' data mining

Whenever human workers interact with the surrounding manufacturing resources, they perform strategic activities in front of it. Therefore, any HPI has the following characteristics: (1) its consecutive points have a high-spatial density and (2) the related duration is strictly greater than zero seconds. Based on these considerations, the following paragraph quantitatively describes the original Industrial DB scan formulation.
Let consider an arbitrary $t_i^{w,a}$ composed by a variable number of $p_{i,f}^{w,a}$. The $\epsilon$ temporal sequence of a given $p_{i,f}^{w,a}$ is the maximum number of points in $t_i^{w,a}$ that meet the following condition (Eq. (2.4)).

$$p_{i,f}^{w,a} \in \epsilon(p_{i,f}^{w,a}, d^*) \Leftrightarrow EuclideanDistance(p_{i,f}^{w,a}, p_{i,f'}^{w,a}) \leq d^*, \forall p_{i,f}^{w,a} \in t_i^{w,a} \tag{2.4}$$

where $d^*$ describes the maximum radius to be considered. Supposing that in the $i$-th sub-trajectory the former condition is verified for a variable number of points, let define the $q$-th $\epsilon$ temporal sequence as $S_{i,q}^{w,a} = \{p_{i,f'_q}^{w,a}, p_{i,f'+1,q}^{w,a'}, ..., p_{i,f^*,q}^{w,a}\}$. However, the $\epsilon$ temporal sequence has to be consistent with the temporal dimension. The following Eq. (2.5) avoids considering two separate HPIs that occurred in the same region as one.

$$p_{i,f'_q}^{w,a} - p_{i,f'+1,q}^{w,a} = \delta t, \forall\ p_{i,f',q}^{w,a}\ ,\ p_{i,f'+1,q}^{w,a} \in S_{i,q}^{w,a} \tag{2.5}$$

where $\delta t$ represents the sampling time of the adopted IoT acquisition layer. Finally, $S_{i,q}^{w,a}$ is a relevant HPI whether groups at least a total number of points equal to or greater than NPts, a threshold of positioning points. This latter parameter is set based on human motion and may vary from sub-area to sub-area to increase the performance of the developed algorithm. However, the processed $p_{i,j,q}^{w,a}$ may be affected by the intrinsic uncertainty of human motion and other types of noise not properly mitigated during the pre-processing stage. Based on this, let consider two consecutive HPIs $C_{z,i}^{w,a}$ and $C_{z+1,i}^{w,a}$ for the first operator in the $a$-th sub-area during the $i$-th sub-trajectory. In detail, any $C_{z,i}^{w,a} = \{p_{i,f',z}^{w,a}, p_{i,f'+1,z}^{w,a}, ..., p_{i,f^*,z}^{w,a}\}$. In addition, HPIs are also distinguished by a geometric center $O_{z,i}^{w,a} = \{Ox_{z,i}^{w,a}, Oy_{z,i}^{w,a}\}$ that can be calculated as the weighted average between the current acquired position $(px_{i,f',z}^{w,a})$ and the delta time between consecutive timestamps $(ts_{i,f'+1,z}^{w,a}$ and $ts_{i,f',z}^{w,a})$ (Eq. (2.6)).

$$Ox_{z,i}^{w,a} = \frac{\sum_{f=f'}^{f^*-1} px_{i,f',z}^{w,a} \left(ts_{i,f'+1,z}^{w,a} - ts_{i,f',z}^{w,a}\right)}{\sum_{f=f'}^{f^*-1} \left(ts_{i,f'+1,z}^{w,a} - ts_{i,f',z}^{w,a}\right)} \tag{2.6}$$

The same approach is adopted to calculate the $y$ dimension of the center. In addition, from a temporal viewpoint $C_{z,i}^{w,a}$ and $C_{z+1,i}^{w,a}$ are spaced by a fixed duration in the preferred time unit. Therefore, two consecutive HPIs can be merged into a single one whether the Eq. (2.7) is met and at least one between Eq. (2.8) and (2.9) is true [96].

$$ts_{i,f^*,z}^{w,a} - ts_{i,f',z+1}^{w,a} \leq \alpha \tag{2.7}$$

$$EuclideanDistance(p_{i,f^*,z}^{w,a}, O_{z+1,i}^{w,a}) \leq \beta \tag{2.8}$$

$$EuclideanDistance(p_{i,f^*,z}^{w,a}, p_{i,f',z+1}^{w,a}) \leq \phi \tag{2.9}$$

where $\alpha$ depends on the average time spent to travel from a process interaction to the following one and $\beta$ and $\phi$ on the expected distance from consecutive process interactions. However, the detected HPIs provide no information on the manufacturing system because they are not related to any industrial entity and thus fail to develop industrial KPIs. In manufacturing environments, human operators perform certain activities of productive processes in known regions of job shops. These areas may be within the boundaries of machines, workbenches, etc. To this extent, let index as $k$ these relevant industrial entities. Indeed, as depicted in Fig. 2.3, any detected $C_{z,i}^{w,a}$ can be assigned to one of them. To do so, a geometric entity representing any $k$-th industrial resource and an objective function to be minimized have to be properly defined. Starting with the first, given the specific geometrical shape of the $k$-th industrial entity, $B_k$ represents its centroid. Then, the formulation of the objective function to assign any $C_{z,i}^{w,a}$ to a unique $k$ follows. This assignment is based on distances and orientations. On one hand, the distance of the $z$-th HPI from an arbitrary $k$-th industrial resource is outlined in the Eq. (2.10).

$$Dist_{z,k}^{w,a} = \frac{\sum_{j=j''}^{j^*-1} dist(p_{i,f',z}^{w,a}, B_k) \left( ts_{i,f'+1,z}^{w,a} - ts_{i,f',z}^{w,a} \right)}{\sum_{j=j'}^{j^*-1} \left( ts_{i,f'+1,z}^{w,a} - ts_{i,f',z}^{w,a} \right)} \tag{2.10}$$

where $dist(p_{i,j'',z}^{w,a}, B_k)$ represents the Euclidean distance between the spatio-temporal point $f'$ of the $i$-th sub-trajectory of the $z$-th HPI for the $w$-th operator in the $a$-th sub-area, and the centroid of the $k$-th industrial resource. On the other hand, the orientation of each process interaction with respect to the $k$-th industrial resource requires more computational steps. First, it is calculated $\theta_{i,f',f'+1,z}^{w,a}$ the angle assumed by the $w$-th worker from the spatio-temporal point $f'$ and $f'+1$. Second, $\theta_{i,f',k,z}^{w,a}$ represents the angle assumed by the same worker and the centroid of the $k$-th industrial entity. Therefore, Eq. (2.11) calculates the resulting orientation from the spatio-temporal point $f'$ to the $k$-th industrial entity.

$$L_{f',k}^{w,a} = |\theta_{i,f',k,z}^{w,a} - \theta_{i,f',f'+1,z}^{w,a}| \tag{2.11}$$

Finally, since HPIs group a variable number of spatio-temporal points, Eq. (2.12) evaluates the orientation of process interactions with respect to the $k$-th industrial entity.

$$L_{z,k}^{w,a} = \frac{\sum_{j=f'}^{j^*-1} L_{i,f'}^{w,a} \left( ts_{i,f'+1,z}^{w,a} - ts_{i,f',z}^{w,a} \right)}{\sum_{j=f'}^{j^*-1} \left( ts_{i,f'+1,z}^{w,a} - ts_{i,f',z}^{w,a} \right)} \tag{2.12}$$

After having presented all the relevant parameters to perform the assignment of HPIs, the objective function to be minimized is outlined below (Eq.(2.13)).

$$FO_z^{w,a} = \min_{\forall k=1,\dots,K} \left( m_D Dist_{z,k}^{w,a} + m_\theta L_{z,k}^{w,a} \right) \tag{2.13}$$

where $m_D$ and $m_\theta$ represent the weights connected to the distances and the orientations, respectively. Consequently, the remaining spatio-temporal points of a given sub-trajectory in value-added areas represent a walking activity for the considered human worker.

### Storage areas' data mining

Whether the detected sub-trajectory (see subsubsection 2.1.2) occurs in storage areas, the original ML-based cyber layer aims at detecting P/D activities with SKUs (Fig. 2.3). Therefore, industrial plant supervisors can analyze in which SKUs anonymously tagged workers perform P/D activities and thus evaluate the material allocation efficiency. To achieve this purpose, the first step to be performed is the Industrial DB scan. Despite the algorithm operatively works as outlined before, the hyper-parameters (e.g., $\epsilon$ NPts, $\alpha$,$\beta$ and $\phi$) due to potentially different motion patterns may be indexed to $a$. Contrary to value-added areas, storage areas are generally wider in terms of square meters. Indeed, some HPIs detected by the developed Industrial DB scan may be FP due to, among the others, the intrinsic uncertainty of human motion and noise of the signal acquired by the locating technology. For instance, the Industrial DB scan may label as process interactions trajectories instances in which the speed of worker motion decreased to overcome unexpected obstacles or aisles congestion. Based on this, a further processing step, supervised learning-based, is leveraged to avoid overestimations of HPIs leading to unrepresentative KPIs (Fig. 2.3). In detail, any $C_{z,i}^{w,a}$ is also distinguished by a mean velocity, acceleration, and duration (e.g., $\overline{v}_{z,i}^{w,a}$, $\overline{a}_{z,i}^{w,a}$ and $dur_{z,i}^{w,a}$). In addition, HPIs are manually assigned to class 1 whether, according to the collected ground truth, they cluster P/D activities, 0 otherwise. Considering real manufacturing environments, collecting large video-based ground truth datasets may raise privacy and industrial secrets concerns of operators and companies, respectively. Another potential limitation is represented by the installation of cameras that may obstacle manual production routines. Therefore, a potential issue is represented by the limited dimension of ground truth datasets upon which training supervised ML models. In such a scenario, to maximize KPIs accuracies while limiting the intrusiveness of ground truth's video acquisitions, supervised-based ML algorithms can be easily trained with limited datasets compared to artificial neural networks [108]. Based on this, as depicted in Fig. 2.3, a Gaussian and Sigmoid Kernel, and a Random Forest are adequately trained using a shared approach. The 80% of the dataset represents the

TABLE 2.1: Example of time-dependent working operation of a UWB tagged worker

| Start | End | Duration [sec] | Operation | SKU | Distance [m] |
|---|---|---|---|---|---|
| 10:06:26.47 | 10:06:46.09 | 19.62 | Workbench 1 | 0 | 0 |
| 10:06:46.76 | 10:06:51.36 | 4.60 | Walking | 0 | 3.4 |
| 10:06:51.59 | 10:06:53.83 | 2.15 | Picking/Deposit | 2 | 0 |
| ... | ... | ... | ... | .. | ... |
| 11:31:03.58 | 11:31:11.41 | 47.83 | Machine 1 | 0 | 0 |

training set. In this heterogeneous set, a K-fold cross-validation and a grid-search approach are implemented. As a result, the proposed models are less biased and the hyperparameters optimized. While for the two kernels the hyperparameters to be optimized are $\gamma$ and $C$, the Random Forest classifier has to optimize the number of estimators, the minimum sample splits and the number of features allowed. Then, the accuracies of the hyperparameters optimized classifiers are validated in the test set. After having learned the features connected to classes, the prediction stage can be triggered for whichever HPI returned by the Industrial DB scan in sub-trajectories of storage areas over working shifts. In detail, a Sigmoid function computes the posterior class probability for each classifier [109]. Subsequently, these predictions are ensembled through a weighted average using classifiers accuracies as weights. Finally, the returned HPI is assigned to the class that has the highest probability. Whether the class is equal to 1, this picking or deposit activity has to be assigned to one of the SKUs belonging to the involved storage areas. According to Fig. 2.3, the assignment function follows the same approach outlined in Eq. 2.13. Otherwise, the HPI is considered a walking activity as the other instances of the sub-trajectories not previously labeled as HPIs by the Industrial DB scan.

### 2.1.3 Industrial dashboard

Benefitting from the presented cyber layer computations to mine value within UWB-based spatio-temporal trajectories, Table 2.1 summarizes how the time-dependent operations of monitored workers are classified during a standard working time window. In detail, the SKU column has values greater than zero only if the related operation is a P/D activity. Similarly, solely walking activities have distances travelled greater than zero meters. It is worth noting that this IoT-based data may enrich the visibility of any manual and low-standardized job shop. Indeed, it is extremely useful to develop industrial KPIs upon with monitor the interdependencies, efficiency, and social sustainability of manufacturing job shops. The following bullet point lists the strategic industrial metrics on three different levels of detail:

- **Job shop:** Operator activities timeline and segmentation; duration and number of P/D activities in storage areas

- **Operators:** Distances travelled in P/D activities; number of interaction with SKUs; from-to charts of travelling activities
- **Resources:** utilization ratio; usages overlapping

Based on the definition of these KPIs and levels of analysis, Fig. 2.4 outlines the developed industrial dashboard to achieve a user-friendly decision-making process. Plant supervisors have a unique opportunity to analyze processes' underperformance under different levels of detail. For instance, the job shop level of analysis may suggest that P/D activities are not optimized due to poor material allocation. Despite this information being strategic to trigger a re-layout process, it fails to analyze an important negative externality. In this regard, the operators' level of detail evaluates the distances travelled by workers during P/D activities to provide mainly two insights. First, a set of workers may be socially disadvantaged due to longer distances covered within the same shift. Second, these inconsistencies may be detected also comparing historical data of several different shifts. To conclude this high-detailed and quantitative section, the following lines combined with the List of Symbols highlight the key steps of the ML-based cyber layer (subsection 2.1.2). After the data acquisition of RTLS-based historical data for a given working shift, the consistency of positioning data is improved with a four-step positioning estimation approach (sub subsection 2.1.2). In this regard, the Savitzky-Golay and Cheng filters (Eq.(2.1)) perform data smoothing and outliers removal in operators' trajectories respectively. Then, the unicycle Extended Kalman filter (Eq.(2.2)) and Rauch-Tung-Striebel smoother further improve the acquired motion patterns. The resulting operators' trajectories are time-dependently indexed to $a$, the respective sub-areas of occurrence (sub subsection 2.1.2 ). Based on $a$, each trajectory follows specific data mining steps as depicted in Fig.2.3. On the one hand, whether the check on storage areas is not verified, two data mining steps are triggered to automatically detect HPIs with industrial resources (sub subsection 2.1.2):

- **Industrial DB scan**: based on the detailed formulation from Eq. 2.4 to Eq. 2.9, it triggers the detection of HPIs. However, such clustered positions provide little information on the system functioning since are not related to any industrial entity.
- **Assignment to industrial entities**: it defines an objective function to be minimized in order to assign HPIs to industrial entities based on distances and angles. From a geometric viewpoint, industrial entities are represented by a centroid.(e.g., from Eq. (2.10) to Eq. (2.13))

On the other hand, three data mining steps detect HPIs with storage areas' SKUs (sub subsection 2.1.2):

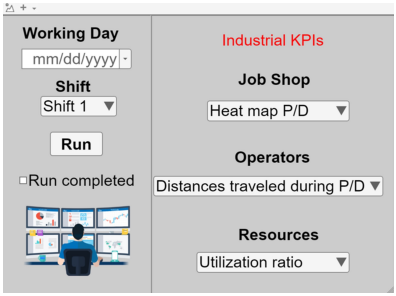


FIGURE 2.4: Industrial dashboard

- **Industrial DB scan**: this step follows the same mathematical formulation, exploiting identical input data. However, hyperparameters (e.g., $\epsilon$ NPts, $\alpha$,$\beta$ and $\phi$) may be different due to potentially different operators' motion patterns in storage areas.
- **Binary Cluster posterior prediction**: benefitting from 3 trained ML-based classifiers (e.g., random forest, gaussian and sigmoid kernel), the detected HPIs are distinguished into walking or P/D activities. To do so, the classifiers perform the posterior binary prediction through Sigmoid functions and ensembled using the weighted average (e.g., weights are the training accuracies). Finally, the HPIs are assigned to the activity that has the highest probability.
- **Picking/Deposit assignment to a stock keeping unit**: during this last step the P/D operations are assigned to SKUs following the same reasoning of before with industrial entities.

## 2.2 Cyber-physical system validation

The previously described digital system is tested and validated in a south-European manufacturing company that performs precision machining operations of components for the automotive industry. Fig. 2.5 depicts the layout of the monitored job shop in which two workers perform the manufacturing process. In such an environment, an agreement with industrial supervisors, the dedicated workforce, and the labor union is reached to develop in Operator 5.0 inspired solution [3]. Indeed, workers wear on the preferred upper arm an anonymous UWB-based tag. Leveraging the developed CPS, plant supervisors require to evaluate the material allocation in storage areas at the detail level of each SKU and monitor the utilization ratio of industrial entities (e.g., workbenches and machines). This double level of analysis focuses on plant efficiencies and social sustainability of the workforce.

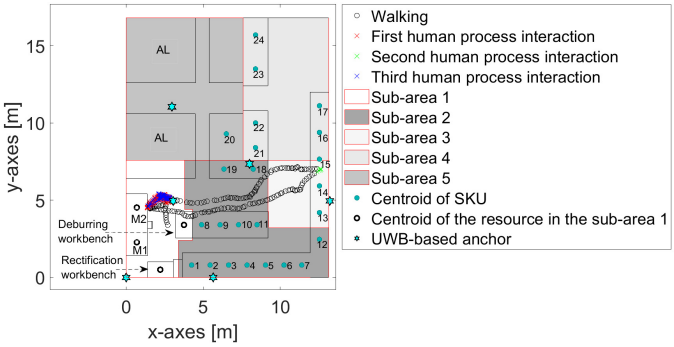


FIGURE 2.5: Reference manual job shop of the manufacturing case study

### 2.2.1 Case Study

Before starting the experimental campaign, an extensive demonstratory period is focused on establishing trust among all shareholders. Based on this, laboratory tests are shown to workers to quantitatively back up the clear purpose of the analysis. Moreover, workers are fully compliant to sign the GDPR. In this non-binding agreement, they can revoke their consensus. Particular attention is focused on data storing and adequately blurring video-based ground truth. Finally, during the latest meetings, it is decided to leave six anonymous tags in the company's locker room to be autonomously equipped on the operators' preferred upper arm. Benefitting from this transparent process, all workers are fully compliant to be involved in the analysis. In addition, Fig. 2.5 shows the 2D geometrical positions of six ANs of the developed IoT acquisition layer having $z$-axis equal to 7.00 m. However, indoor positioning raw data with an average sampling rate equal to 20 Hz are highly affected by noise. In detail, the mean speed profile of workers is equal to 9.6 m/s. To increase the consistency of human motion patterns, the previously described four step positioning estimation methods (subsubsection 2.1.2) are adopted resulting in a sampling rate and mean speed profile equal to 6.6 Hz and 1.3 m/s. Subsequently, based on the algorithm requirements, industrial supervisors decide to divide the monitored job shop into five sub-areas depending on their functional role in the manufacturing process (e.g., A=5). The value-added area, namely the sub-area 1, hosts four different industrial entities and represents the most visited one by workers. In detail, workers load and unload into dedicated stand-alone machines (e.g., M1 and M2) different batches of materials and then perform manual manufacturing operations in the deburring and rectification workbenches (Fig. 2.6 (b)). As depicted by Fig. 2.6 (b), it is worth noting that the distances between the industrial entities

combined with the high degree of freedom of human movements may considerably challenge the accuracy and reliability of the Industrial DB scan and the assignment of HPIs. In this area, industrial plant supervisors require to calculate the utilization ratio per worker of such entities and detect potential simultaneous usages of workbenches. Apart from the sub-area 5 which hosts two automatic lathes and the SKU ID 20 for scraps, the other three sub-areas stock different batches of materials. In particular, the fourth one groups SKUs of finished materials to be moved into other in-plant job shops by manual forklifts. The sub-area 2, partially depicted in Fig. 2.6 (a) from a static viewpoint, stocks both finished and raw materials while the third one raw materials. Centroids of the SKUs are depicted through green dots in Fig. 2.5. Based on the production schedule at the beginning of each working shift, workers are required to move as close as possible to sub-area 2 all SKUs containing the batch to be manufactured and empty SKUs in which store processed materials. Therefore, based on the outlined cyber layer capabilities, plant supervisors can digitally analyze the efficiency of such material allocation by monitoring P/D activities in SKUs along with distances traveled in such routes. However, before starting to discuss the industrial KPIs in section 2.3, two intermediate considerations are addressed. First, for the sake of clarity, subsection 2.2.2 describes the ML-based cyber layer computations on sub-trajectories. Second, subsection 2.2.3 validates the performances of the ML-based algorithms based on the collected ground truth. This investigation plays a pivotal role in order to avoid unrepresentative and misleading industrial KPIs.

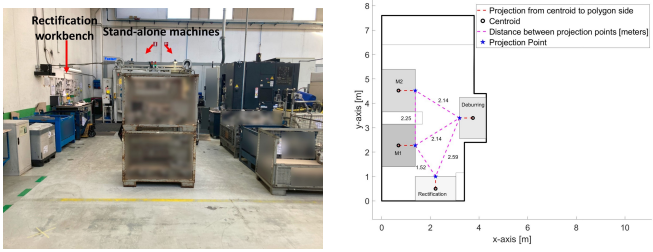


(A) Layout of the monitored manufacturing job-shop from a static point of view

(B) Geometry of the sub-area 1

FIGURE 2.6: Human-centric industrial job shop

### 2.2.2 Evaluation on sub-trajectories of ML-based cyber layer

Benefitting from the algorithm functioning, Fig.2.5 represents an example of HPIs detection in the manual and low-standardized job shop. The considered human

movement occurred from 11:45:47 to 11:47:00 on the $15^{th}$ of February 2021. According to the collected video-based ground truth, the operator 1 works in M2 for 38.71 seconds and then transiting through the sub-area 2 picks two raw materials from the SKU ID 15 and then goes back to M2 to load them in 15.74 seconds. As depicted in Fig.2.5, the developed CPS detects three different process interactions. In the proposed example of five trajectories, the TP and TN are equal to 3 and 4, respectively. These instances represent a match between the actual scenario and the one determined by the developed algorithm. In this case of perfect detection, bot FP and FN are equal to zero. For the sake of completeness, a FP takes place whenever the Industrial DB scan clusters noise points into a not expected HPI. The FN represent the opposite condition. For simplicity, it is assumed that the three returned HPIs are the first three detected in the monitoring period. Indeed, $C_{1,1}^{1,1}$ and $C_{3,5}^{1,1}$ last 36.95 and 14.59 seconds, respectively. Therefore, the relative deviations of process interactions' duration are below 10%. In sub-area 3, a process interaction is detected, namely $C_{2,3}^{1,3}$. In particular, its input features (e.g., $\overline{v}_{2,3}^{1,3}$ and $\overline{a}_{2,3}^{1,3}$ and $dur_{2,3}^{1,3}$ ) are fed into the ensembled supervised learning classifiers to compute the posterior class probability. Since the resulting probability of class 1 is equal to the 80%, $C_{2,3}^{1,3}$ is classified as a P/D activity. Despite no basis to better identify these two activities due to the intrinsic RTLS characteristics, the proposed digital system is much more practical and way less costly than tagging, using the RFID technology, products or industrial entities in modern manufacturing job shops. Finally, this process-driven activity is correctly assigned to the SKU ID 15. Despite the promising accuracies obtained by the ML-based methods in this set of spatio-temporal trajectories, the following subsection validates its performances with larger and representative ground truth datasets.

### 2.2.3 Performances of the machine learning based cyber layer

To adequately validate the performances of the ML-based algoritms, video-based ground truth is collected in 4 working shifts involving different workers. Considering the value-added area (e.g.,sub-area 1), 68 relevant process interactions occur with an aggregate length equal to 48.11 minutes. In addition, the data set is fairly balanced. While the percentages of HPIs that occurred in M1, M2, and deburring range from 25% to 30%, the rectification workbench hosts 20% of them. Based on the left part of Fig. 2.3, after the detection of $T^w$ and the related sub-trajectories in sub-areas, the developed Industrial DB scan is adopted to detect relevant HPIs using NPts and $\epsilon$ equal to 15 and 0.17 meters, respectively. In addition, $\alpha$ is equal to 1 second and $\beta$ and $\phi$ to 0.5 meters. These latter parameters are responsible for merging consecutive process interactions. The Industrial DB scan accuracies are evaluated through two metrics. First, a confusion matrix is developed to evaluate detection performances. The resulting accuracy over the 68 HPIs is equal to 82%.

Second, the comparison between expected and returned process interactions' duration is evaluated. Fig. 2.7 depicts this temporal analysis through the absolute and relative deviation of process interactions' duration. The data set considers solely the TP that are equal to 51 relevant process interactions. In detail, the mean absolute and relative deviations are equal to 2.69 seconds and 14.14 %, respectively. After having assessed the promising accuracies of the proposed Industrial DB scan

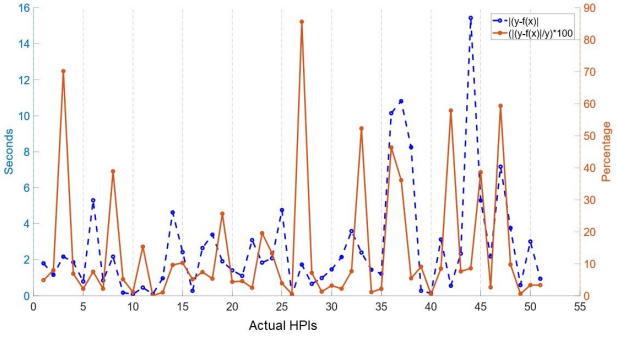


FIGURE 2.7: Temporal performances of HPIs' detection of the developed cyber-physical system

in such a small area, HPIs have to be assigned to one of the four industrial entities shown in Figure 2.6. Weights of the objective function in Eq. (2.13) are arrays of 11 rows with element values that range from 0 to 100. Of course, the element-wise summation has to be equal to 100. Fig. 2.8 shows the accuracies of the 11 objective functions to assign HPIs to industrial entities. In detail, the first and last objective functions give no relevance to the angle and distance, respectively. The highest accuracy equal to 88.1% is achieved by the second one with $m_D$ and $m_\theta$ equal to 90 and 10, respectively. The same approach is adopted for the four storage areas to test and validated the right part of the cyber layer in Fig. 2.3 aimed at detecting P/D. In contrast to sub-area 1, it is reasonable to expect much shorter HPIs in stocking areas. Indeed, the Industrial DB scan is adopted using the same hyper-parameters apart from NPts which is equal to 5. Based on the collected video-based ground truth in the same 4 working shifts as before, 44 different trajectories of P/D activities for a total duration of 8.35 minutes are analyzed to validate the algorithm under different human motion patterns. The proposed Industrial DB scan returned 100 different HPIs in which all the expected relevant activities were detected. However, a problem of over-estimation occurs. In detail, 35% of returned interactions are not related to the monitored manufacturing cycle. Among them, there are unexpected process interactions of human operators driven by different causes (e.g., unexpected obstacles). For this purpose, supervised-learning techniques are leveraged to learn the

movement patterns of this scenario using as input features $\overline{v}_{z,i}^{w,a}$ and $\overline{a}_{z,i}^{w,a}$ and $dur_{z,i}^{w,a}$. During the training stage, the most performing hyper-parameters combinations are evaluated for all classifiers. In detail, the two kernels share the same optimal $\gamma$ value equal to 0.01 but they have different C values. The Gaussian and Sigmoid values of C are equal to 10 and 1, respectively. On the other hand, the Random Forest is optimized under other sets of hyperparameters. The best configuration has 50 estimators, a minimum sample split of 0.6 and the features allowed are equal to the square root of the total number of features in the training data set. Then, the performances of the hyperparameters optimized classifiers are validated in the test set. While the Random forest has an accuracy of 71.4%, the accuracies of the Gaussian and Sigmoid Kernel are equal to 61.9% and 42.9%, respectively. The resulting accuracy of the weighted and Sigmoid-based ensembled classifier is equal to 76.4%. Finally, the objective function to be minimized performs the assignment of the detected HPIs to to one of the SKU plotted in Fig. 2.6. Based on the available ground truth, this assignment solely depends on the distances with an accuracy of 100%.

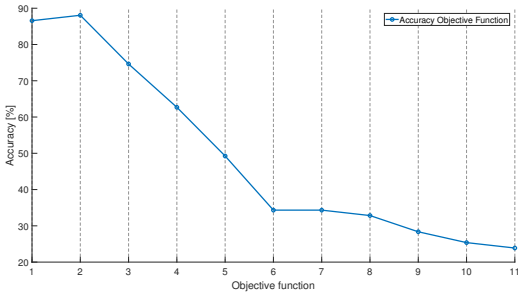


FIGURE 2.8: Objective functions accuracies in HPIs' assignment

## 2.3 Results & managerial insights

Based on the successful validation of the digital CPS (subsection 2.2.3) in the mentioned manual and labor-intensive manufacturing job shop, this section presents the industrial KPIs to monitor the efficiency and the social sustainability according to the Industry 5.0 principles. The remaining discussion is divided into three levels of detail, following the industrial dashboard structure in Fig. 2.4.

### 2.3.1 Job shop level

The job shop dimension monitors from an aggregate viewpoint the functioning of the manual and UWB-referenced job shop. In particular, Fig. 2.9 (a), depicts the

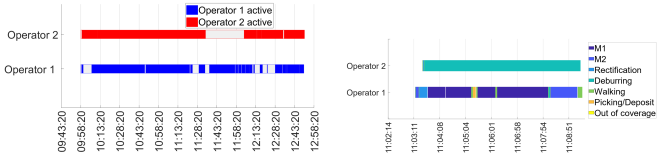


(A) Monitored time window of anonymous operators

(B) Time-dependent activities

FIGURE 2.9: Temporal analysis of anonymous workers on the $3^{rd}$ March 2022

monitored time window in which two anonymous operators equipped with their respective TagID are working within the coverage area defined by the displacement of ANs (Fig. 2.5), during the $3^{rd}$ of March 2022. In addition, Fig. 2.9 (b) shows the time-dependent activities performed by workers from 11:03:00 to 11:09:00 on the monitored shift. While operator 2 mostly performs value-added operations in the deburring workbench, the other colleague performs several process-driven tasks. In particular, one P/D activity and eight HPIs are automatically detected, where the vast majority of them occurs in M1. However, these first two KPIs fail to provide privileged insights for industrial supervisors' needs. Indeed, no evaluations regarding material allocations and resource utilization can be established. Starting with the first aim, Fig. 2.10 shows through a dedicated color bar from white to red the aggregated P/D interactions over the monitored time window in SKUs. Benefitting from this, industrial plant supervisors can analyze the efficiency of the manufacturing systems during P/D traveling activities. Fig. 2.10 suggests that the monitored manufacturing system is not optimized. Based on this, it is useful to consider the SKUs in the sub-area 2. The nearest SKUs to sub-area 1 host the highest P/D activities. In detail, SKUs ID 1 and 3 have 56 and 15 visits over the monitored period, respectively. However, the farthest SKUs ID namely 5, 6, 7, 11, 12, and 18 register combined together 24 P/D activities. This accounts for 18.6% of the total P/D activities over the considered time period. Adopting the same approach with SKUs of other sub-areas, this metric increases to 26%. Therefore, almost a third of P/D activities are inefficient.

In addition to this, Fig. 2.11 completes the analysis depicting the duration of HPIs activities in storage areas for both workers. During the monitored time period, the two anonymous workers spend roughly 25 minutes performing P/D activities in storage areas. Based on the proposed heatmaps (Fig. 2.10 and 2.11), there is a clear direct correlation between the number of interactions with SKUs and the time spent performing P/D activities. Indeed, as expected, SKU ID 1 shows the highest duration, accounting for 633.69 seconds. However, the underperforming material allocation in storage areas' SKUs can be analyzed on the temporal dimension as

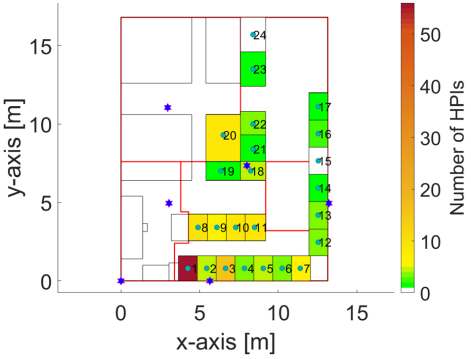


FIGURE 2.10: Number of HPIs in storage areas during the monitored time window of anonymous workers on the $3^{rd}$ March 2022

well. Considering the most inefficient SKUs of sub-area 2 (e.g, ID from 4 to 7, 11, 12 and 18), the total duration to perform/picking and deposit activities is equal to 250 seconds which accounts for the 16% of the total time to perform such process-driven activities. This statistic increases to the 30% by taking into account all SKUs belonging to other sub-areas. Also, such underperforming material allocation in storage areas triggers a consistent negative externality on meters travelled by workers. Therefore, the following subsection narrows the analysis to the Operators' level of detail to properly assess the impact of logistic activities on their manufacturing routines.

### 2.3.2 Operators level

The P/D activities of workers in defined SKUs show fairly similar percentages. While worker 1 visits 84 times the SKUs accounting for the 11% of his working routine, operator 2 performs 66 P/D activities during the 7% of the monitored period. For both workers, several P/D activities start and return in sub-area 1. Based on this, Fig. 2.12 outlines the meters traveled by workers to perform different activities in the manufacturing system (the acronyms A1 refer to the sub-area 1). While the total distances traveled over the monitored period by the two workers differ from 150 meters, the comparison of travelings involving P/D activities needs to be properly analyzed. Considering the traveling activities from sub-area 1 to a P/D activity, operator 1, and operator 2 walk 207.47 and 193.28 meters, respectively. Despite these metrics having similar values, the two workers perform highly different in-plant flows. Worker 1 and worker 2 travel from sub-area 1 to a given SKU 60 and 25 times, respectively. Indeed, worker 2 travels 2.24 times the meters of the other colleague, considering mean values.

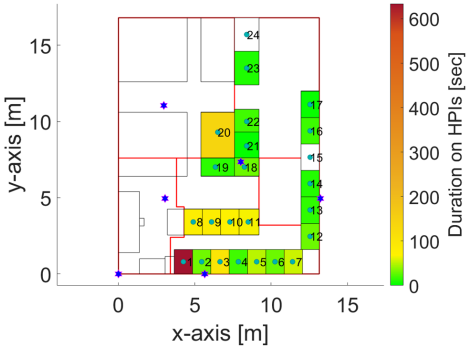


FIGURE 2.11: Duration of HPIs in storage areas during the monitored time window of anonymous workers on the $3^{rd}$ March 2022

Despite most of the time the two workers start the considered traveling route either from the rectification workbench or the deburring one, they show markedly different P/D activities within the defined SKUs. To properly analyze and discuss this scenario, the 24 SKUs are divided into five classes. The "prime" class includes the SKUs 1,2,8. While the SKUs ID 3,4,9,10, and 19 belong to the "sub-optimal" class, the remaining SKUs of the sub-area 2 are grouped into the "underperforming" one. Finally, all the other SKUs, apart from the 20 that belongs to the "scrap" class due to the intrinsic nature of material stored in it, are grouped in the class named "long". On one hand, worker 1 performs 43 P/D activities in the "prime" class accounting for 72% of HPI in storage areas. In addition, 18% of flows happen in the "sub-optimal" SKUs. Among the other flows from the sub-area 1, solely 6 P/D visits are towards the "long" class, accounting for 8% of the total activities in storage areas. The longest distance traveled is equal to 11.54 meters and involves a flow from the rectification workbench to the SKU ID 20, most likely to deposit a manufacturing scrap. No flows from the sub-area 1 go to the "long" class. On the other hand, the P/D activities of operator 2 from the sub-area 1 are completely different. Based on this, only 8% of flows are towards to SKU ID 1. In addition, while 14 flows go to the "sub-optimal" SKUs, 24% of total flows involve the "underperforming" class. The "long" class hosts 3 flows in the sub-area 5 to interact with the SKUs ID 22 and 23. According to these KPIs, worker 2 due to poor materials and thus SKUs allocation is socially disadvantaged. This scenario is completely similar when analyzing the number of flows with the distances traveled from P/D activities to sub-area 1 and among consecutive P/D activities. Regarding these latter flows, the evaluated KPIs suggest that operator 2 is also responsible for moving SKUs around the manufacturing job shop. While worker 1 performs the 80% of consecutive P/D activities either in the "prime" class or with the "sub-optimal" one (e.g, from SKU ID1 to SKU ID 8,

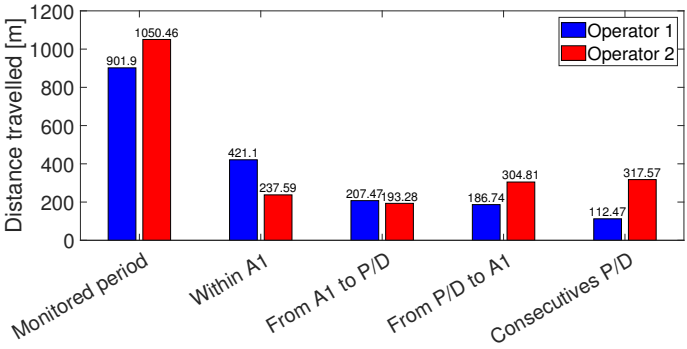


FIGURE 2.12: Distances traveled by operators during the monitored period

from SKU ID 1 to SKU ID 2, from SKU ID 3 to SKU ID 8, etc.), operator 2 travels between SKUs belonging to different sub-areas. Stark examples are represented by flows from SKU ID 7 to SKU ID 17 and to SKU ID 23. By comparing these sets of flows with the ones within the sub-area 1, it is clear how manual manufacturing systems rely on human commitment. Compared to SKUs that are dynamic entities, the four industrial entities have fixed locations defined by the aforementioned centroids ( Fig. 2.6). Indeed, at mean values, worker 1 and worker 2 travel within the sub-area 1 1.57 and 1.64 meters, respectively.

The acknowledgment of these inconsistencies in the monitored human-centric manufacturing system provides strategic insights to enhance the decision-making process. In particular, plant supervisors can re-balance the distances travelled by workers during P/D activities. To achieve this aim, internal meetings may be organized to raise awareness among the workforce of efficient material allocation in storage areas. Focusing on the positive externality in reducing distances traveled, industrial plant supervisors may define specific guidelines to properly move as nearest as possible to the sub-area 2 the material batches to be manufactured during the shifts. According to the Operator 5.0 concept, a further incentive to meet this target is to design gamification approaches [110]. For instance, workers that travel the shortest distances during P/D activities may be awarded on a monthly basis. Therefore, the social sustainability of the considered low-standardized job shop is constantly reinforced at desired values while spreading the best practices among operators. Finally, based on supervisors' requests, the following subsection analyzes the resources' level of detail to point out their utilization ratio during the monitored time window.

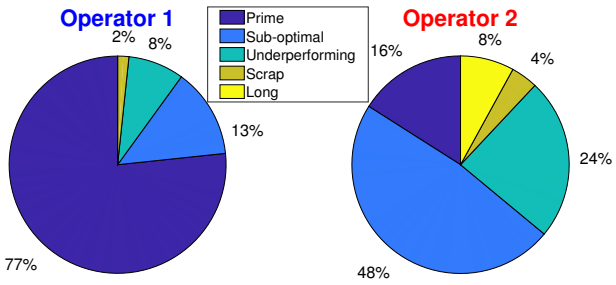


FIGURE 2.13: Percentages for operators of P/D activities from sub-area 1 divided by class of SKUs

### 2.3.3 Resources level

To properly assess the utilization ratio of resources, the focus is ensured on the workers' activities segmentation (Fig.2.14). As depicted by the pie charts, operators 1 and 2 perform value-added activities for 56% and 62% of the entire time window interacting with the four industrial entities (e.g., M1, M2, rectification, and deburring workbenches) in the sub-area 1, respectively. However, these two workers have different patterns of interaction with the entities. While the working percentages of worker 1 are fairly balanced among the four resources, the working times of operator 2 are distinguished by a markedly different pattern. Indeed, operator 2 for 74.8 minutes, that account for 44% of the entire working routine, performs materials deburring. These four resources are distinguished by a low utilization ratio.

The deburring workbench registers the highest ratio equal to 55.9%. In addition, the monitored operators correctly parallelize their working routine by avoiding to occupy simultaneously the same resource. In this regard, a more performing material allocation may bring a further positive externality, namely a likely increase in the share of these value-added operations in the considered manufacturing process. Simultaneously, plant supervisors can combine the utilization ratio of industrial entities with manufactured goods to evaluate and compare the working efficiency of multiple working shifts. For instance, a decrease in finished products can be analyzed through the different patterns of interactions with industrial entities. In such a scenario, it is reasonable to expect low utilization ratios of M1 and M2. At the same time, the deburring and the rectification workbenches may register high shares. Therefore, a likely root cause may be driven by poor automatic lathes' working quality potentially due to a worn tool.

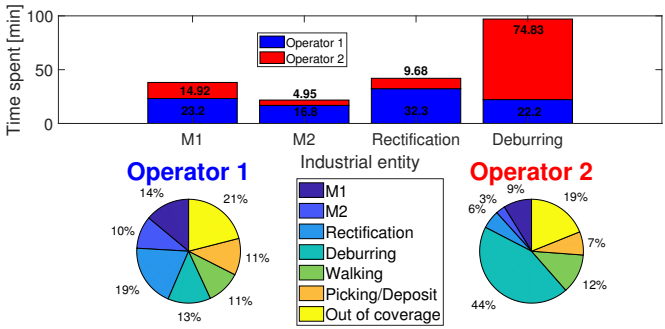


FIGURE 2.14: Activities segmentation of the anonymous operator over the monitored time window

To conclude, the proposed digital system can effectively support human-centric and low-standardized job shops by creating value for its operational business. In particular, the adopted IoT acquisition layer combined with the ML-based cyber layer enables a performing data analytics to enhance the visibility of the process functioning by minimizing installation costs compared to the RFID technology. Therefore, benefitting from the discussed multidimensional KPIs, industrial plant supervisors constantly analyze the in-plant operation and trigger target-oriented evaluations on processes' inefficiencies.

## Chapter 3

# Digital monitoring of Reconfigurable Manufacturing Systems

"Just wrap your legs 'round these velvet rims
And strap your hands cross my engines
Togheter we could break this trap"
*– Bruce Springsteen, Born to Run, 1975*

The previously tested and validated CPS highlights several benefits of monitoring the efficiency and social fairness of production environments. However, its definition, implementation, and deployment are strongly limited to human-centric job shops. Besides embracing the discussed digital transformation, manufacturing companies are experiencing and introducing novel production paradigms with different designs [111]. Among the others, short product life cycles and flexible batches are a key elements that powers this transition [112]. Traditional paradigms such as flexible manufacturing systems (FMS) and dedicated manufacturing systems (DMS) are distinguished by restricted capacity in reconfiguring themselves to meet a variable production with short life cycles [113]. These limitations are mainly driven by two drivers. First, fixed systems structures require prolonged reconfiguration times or even prevent these modifications.

TABLE 3.1: Feature benchmarking of manufacturing systems, taken from [113]

| | DMS | FMS | CMS | RMS |
|---|---|---|---|---|
| Cost per part | Low | Reasonable | Medium | Medium |
| Demand | Stable | Variable | Stable | Variable |
| Flexibility | No | General | General | Customised |
| Machine structure | Fixed | Fixed | Fixed | Changeable |
| Product family formation | No | No | Yes | Yes |
| Productivity | High | Low | High | High |
| System structure | Fixed | Changeable | Fixed | Changeable |
| Variety | No | Wide | Wide | High |

A stark example is provided by DMS that are designed to satisfy high demands for a given product [114]. Second, systems' structures need to achieve competing unitary costs and throughput times for a large variety of final goods [115]. Cellular manufacturing systems (CMS) address some weaknesses by leveraging product families dependent on working cell configurations. However, this process design ensures competing unitary costs with long lifecycles and stable market demands. RMS overcome these limitations by dynamically adjusting its output capacities and system structure with respect to unforeseen market changes while ensuring competitive market costs [113, 114, 115, 116]. Tab. 3.1 benchmarks these production paradigms highlighting RMS as the best candidate to compete in modern markets. RMS versatile structure is granted by six core features, where modularity and scalability are the most investigated ones [113, 116]. The former targets the compartmentalization of production units that can be combined together in production schemes while the latter underlines the ability to modify productive capacities.
In this scenario, data-driven approaches to monitor and optimize RMS are mostly limited to heuristic and clustering-based optimization problems [117]. These approaches define objective functions to be either minimized or maximized given a set of constraints [118]. Although the tangible operational benefits for RMS, these solutions are often based on static parameters leading to potentially time-consuming algorithms rearrangements. Another major limitation is not to model the human factor stochastic behavior in processes' executions. This Chapter fills these limitations by presenting and validating a CPS that embraces the challenge of having a versatile structure to reduce deployment time in different RMS configurations. Based on this, RTLS measurements are processed by an operation and layout-insensitive ML-based cyber layer. A further improvement compared to the contribution presented in Chapter 2 is the ambition to differentiate between workers' value-added and non-value-added manual operations. Value-added operations occur whenever workers perform process driven operations such as screwing work-in-progess products.

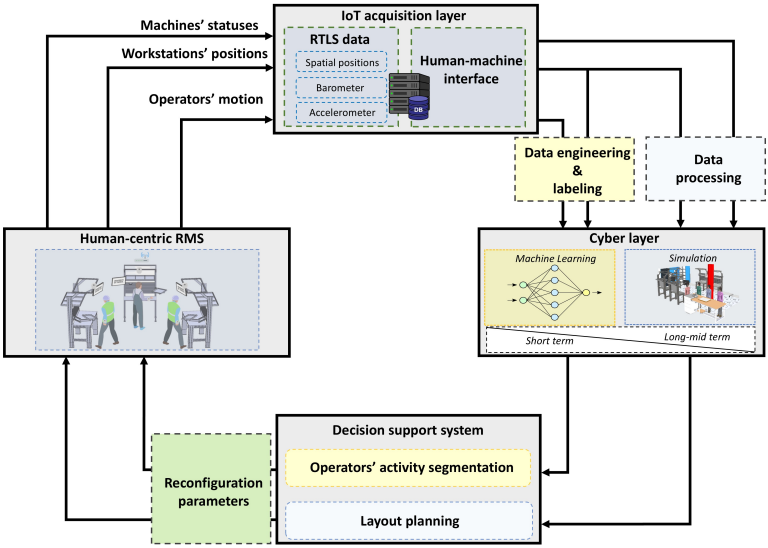


FIGURE 3.1: Cyber-physical system to monitor and manage human-centric reconfigurable manufacturing systems

## 3.1 Cyber-physical system for reconfigurable manufacturing systems

This section presents the innovative proposal of this Chapter. This digital solution is developed to support decision-makers in managing and designing dynamic human-centric RMS. In particular, a specific set of enabling technologies is exploited to enhance these production environments with two different planning horizons. While the short-term one focuses on in-plant performances and interdependencies of production setups, the long mid-term planning horizon leverages simulation environments to iteratively assess the best layout configuration.

To meet these complementary goals, this CPS consists of four conceptual entities (Fig. 3.1). The first one targets whichever labor-intensive RMS that may adjust its functioning and layout configuration based on market demands and product batches. Instead of managing these complex environments based on plant managers' experience, an IoT acquisition layer is introduced to digitize processes' executions. While an RF-based RTLS acquires motion patterns and spatio-temporal

information of workers and industrial resources (e.g., WS), machine interfaces mirror ongoing automation-based production processes. These data streams after specific pre-processing computations are fed into the third system's entity, the cyber-physical layer. Based on the desired planning horizon, two consecutive computations occur. On one hand, ML-based algorithms leverage positioning measurements to detect HPIs and thus segment operators' activities. Following a post-processing step, these outputs automatically generate KPIs upon which plant supervisors can monitor processes' functioning on the short-term horizon. On the other hand, discrete-based simulation models define iteratively sub-optimal production-specific layout configurations. Interest readers may appreaciate the validated methodology in [50]. The main strength of both computational methods is their layout and task insensitivity. Indeed, these models quickly and seamlessly reconfigure based on WS positioning information. The obtained outputs are post-processed to generate KPIs in a decision support system (see Fig.3.1). Both approaches provide detailed insights into processes' weaknesses suggesting to plant supervisors how to improve the efficiency and interdependencies of human-centric RMS while preserving social fairness according to Industry 5.0 value creation. This work focuses on short-term planning and thus the remaining parts of this Chapter target the yellow boxes in Fig. 3.1.

### 3.1.1 IoT acquisition layer

The IoT acquisition layer leverages a UWB-based RTLS to acquire the motion patterns of workers' and WS' positions in various production set-ups. This spatio-temporal information is strategic to automatically classify workers' operations in human-centric RMS. In particular, the classification is distinguished by two objectives. First, layout-insensitive algorithms assign operators' activities to industrial resources and detect logistic activities (see subsubsection 3.1.2). Second, returned operators' activities are further divided into value-added and non value-added operations (see subsubsection 3.1.2).
To achieve this challenging goal, workers wear anonymous tags on the wrist of their dominant hand to acquire the geometrical location as well as 3D acceleration profile. The positions and orientations of WS are acquired by placing two devices in known locations. In addition to the application, these moving entities differ in time resolutions. The datastreams of workers and WS are sampled at a frequency equal to 10 Hz and 1 Hz, respectively. At the same time, they share the same hardware design. These different time resolutions are chosen because workers' positions are way more dynamic than WS within production set-ups. Indeed, a single position for each WS is used in the data engineering step to pre-process the UWB-based dataset. The main advantages of these sensing units are compact size and a battery lifetime up to one year. In addition, additional sensors such as accelerometers are

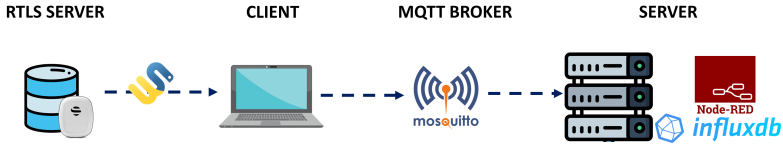


FIGURE 3.2: Conceptual data flow of the IoT acquisition layer

mounted on board. The $3D$ acceleration profiles may represent valuable parameters to learn and identify workers' activity during process executions (subsection 3.1.2). Wearable tags are based on Decawave UWB radio modules and use Channel 5 with a bandwidth of 6500 MHz to exchange JSON messages with anchors using the mentioned refresh rates. In particular, the JSON bodies contain several measurements, namely 3D indoor positions, acceleration profiles, environmental parameters (e.g., temperature and pressure), and a tag ID. The displacement of anchors defines the IoT network reference system and the spatial manufacturing environment to be monitored. Six reference points are installed on the ceiling of an industrial-related pilot environment covering an area approximately equal to $70m^2$. anchors are based on Decavawe modules and an IEEE-compliant UWB transceiver. Connectivity and power supply are granted by a Power over Ethernet (PoE) switch resulting in a star network configuration. Finally, JSON messages are uploaded to an RTLS server (see Fig. 3.2) that determines the unknown position of moving tags through the TDoA geometrical method [103, 119].

Although this network configuration provides a stable data gathering of tagged entities, the RTLS server is a closed web-based application and thus prevents the development of customized algorithms. To overcome this hard limitation, Fig. 3.2 depicts the data flow of positioning information to an external physical server. In detail, the RTLS server is Wi-Fi connected to the Internet using a static IP address. By doing this, whichever client is connected to the Internet can retrieve real-time JSON data through WebSockets API. The client opens as many connections as the number of active tags using threads and locks to avoid unnecessary redundancies. Each connection and thus WebSocket communication is opened and managed by targeting the unique tag ID. Instead of storing data locally, the client node leverages MQTT protocol and publishes positioning datasets in a TLS-encrypted Mosquitto Broker to ensure final users' privacy and avoid data leaks. Therefore, subscribers can authenticate the broker to retrieve JSON data, even in real-time or close to. Since the developed ML-based cyber layer operates with shift-based datasets, these messages are stored in a physical server connected to the Internet. Besides storing measurements in a time-series database (e.g., InfluxDB), a running node-red application parses the JSON messages. It is worth saying that the physical server can be remotely accessed by computational nodes through Secure Shell (SSH) connections.

### 3.1.2 ML-based cyber layer

This section details the ML-based computational steps to perform an activity segmentation of workers' tasks in human-centric RMS. In addition to detecting the performed activities, the cyber layer distinguishes value-added and non-value-added operations. A value-added activity occurs whenever workers perform process-driven activities in industrial resources (e.g., fastening screws). Otherwise, the worker status is idle which is a non-value-added operation. To achieve this challenging task, Fig. 3.3 depicts the closed-loop structure of acquired positioning data in the cyber layer, where the processing steps are associated with the corresponding outputs (e.g., see green-colored boxes). A preliminary overview of these computational steps is listed below:

- **Data Engineering & labeling:** this step increases the dataset dimension by engineering additional features from the acquired motion patterns of workers. In particular, the dataset is distinguished by a relative coordinate system between workers' and industrial resources positions. This feature grants a high degree of adaptability to the computational layer in monitoring any system configuration.
- **Reconfiguration oriented computations:** this ML-based algorithm performs a layout and operator-insensitive classification of logistic activities and assignment to industrial resources (see subsubsection 3.1.2).
- **Operation oriented computations:** this last ML-based step consists of a resource specific approach to classify value-added and non-value-added operations (see subsubsection 3.1.2)

These ML-based outputs are stored in a DSS where callback functions develop KPIs to monitor the performances and the interdependencies of human-centered RMS (see subsection 3.1.3). Based on this overview, the following subsubsections discuss the ML-based approach designed to mitigate limited and sparse datasets. Indeed, collecting a considerable amount of video-based ground truth in industrial environments may raise stakeholders' privacy concerns, from operators to labor unions.

#### Data engineering & labelling

This introductory step downloads the UWB-based datastreams of WS and workers in separate files from InfluxDB (see Fig. 3.2). Before designing the dataset features, an introductory step assesses the positions and orientations of WS for each production setup. The WS 2D positions are determined by averaging the acquired spatio-temporal data. This enables to mitigate the measurement noise of the adopted physical layer. The orientation on the z-axis of these entities is computed through the Arccos of motion vectors using as input both tags' positioning information. While

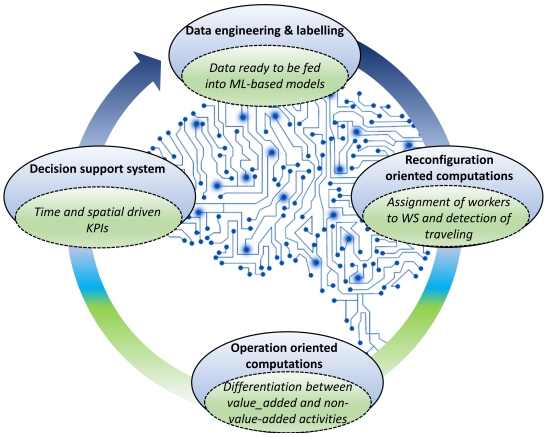


FIGURE 3.3: Conceptual data mining closed-loop of IoT data streams

the initial vector is constructed upon the initial positions of the WS, the final vector underlines the setup location.

At this point, the acquired workers' motion pattern undergoes data engineering and labeling processes. The data engineering step designs the dataset features to facilitate the learning capabilities of ML-based models. Besides raw absolute 2D indoor positions and 3D acceleration profiles parsed from the acquired JSON data streams, a dedicated script computes the relative distances with WS for each positioning frame and worker. This relative coordinate system provides ML-based classifier insensitiveness to production setups (e.g., see subsubsection 3.1.2). Operators' numbers and time-driven information (e.g., absolute clock for each production setup) complete the input features by establishing data relationships among parallel manual operations.

Following this data engineering step, ground truth data (e.g., video recordings) are analyzed to label workers' motion patterns, according to the operation performed. This multi-class classification involves as many labels as the number of WS in the manufacturing system. Traveling and idle states represent two further events to be classified. Based on this, the goal of the following ML-based computations is to perform an activity segmentation of manual task executions in human-centric manufacturing systems and thus offer multidimensional KPIs in a DSS to evaluate the efficiency and interdependencies among industrial resources. Therefore, the first set of ML-based architectures leverages the described dataset features to automatically assign workers to a production resource and detect traveling states (subsubsection 3.1.2). Having as input these classifications, the second step designs WS-dependent algorithms to further detail the proximity of operators to resources into value-added

and non-value-added operations (see subsubsection 3.1.2).

### Reconfiguration oriented computations

To automatically classify workers' proximities to industrial resources and traveling events regardless of production setup layouts, three ML-based algorithms are introduced and benchmarked with each other (e.g., LSTM, Industrial DB scan, and Random Forest). It is worth noting that classifiers' insensitiveness to setups is granted by the data engineering process (see subsubsection 3.1.2), where a relative coordinate system between workers and WS positions is introduced. The following algorithms differ under different perspectives such as the hyper-parameters, and the learning type (e.g., supervised and unsupervised). While the LSTM-based neural network extracts valuable information in the time-series datasets, the Industrial DB scan detects high-density regions of spatio-temporal positioning points and the Random Forest classifies input data using decision trees. These algorithms are discussed in the following paragraphs and Appendix A lists the classifier-specific hyper-parameters to be optimized (see Tab. A1, A2 and A3).

**LSTM-based architecture:** This supervised-based neural architecture follows the definition proposed in [20]. LSTM architectures improve the standard formulation of recurrent neural for the vanishing gradient problem and better capture long-term patterns in time-series analysis [120]. Tab.A1 lists the set of hyper-parameters to be optimized. The core LSTM cell is distinguished by the input, forget, and output gates (see Fig. 3.4). The first updates the cell state by passing in a sigmoid function the input data at timestamp t and the previous hidden state. The closer the output is to 1 the higher informative value occurs in input data. The forget gate is responsible for selecting meaningful information in the cell state at timestamp t. The output of the sigmoid between the previous hidden state and the current input data is multiplied via the Hadamard product with the cell state. While outputs close to 0 suggest that the information can be discarded, values close to 1 indicate meaningful information. Therefore the cell state at timestamp t+1 is given by the sum of potentially discarded information in the forget gate and the output of the input gate. Finally, the output gate is responsible for updating the hidden state to carry forward.

Before feeding data streams into an LSTM-based network, engineered input data are processed by a sliding window algorithm. The dataset is divided into overlapping sliding windows of different sizes (see Tab. A1) and assigns the ground truth-based label to the last input data of the window. Sliding windows are shifted by one sample. In addition, three-dimensional tensors are generated having dimensions equal to the window size, the dataset features, and the batch size. This last parameter enables the computation of the mini-batch gradient and it is adopted to mitigate the vanishing problem during the network training (see Tab.A1). Fig. 3.5 depicts the

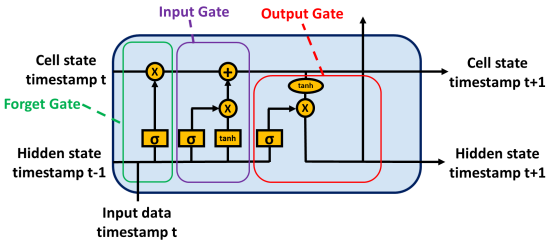


FIGURE 3.4: LSTM cell

LSTM-based architecture that forward propagates input data (e.g., $X_1$ to $X_t$) to be classified. Each layer of the LSTM-based neural network has as many LSTM cells as the window size. The number of layers is an additional hyper-parameter to increase the model's depth and ability to eventually learn complex patterns in input data. Considering an architecture with 2 layers as in Fig. 3.5 , it is possible to approximate the network as a matrix where the number of rows is equal to 2 and columns equal to the window size. Where each matrix entry contains the LSTM cell in Fig. 3.4. For models with more than one layer, the dropout is often adopted to randomly offset some network neurons. This parameter offers a learning regularization and prevents the model's overfitting (see Tab. A1). Another relevant hyper-parameter in designing a robust LSTM-based architecture is the hidden state size (e.g., $h_{11}$, $h_{12}$, etc.). Contrary to the cell state (e.g., $c_{11}$, $c_{12}$, etc.) that stores long-term information, the hidden state carries forward short-term information and overwrites at every timestep. The output of the LSTM cells of the last layer is fed into a fully connected neural network with an output size equal to the number of activities or events to be classified. Finally, a normalized softmax activation function maps the multidimensional vector into the most significant class. After this forward propagation, the deep learning network computes the batch-based gradient using the cross-entropy function and updates the network weights and the learning rate based on the Adam optimization. Tab. A1 lists the initial learning rates.

**Industrial DB Scan**: this unsupervised-based algorithm fills the limitations of its standard formulations as discussed in Chapter 2 [26]. In short, this clustering method detects HPIs as high concentrations of spatio-temporal points in a defined layout region and assigns them to manufacturing systems' industrial resources (e.g., WS). This algorithm does not need to be trained but requires the definition and a static assignment of five spatio-temporal hyper-parameters. Tab. A2 lists them with the related values intervals. First, $d^*$ and $NPts$ provide an initial clustering of human activities during production cycles. While $\epsilon$ defines the distance between geometrical points, NPts define the minimum number of points for each HPI. This last parameter can be seen as a temporal constraint as well. In addition, spatio-temporal points grouped by $\epsilon$ and $NPts$ must be temporally consecutive and thus spaced by

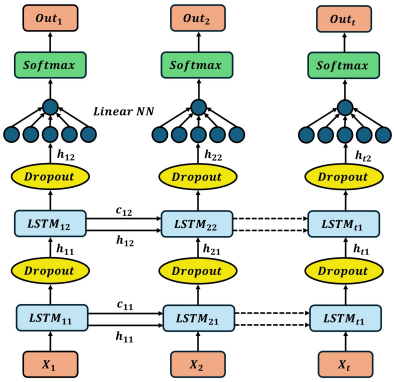


FIGURE 3.5: LSTM-based architecture

$\delta$t. Trivially, $\delta$t is equal to the sampling frequency of the adopted acquisition layer. However, these constraints do not adequately model the measurement noise and motion uncertainties of the IoT acquisition layer and workers, respectively. Indeed, it may be necessary to merge process interactions with each other to avoid skewed KPIs. For instance, let's define two consecutive HPIs (e.g., $C^{w,a}_{z,i}$ and $C^{w,a}_{z+1,i}$). Each interaction is defined by a finite set of positioning points (e.g., $p^{w,a}_{i,f',z}$), a time window (e.g., $ts^{w,a}_{i,f',z}$ and $ts^{w,a}_{i,f^*,z}$), and a geometric center (e.g., $O^{w,a}_{z,i} = \{Ox^{w,a}_{z,i}, Oy^{w,a}_{z,i}\}$). Therefore, $C^{w,a}_{z,i}$ and $C^{w,a}_{z+1,i}$ are merged togheter whether the Eq. (3.1) is true and at least one between Eq. (3.2) and (3.3) is met.

$$ts^{w,a}_{i,f',z} - ts^{w,a}_{i,f^*,z} \leq \alpha \tag{3.1}$$

$$EuclideanDistance(p^{w,a}_{i,f^*,z}, O^{w,a}_{z+1,i}) \leq \beta \tag{3.2}$$

$$EuclideanDistance(p^{w,a}_{i,f^*,z}, p^{w,a}_{i,f',z+1}) \leq \phi \tag{3.3}$$

Tab. A2 shows the hyper-parameters considered in the previous equations, namely $\alpha$, $\beta$ and $\phi$. While $\alpha$ depends on the average time spent to travel from $C^{w,a}_{z,i}$ and $C^{w,a}_{z+1,i}$, $\beta$ and $\phi$ are functions of the expected distance from consecutive process interactions. Once again, interested readers can find the extended formulation in Chapter 2. List of Symbols sums up this algorithm's the indeces and parameters.

**Random Forest:** this supervised-based algorithm has a structure based on decision

trees [121]. The number of tree to be ensembled together is given by the hyper-parameter estimator number (see Tab. A3). Each tree computes the output class for any measurement in the training set. Several parameters influence the size and depth of these estimators. Among them, the minimum sample split defines whether a tree node is further split. The node is split if the number of samples in the node is less than the minimum (see Tab. A3). Otherwise, that node represents a leaf. The output of all decision trees is considered to determine the final output class. This process is known as aggregation and is based on majority voting. Trees models are diversified based on two different methods. First, bagging or bootstrap avoids model overfitting by reducing the sensitivity of training data. Therefore, each decision tree is provided with a sample of data with random replacements in between. Second, feature randomness differentiates the branches of trees' nodes enabling a better classification of datasets. Each decision tree chooses randomly a maximum amount of features based on *sqrt* or $log2$ (see Tab. A3). Finally, the loss function to be minimized during the training process is given by the entry criterion in Tab. A3.

### Operation oriented computations

This computation leverages the output of the previous classifiers bundled with the same feature space to train industrial resource-specific classifiers. In detail, assignments to industrial resources are further distinguished into value-added and non-value-added activities. Value-added operations groups events in which workers are performing manual tasks assigned in industrial resources. This computational step targets a binary classification and reduces algorithm complexity during the learning stage. In addition, it is particularly effective and practical in industrial environments where companies require ready-to-deploy solutions and privacy concerns combined with potential interference with processes' executions may limit extensive ground truth data gathering. Indeed, achieving representative datasets for human motions is a challenging task, especially in diversified workforces and heterogeneous manual operations. To achieve this ambitious aim, three different ML-based classifiers are benchmarked with each other, namely Random Forest, Gradient Boosting, and Support Vector Machine. The Random Forest algorithm discussion is not repeated since it follows the same formulation given in subsubsection 3.1.2. In addition, Appendix A lists the classifier-specific hyper-parameters to be optimized (see Tab.A3, A5 and A4).

**Gradient Boosting:** similarly to the Random Forest, this supervised-based algorithm exploits ensemble learning method, where decision trees or estimators are trained as base learners and then leveraged to achieve input classifications (see Tab.A5). In addition, this classifier adopts the boosting techniques by learning in a sequential manner decision trees. Therefore, the initial and highly biased model is further complicated by adding more trees to minimize the residual error between actual and predicted values. The error is computed through the derivative of the

squared logarithmic loss function with respect to the predicted value. In addition, the learning rate controls the importance of new trees added to the model during the classification process. Tab. A5 defines the set of hyper-parameters to be optimized, where the maximum features and the minimum sample splits follow the same definitions of the Random Forest classifier.

**Support Vector Machine:** this supervised-based algorithm is widely used for classification problems even though the training time exponentially increases with large datasets. The objective of this ML-based classifier is to define the optimal hyperplane that best differentiates input data streams' features. Data closest to the hyperplane are support vector points and their distances are the margins. The hyperplanes are computed based on similarity scores between pairs of training data. These scores are computed by choosing the preferred Kernel, where the Gaussian is one of the most popular [122]. During the training process, two hyper-parameters need to be optimized (A4). First, $C$ can be seen as a model's regularization parameter by controlling the cost of misclassifications. Indeed, it trades off between correct classifications and the margin dimension. While to large value of $C$ is associated with a small margin, the opposite scenario occurs with low $C$ values. In this latter case, the probability of misclassifying data increases. Second, $\gamma$ defines the influence level of a single training example with all the others. High values suggest a close influence between data points.

### 3.1.3 Decision Support System

Based on the closed-loop computations of the cyber layer (see Fig. 3.3), Tab. 3.2 lists how the segmented workers' activities are stored before computing the multi-dimensional KPIs to monitor and manage human-centric manufacturing systems. In particular, the data engineering & labeling step acquires the JSON data of the UWB-based RLTS and then extracts the dataset features to be fed in the following two ML-based computations. While the reconfiguration oriented classifies logistic activities and assigns workers to industrial resources regardless the production setup, the operation oriented computation differentiates between value-added and non-value-added manual operations for each WS.

TABLE 3.2: Example of time-dependent working operation of workers within a production setup

| Start | End | Duration [sec] | Operation | Resource | Distance [m] |
|---|---|---|---|---|---|
| 10:06:26.47 | 10:06:46.09 | 19.62 | Value-added | WS2 | 0 |
| 10:06:46.76 | 10:06:51.36 | 4.60 | Non-value added | WS2 | |
| 10:06:51.59 | 10:06:53.83 | 2.15 | Traveling | - | 4.7 |
| ... | ... | ... | ... | .. | ... |
| 11:31:03.58 | 11:31:11.41 | 47.83 | Value-added | WS4 | 0 |

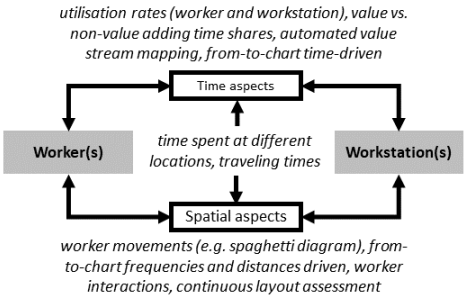


FIGURE 3.6: Multidimensional KPIs embedded in the Decision Support System

The first three columns of Tab.3.2 outline the time-driven features of detected manual operations by storing the time window timestamps and the related duration. Working activities are classified by the operation and resource entries. While the first distinguishes between operation type (e.g., value-added and non-value-added), and traveling activities, the resource column specifies the industrial resource. The last column specifies the meters traveled between two temporally consecutive process interactions. Although this RTLS-based activity segmentation of workers' operations enriches the visibility of in-plant operations, it is impractical to effectively monitor the performances of human-centric RMS. To fill this gap, customized callback functions enable user-friendly decision-making facilitating innovative insights into the interaction of workers and WSs in flexible manufacturing systems. This is related to time and spatial aspects as well as the combination of both. Fig. 3.6 provides an overview of considered KPIs and analysis items towards advanced decision support use cases for monitoring, planning, and improving manufacturing systems. For instance, industrial plant supervisors visualize the most utilized resources while understanding the allocation of operators to industrial resources. In general, these indicators extensively evaluate value-added activities to detect inefficiencies or bottlenecks in reconfigurable environments. Based on this level of detail, decision-makers have pivotal insights to reconfigure the process to achieve scheduled efficiencies. At the same time, the multi-dimensional from-to charts highlight the resources' interdependencies and the most exploited workers in material handling activities during production processes. This level of analysis is extremely beneficial for managers. First, they may aim to achieve fair RMS by equally involving workers in handling activities. Second, data-driven layout redesigns may increase the operational efficiency of human-centric RMS. Therefore, as clear advancements towards the state of the art, the suggested approach is flexibly adapting to changing manufacturing layouts and situations and enables an innovative breakdown of manufacturing activities (e.g. into value and non-value-adding time shares).

FIGURE 3.7: Static viewpoint of the industrial related reconfigurable pilot environment

## 3.2 Cyber-physical system validation

This section validates the digital system to monitor human-centric RMS based on ML-based models. In particular, subsection 3.2.1 describes the industrial-related pilot environment where the workers' motion patterns and WS positioning information are acquired by a UWB-based RTLS. The obtained dataset consists of 8 manufacturing configurations, where a spinal prosthetic model is the final product to be assembled by exploiting various industrial WSs, operators, and task assignments (subsection 3.2.2). Finally, the remaining subsections 3.2.3 and 3.2.4 present the ML-based performances of the reconfiguration and operation oriented computations. These intelligent classifiers are trained and tested in a remote Jupiter server running in a Dell PowerEdge R740 with an Intel Xeon Platinum 8468H and RAM 256Gb.

### 3.2.1 Reconfigurable case study

The industrial-related pilot environment assembles a medical spinal prosthetic sample in different industrial resources, where one of them hosts a collaborative robot (see Fig. 3.7). WS are equipped with industrial screwdrivers and a fixed storage location that stocks components and fasteners. The manufacturing process requires fully assembling 3 final products by performing a wide range of tasks. Based on operators' experience, the entire production takes between 15 and 20 minutes. First, 8 blocks are glued together in pairs and thus drilled. Each block is distinguished by 4 holes. Subsequently, these blocks are fit into the prosthetic frames and screwed by industrial drivers. The third step screws together the prosthetic halves to achieve the final product. The production cycle ends with screwing quality tests. Based on this assembly process, 8 different production setups have been performed varying the number of WS, the task to WS assignment, and the workers involved. Although this human-centric RMS may accommodate high product variances at affordable costs, a process monitoring based on supervisors' experience

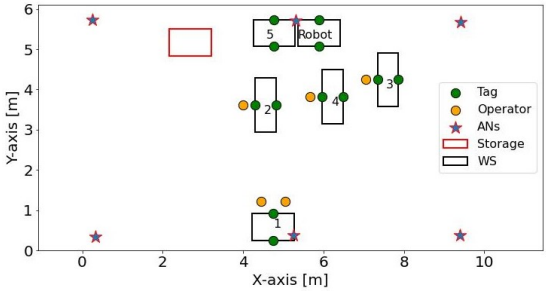


FIGURE 3.8: Seventh production set-up

and human commitment results in unrepresentative analysis and thus underperforming decision-making. To avoid these managerial weaknesses, the overall goal is to design a CPS that performs an activity segmentation of workers' tasks by distinguishing them into value-added and non-value-added, regardless of the different industrial setups during a pilot production of the medical prosthetic. In particular, the computational layer needs to be layout and operation-intensive to ensure easy-to-deploy in-plant monitoring. Based on this, a UWB-based RTLS acquires workers' motion patterns and industrial WS locations in the production environment. As depicted in Fig. 3.8, six anchors are deployed in the ceiling of the monitored industrial-related pilot environment at known positions. These reference points are connected to a PoE switch that provides a stable power supply and a local network. Based on the description of the industrial use case, the following subsection describes the feature-engineered dataset of workers' motion patterns during the spinal prosthetic assembly in 8 production setups. Each manufacturing configuration is implemented twice on different working days.

### 3.2.2 Feature-engineered workers' motion patterns

This subsection describes the operator-specific datastreams that are fed into the ML-based cyber layer. The global dimension of the dataset is equal to 814065 samples. These time-driven motion patterns are acquired in 8 production setups involving a total of 41 different workers. In this regard, Tab. A6 in Appendix A specifies the setup-dependent WS' absolute 2D positions and the number of operators. Since less than 25% and 40% of production setups involve 5 and 6 workers, the vast majority of input data is held by the first four operators. Tab. A7 lists the gathered input data for each operator number. The collected video-based ground truth enables frame-oriented data labeling and thus 9 different classes are adopted to distinguish workers' operations during production processes. This supervised and time-consuming

process deeply affects the deployment time of ML-based models. A possible and viable solution to slash down data labeling times is to run a time-dependent script that assigns real-time labels to workers' operations based on keyboard entries of numbers. However, this approach requires the supervision of each worker-dedicated running script and thus it is not implemented due to the shortage of researchers. The classes from *WS*1 to *WS*5 underline process-specific working activities in these WS. Similarly, *Robot* and *Storage* suggest human-automation interactions and the picking of raw materials and components (e.g., fasteners). The *Idle* class is introduced to group all non-value-added operations regardless of the spatio-temporal positions within 8 production setups. Fig. 3.9 outlines using boxplots the distributions of the discussed industrial classes among production setups. The *Idle* state represents the majority of events in this highly unbalanced dataset with a median value equal to 27.27%. The maximum and minimum values account for 51.48% and 15.87%, respectively.

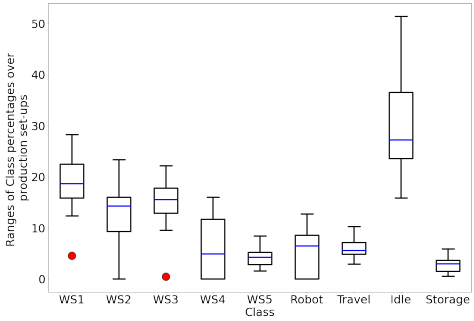


FIGURE 3.9: Dataset classes distributions in percentage

While the maximum is connected to the second production setup during the first recording day, the lower bound is registered in the fourth production setup and second recording day. The higher bound is markedly affected by the Operator 6 operations that are non-value-added for the 88.89% of his/her production time. The other most populous classes are *WS*1, *WS*2 and *WS*3 peaking at 28.3%, 23.42% and 22.23%, respectively (see Fig. 3.9).

Considering the challenging target of designing a configuration and operation insensitive architecture, an additional data investigation targets the distribution of acceleration profiles. Therefore, *Working* and *Idle* represent the newly formed operators' states under analysis. In particular, the *Working* state groups workers' value-added datastream in whichever WS and production set-up. Fig. 3.10 shows the 3D distributions of acceleration profiles in the mentioned operator states. It is worth

noting that these distributions have overlapping patterns and the underlying one and multi-way ANOVA tests are distinguished by really weak p-values. This scenario confirms the null hypothesis and may be driven by two main factors. First, the dataset dimension fails to generalize both workers' motion patterns and the performed manual operations. However, it may be difficult to extensively acquire ground truth information in industrial use cases due to privacy concerns [26]. Second, the IoT acquisition layer is required to increase the sampling frequency to obtain higher resolutions in acceleration motion patterns [123]. To mitigate the dataset sparsity and the low resolution of acquired accelerations, the proposed ML-based cyber layer mines value inside data using a two-step approach. First, state-of-the-art algorithms assign workers to industrial resources (e.g., WS and storage location) and detect logistic activities (see subsubsection 3.1.2). However, this computational step approximates any WS proximity to value-added operations. Therefore, the second computational step fills this gap by performing a binary classification between *Working* and *Idle* states (see subsubsection 3.1.2). Six different ML-based classifiers are trained to learn meaningful motion patterns from $WS1$ to the robotic WS. The performances of these two computational steps are described in the following subsections 3.2.3 and 3.2.3.
Regardless of the different targets of these computational algorithms, the dataset is split into three sets, where the validation has a share equal to the 70% of the dataset and the remaining two (e.g., validation and test) accounts for 15%. Production set-ups in recording days are assigned entirely to one of these sets and are not duplicated. In particular, the test set contains datastreams of the 7-th production setups during the second recording day. Fig. 3.8 shows the layout configuration of this setup as well as the number of workers. In addition, the bold entry in Tab. A6 of Appendix A outlines the absolute WS positions and number of workers for this production setup. In particular, the $WS1$ dedicated workers glue and drill the blocks to be inserted in prosthetic frame halves. Then, the righter worker of $WS1$ is in charge of moving finished products in $WS2$, $WS3$, and $WS4$ where prosthetic halves are fully assembled. The production process ends using the robotic arm to screw together the prosthetic halves to achieve the final product. This process is remotely controlled from $WS5$ where an automated final inspection of products is performed.

### 3.2.3 Performances of reconfiguration oriented computations

This subsection validates the first step of the ML-based computations (see subsubsection 3.1.2), where the hyper-parameters optimized classifiers are benchmarked with each other. Before going through the performance metrics (Fig.3.11 in Appendix A and Tab. 3.3), it is worth describing the adopted data splitting approach.

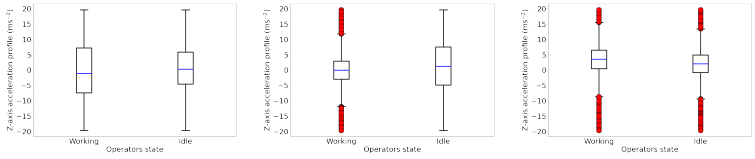


(A) X-axis acceleration distribution (B) Y-axis acceleration distribution (C) Z-axis acceleration distribution

FIGURE 3.10: Distributions of 3D acceleration profiles of UWB-based tags on operators' hand

On the one hand, the supervised learning approaches (e.g., LSTM-based architecture and Random Forest) are trained on 70% of the entire dataset. The remaining input data are equally split into the validation and the test sets. In particular, production setups are randomly assigned to the mentioned dataset splits, preserving their temporal dependence. The seventh production setup during the second recording day and the second setup on the first recording day belong to the test set. On the other hand, the Industrial DB scan does not require training and thus the following performances are evaluated both on the 7th production set-up and on the entire dataset. Tab. 3.3 depicts these performances, where values between brackets relate to the entire dataset. Regardless of the classifier, three different metrics (see Eq. from (3.4) to (3.6)) benchmark the classification performances of the presented ML-based algorithms.

$$Precision = \frac{TP}{(TP + FP)} \tag{3.4}$$

$$Recall = \frac{TP}{(TP + FN)} \tag{3.5}$$

$$Micro\ F1 - score = \frac{TTP}{TTP + \frac{1}{2} * (TFP + TFN)} \tag{3.6}$$

The first two class-dependent metrics are functions of TP, FP, and FN. While Precision measures results' relevancy, the Recall indicates how many truly relevant results are returned. The Micro F1 score is chosen as a global metric due to its ability to better reflect imbalanced data distributions (see Fig. 3.9). Where TTP, TFP, and TFN are derived by summing up the related class-dependent metrics (e.g., TP, FP, and FN).
Regardless of the intrinsic differences of ML algorithms, Fig.3.11 (a) shows promising Micro F1 scores for all classifiers. In particular, the Random Forest and Industrial DB scan represent the worst and best-performing approaches accounting for

0.82 and 0.87, respectively. However, this global metric fails to highlight the class-specific strengths and weaknesses of these models. To fill this gap, the performance evaluation of this computational stage starts with the Pytorch-coded LSTM-based neural network. Based on the hyper-parameters in Tab. A1, the optimal network configuration is iteratively assessed. Batch, window, and hidden sizes are equal to 64, 128, and 256. The model is distinguished by solely one LSTM layer and thus the dropout is not introduced. Finally, the learning rate is equal to $1e^{-4}$. Fig. 3.11 (b) shows the Cross-Entropy-based loss for both the training and validation set over 300 epochs. While the training loss starts at 1.21 its profile over epochs decreases to meet convergence at 0.01, the validation Cross-Entropy opens at 2.62, and the loss is distinguished by fluctuations over training epochs. In addition, after reaching the local minima equal to 0.34 at epoch 49, the validation curve increases to 0.72. Since this scenario may indicate model overfitting, Fig. 3.11 (c) depicts the Micro F1 scores within data splits over model epochs. Although the training F1 score is approximately equal to 1 from epoch 94 on-wards, the validation and test set have similar profiles and do not shrink. The 111-th model epoch with related learned weights maximizes the test F1 score accounting for 0.86 (see Fig. 3.11 (a)). Fig. 3.11 (d) shows the confusion matrix related to this model epoch, where the main diagonal contains the correct classified datastreams. Before analyzing the confusion matrix, it is worth stating that this computationally expensive architecture is distinguished by an inference time equal to 90 seconds for each training epoch and a test time approximately of 38 seconds.

The confusion matrix suggests that the vast majority of dataset classes present low misclassification dispersion (e.g., FP and FN). Indeed, WS apart from *WS4* and the *Storage* present Micro F1 scores ranging from 0.82 to 0.98 (see Tab. 3.3). However, WS4 and Travel classes are distinguished by underperforming F1 scores accounting for 0.63 and 0.48, respectively (see Tab. 3.3). On the one hand, the Precision and Recall of the fourth WS are equal to 0.84 and 0.51 leading to class underestimation due to a high amount of FN. This scenario is driven by a limited representation of this class in the dataset. Indeed, the class shares range from 1.31% to 15.72% within production setups (see Fig. 3.9). In addition, half of production environments do not exploit *WS4* during the prosthetic assembly. On the other hand, the *Travel* class shows low values for Recall and Precision. This scenario is driven by narrowed production setups where the UWB-based RTLS is stressed with short distances between manufacturing WS (see Tab. A6).

The second classifier is the Industrial DB scan. The model's hyper-parameters are shared and have the same values as the first algorithm definition and validation proposed in [26]. In particular, $\epsilon$, $NPts$ and $\delta t$ are equal to 0.17 meters, 15 positioning points and 10 Hz. The measurement noise and motion uncertainty-driven hyper-parameters, namely $\alpha$, $\beta$, and $\phi$ account for 1 second and 0.5 meters. Based

on this hyper-parameters selection (see Tab. A2), the Micro F1 score of the 7th production set-up is equal to 0.87. Fig. 3.11 (e) shows the related confusion matrix for this targeted multiclass problem. This clustering method presents a computational time equal to 72 seconds for each operator in the considered production setup. Similarly to the LSTM-based network, the F1-score of industrial resources from $WS1$ to $WS5$ ranges from 0.80 to 0.95. It is worth noting that the $WS4$ F1-score accounts for 0.94, markedly higher than the one obtained with the LSTM-based architecture (see Tab. 3.3). A different scenario emerges for the *Storage* class where the neural network architecture outweighs this density-based method. Indeed, an underperforming Recall value provides an F1 score equal to 0.54. This low statistic is driven by a relevant limitation of the Industrial DB scan. The definition of static hyperparameters may not reflect different positioning accuracies of the UWB-based IoT acquisition layer in manufacturing systems' local regions. In the targeted industrial-related pilot environment, such a scenario emerges for x and y values ranging from 0 to 3 and from 3.75 to 6 meters, respectively (see Fig. 3.8). Both classifiers are distinguished by weak capabilities in detecting logistic activities in the mentioned industrial-related pilot environment due to narrowed distances between WSs (see Tab. 3.3 and Tab.A6).

The last classifier to detect reconfiguration-oriented operations is the Scikit-learn-coded Random Forest. The optimal hyperparameters configuration is found using the grid-search algorithm. This sub-optimal configuration is distinguished by a number of estimators and minimum sample splits equal to 70 and 3, respectively. In addition, the optimal criterion and maximum features are given by *entropy* and the *sqrt*. Fig. 3.11 (f) depicts the related confusion matrix that provides a Micro F1 Score equal to 0.82. The described training and test times are equal to 140 and 15 seconds, respectively. Although this classifier is the worst performing in detecting manufacturing operations, $WS1$ and $WS5$ F1 scores outweigh the previous two computational methods. Overall, this statistic for the other classes is satisfactory apart from $WS4$ and *Travel*. While the first confirms the limitations already analyzed with the LSTM-based model, the logistic activities are a shared weakness of all benchmarked intelligent algorithms (see Tab. 3.3).

TABLE 3.3: Performances of optimized classifiers for reconfiguration oriented computations

| Class | LSTM architecture | | | Industrial DB scan | | | Random Forest | | |
|---|---|---|---|---|---|---|---|---|---|
| | Precision | Recall | F1-score | Precision | Recall | F1-score | Precision | Recall | F1-score |
| *WS1* | 0.96 | 0.89 | 0.92 | 0.95 (0.93) | 0.96 (0.92) | 0.95 (0.92) | 0.98 | 0.97 | 0.97 |
| *WS2* | 0.96 | 0.97 | 0.96 | 0.96 (0.97) | 0.94 (0.90) | 0.95 (0.93) | 0.97 | 0.79 | 0.87 |
| *WS3* | 0.92 | 0.95 | 0.94 | 0.93 (0.90) | 0.86 (0.88) | 0.89 (0.85) | 0.96 | 0.88 | 0.92 |
| *WS4* | 0.84 | 0.51 | 0.63 | 0.96 (0.90) | 0.94 (0.95) | 0.95 (0.92) | 0.97 | 0.56 | 0.71 |
| *WS5* | 0.85 | 0.81 | 0.83 | 0.76 (0.70) | 0.85 (0.90) | 0.80 (0.79) | 0.91 | 0.97 | 0.93 |
| *Robot* | 0.74 | 0.91 | 0.82 | 0.88 (0.81) | 0.81 (0.88) | 0.85 (0.84) | 0.94 | 0.69 | 0.80 |
| *Travel* | 0.44 | 0.53 | 0.48 | 0.45 (0.5) | 0.62 (0.70) | 0.52 (0.58) | 0.19 | 0.63 | 0.29 |
| *Storage* | 0.94 | 0.89 | 0.92 | 0.98 (0.90) | 0.47 (0.45) | 0.64 (0.60) | 0.96 | 0.83 | 0.89 |

After this quantitative discussion on class-specific performances, the LSTM-based

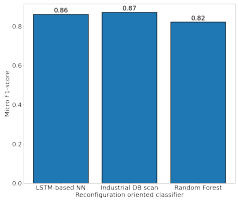


(A) Micro F1-scores of the reconfiguration oriented classifiers

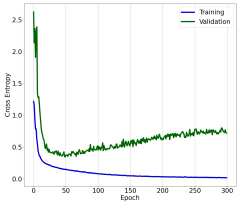


(B) Cross Entropy losses optimized LSTM-based architecture

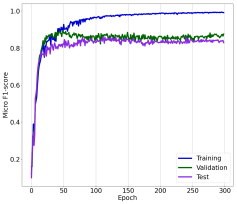


(C) Micro F1-Scores optimized LSTM-based architecture

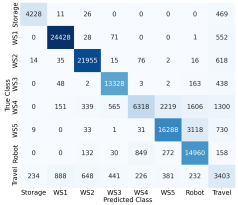


(D) Confusion matrix optimized LSTM-based architecture

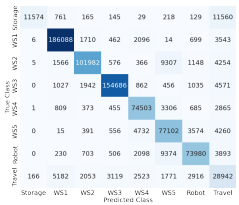


(E) Confusion matrix optimized Industrial DB scan

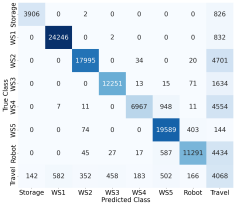


(F) Confusion matrix optimized Random Forest

FIGURE 3.11: Performances of ML-based classifiers of reconfiguration-oriented computations

neural network is chosen over the Industrial DB scan for a main reason. It is preferable to achieve a better Micro F1-score for the *Storage* class rather than in *WS4* which is hardly used in the considered manufacturing process (see Fig. 3.3). Despite the adopted model selection to maximize classification performances, the following Tab. 3.4 provides an additional and useful distinction of the benchmarked ML-based classifiers. The listed features may guide practitioners in implementing the most adequate model based on their needs and requirements. For instance, the Industrial DB scan represents the most effective solution with a limited dataset and related ground truth baseline information. In addition, this density-based computational method does not require training and thus the deployment time solely relies on the identification of a sub-optimal hyper-parameters values set.

TABLE 3.4: Qualitative benchmark of reconfiguration oriented ML-based methods

| Classifier | Training | Deployment Time | Number of hyper-parameters | Dataset size |
|---|---|---|---|---|
| LSTM-based architecture | Yes | High | High | Large |
| Industrial DB scan | No | Low | Low | Small |
| Random Forest | Yes | Low | Medium | Medium |

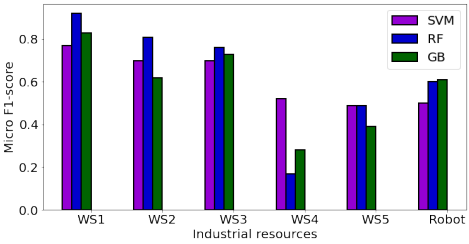


FIGURE 3.12: Micro F1-scores of the operation oriented classifiers

### 3.2.4 Performances of operation oriented computations

This subsection discusses the performances in classifying working and idle activities, given the industrial resource (see subsubsection 3.1.2). To do so, three grid search optimized (see bullet point in Appendix A) ML algorithms are trained using a resource-specific dataset with test sets' dimensions varying from 7.3% to 17.5% (e.g., $WS5$ and $WS2$ represent the lower and upper bound). This computational step considers solely data streams acquired during the second recording day due to reduced exposure to motion uncertainty in workers' assembly activities. Considering computational times, the Support Vector has markedly higher statistics compared to the other two models. Indeed, the Gradient Boosting and the Random Forest are distinguished by mean and standard deviation training times equal to 35 and 5 seconds, respectively. The same statistics for the Support Vector account for 11.5 and 2.2 minutes. The related mean and standard deviation for the inference shrinks to 2.5 minutes and 70 seconds.
Fig.3.12 shows the industrial resources-centered (e.g., from $WS1$ to *Robot*) Micro F1-scores in identifying value-added and non-value-added activities. The acronyms SVM, RF, and GB refer to Support Vector Machine, Random Forest, and Gradient Boosting methods to limit space. Overall, the first three WS are distinguished by markedly higher Micro F1-scores compared to the remaining others. This scenario is driven by the nature of tasks allocated to WS. Indeed, the most manual-intensive activities such as drilling blocks and screwing them into the model's frame are usually assigned to $WS1$, $WS2$, and $WS3$. Based on this, two algorithms are selected to differentiate workers' status (e.g., *Working* and *Idle*) in industrial resources. While the Random Forest is the most appropriate method for the first three WSs, Gradient Boosting shows better capabilities in the remaining WSs where operators' motion patterns are limited.

Starting the discussion with the most manual-intensive industrial resources, the Random Forest Micro F1-score values of $WS1$, $WS2$, and $WS3$ are equal to 0.92,

0.81, and 0.76, respectively (see Fig. 3.12). These promising statistics are also reflected by analyzing the resources and operator state-driven Precision, Recall, and F1-score metrics (see Tab. 3.5). In particular, the Random Forest algorithm outperforms the other methods showing deltas up to 0.49. A stark example is provided by the Recall values of non-value-added activities in WS1 (see Tab. 3.5).
A different scenario emerges for the remaining industrial resources from the fourth WS to the robotic one. Indeed, the Support Vector Machine and the Random Forest show superior Micro F1-scores compared to the Gradient Boosting algorithm (see Fig. 3.12). For instance, considering $WS4$, the Support Vector accounts for 0.52 compared to 0.28 of the Gradient Boosting. However, Tab. 3.5 suggests that both Random Forest and Support Vector Machine classifiers overfit the data set. In detail, the value-added class for $WS4$ and $WS5$ is never recognized. Based on this, the Gradient Boosting is leveraged as the most adequate classifier to evaluate the operator state in these WS. Despite this selection, the detection capabilities are not satisfactory for two main aspects. First, 3D acceleration profiles present overlapping distributions among *Working* and *Idle* classes, as already pointed out during the dataset description (see subsection 3.2.2). Second, these industrial resources are distinguished by pretty static workers' motion patterns. For example, operators' activities are limited to interaction with the machine interface and highly assisted quality checks in the robotic and fifth WS. To conclude this classifier and resource-oriented discussion, Fig.A1 in Appendix A shows the confusion matrices for each resource and chosen ML-based algorithm.
Benefitting from these sequential ML-based computational steps, a time and label-oriented algorithm segments workers' activities as shown in Tab.3.2. Sequentially, callback functions leverage these outputs to achieve KPIs to monitor the efficiencies and interdependencies of production set-ups.

TABLE 3.5: Performances of optimized classifiers for operation oriented computations

| | | Working | | | Idle | | |
|---|---|---|---|---|---|---|---|
| Industrial Resource | Classifier | Precision | Recall | F1-score | Precision | Recall | F1-score |
| *WS*1 | Support Vector Machine | 0.76 | 0.95 | 085 | 0.81 | 0.38 | 0.53 |
| **WS1** | **Random Forest** | **0.94** | **0.95** | **0.94** | **0.89** | **0.87** | **0.88** |
| *WS*1 | Gradient Boosting | 0.80 | 0.99 | 0.88 | 0.97 | 0.47 | 0.64 |
| *WS*2 | Support Vector Machine | 0.72 | 0.86 | 0.79 | 0.63 | 0.41 | 0.5 |
| **WS2** | **Random Forest** | **0.84** | **0.87** | **0.86** | **0.76** | **0.71** | **0.73** |
| *WS*2 | Gradient Boosting | 0.81 | 0.54 | 0.65 | 0.49 | 0.77 | 0.59 |
| *WS*3 | Support Vector Machine | 0.65 | 0.92 | 0.76 | 0.84 | 0.57 | 0.60 |
| **WS3** | **Random Forest** | **0.72** | **0.89** | **0.80** | **0.84** | **0.63** | **0.72** |
| *WS*3 | Gradient Boosting | 0.68 | 0.89 | 0.78 | 0.83 | 0.56 | 0.66 |
| *WS*4 | Support Vector Machine | 0.82 | 0.55 | 0.66 | 0.16 | 0.43 | 0.23 |
| *WS*4 | Random Forest | 0 | 0 | 0 | 0.17 | 1 | 0.28 |
| **WS4** | **Gradient Boosting** | **0.90** | **0.14** | **0.25** | **0.18** | **0.92** | **0.30** |
| *WS*5 | Support Vector Machine | 0 | 0 | 0 | 0.49 | 1 | 0.66 |
| *WS*5 | Random Forest | 0 | 0 | 0 | 0.48 | 1 | 0.65 |
| **WS5** | **Gradient Boosting** | **0.52** | **0.07** | **0.12** | **0.49** | **0.94** | **0.65** |
| *Robot* | Support Vector Machine | 0.62 | 0.64 | 0.63 | 0.26 | 0.24 | 0.25 |
| *Robot* | Random Forest | 0.68 | 0.72 | 0.70 | 0.41 | 0.37 | 0.38 |
| **Robot** | **Gradient Boosting** | **0.77** | **0.57** | **0.66** | **0.45** | **0.66** | **0.53** |

## 3.3 Results & managerial insights

After the performance validation of the designed ML-based cyber layer, this section discusses the managerial insights and implications of monitoring with IoT technologies task executions in human-centric RMS. The following KPIs embedded in the DSS discusses the performances and interdependencies of the 7th production set-up during the second recording day lasting 16 minutes approximately.
This production setup employs 5 workers to fully assemble 3 spinal prosthetic models resulting in 5.45 minutes/product. Fig. 3.13 shows the utilization ratio of industrial resources as a function of workers' value-added operations over the monitored shift (e.g., ST stands for Storage and ANs for anchors).

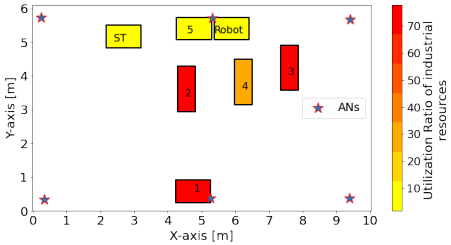


FIGURE 3.13: Utilization of Industrial resources over the monitored shift

The most saturated resources of this production set-up are the first three WS. While WS1 peaks at 77.82%, WS2 and WS3 are distinguished by utilizations equal to 72.31% and 70.22%, respectively. This scenario is driven by the task allocation to WS. Indeed, WS1 hosts manual gluing and drilling of blocks. Subsequently, blocks are moved into three parallel WS (e.g., WS2, WS3, and WS4) that fit two wooden blocks each into the prosthetic model halves. The analyzed KPI demonstrates that WS2 and WS3 are preferred over WS4. This last resource is used as a jolly WS showing a utilization ratio lower than 30%. Based on this first insight, plant supervisors should identify the over-allocation of resources that negatively impact both economic indicators and potential distances traveled by workers to perform production cycles. In this regard, it would be recommended to reduce the number of WSs and eventually assign an additional jolly operator either to WS2 or WS3 to lower potential bottlenecks and operators' efforts to meet required takt times. The remaining industrial resources are distinguished by low utilization lower than 10%. The quality control in WS5 and the human-robot interactions represent quick and less labor-intensive tasks. Although this KPI highlights potential redundant WS in production set-up, it falls short in segmenting workers' operations over the shift. Fig. 3.14

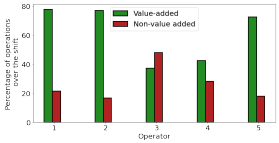


(A) Distribution of operator-centric operations

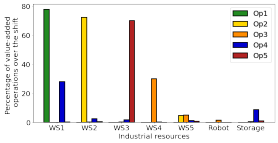


(B) Distribution of value-added operations among operators and resources

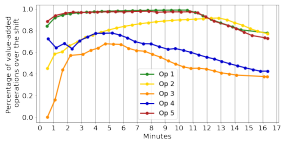


(C) Operator specific percentage of value-added operations over the shift

FIGURE 3.14: Activity segmentation of workers operations

(a), (b) and (c) fill this gap by highlighting the distribution of value-added and non-value-added operations as well as the operators' assignments to WS. First, Fig. 3.14 (a) outlines the operator-centric distributions of value-added and non-value-added operations as a function of the shift duration. This KPI is extremely effective in pointing out the most under-saturated workers in performing process-related activities. While Op1, Op2, and Op5 register shares of value-added operations greater than 72%, Op3 and Op4 are distinguished by values equal to 37.42% and 42.57%, respectively. Although this first overview may suggest an over-allocation of workers to the production setup, further metrics are required to carefully analyze this working shift. Second, Fig. 3.14 (b) depicts the value-added activities performed by operators among the seven industrial resources of this production set-up. This metric enables to differentiate operators' tasks. While Op1 and Op2 value-added operations never below 72% are limited to WS1 and WS3, the remaining operators are way more dynamic showing interactions with multiple resources. Op3 and Op4 represent striking examples and provide additional details into the process's functioning. On the one hand, the distribution of Op3 value-added activities suggests that low productivities of WS4 are integrated with quality checks and robot interactions. On the other hand, Op4 interacts with almost all industrial resources of the manufacturing system, where an 8.77% of time is reserved by picking activities from the storage location. This insight may suggest that this worker is also in charge of manual material handling operations among industrial resources. Third, Fig. 3.14 (c) further details workers' value-added operations by evaluating their share in production routines using a time resolution of 30 seconds. This KPI notifies plant supervisors of potential workers' over-allocations to production set-ups.

Although three operators (e.g., Op1, Op2, and Op5) are distinguished by shares of value-added operations greater than the 80% for the majority of the production shift, Op3 and Op4 hardly exceed the 70%. In particular, Op3 is the least involved in value-added activities. Benefitting from these KPIs, decision-makers may reduce the workforce size and re-distribute Op3 tasks to the remaining others, most likely to Op2 and Op5 that share similar operations.In general, workers' over-allocations are detrimental to in-plant performances. First, stagnant outputs per unit of time and operators may penalize workers' commitments and awards during gamification approaches. Second, incorrect systems design in manufacturing systems with interconnected job shops may drastically affect companies' market competitiveness. Besides process-oriented manual operations, it is pivotal to focus on traveling events to discuss the interdependencies among industrial resources. A top-down approach is established to achieve this purpose. Fig. 3.15 shows the distances traveled by monitored workers over the working shift. Op4 travels 3 up to 20 times the distances of his/her colleagues, overcoming 200 meters during the shift. This statistic is consistent with the distribution of value-added activities among operators and resources (see Fig. 3.14 (b)). Indeed, Op4 interacts with almost all industrial resources and spends approximately 10% of his/her working time in the storage location. This distance-dependent statistic negatively affects the social inclusiveness and sustainability of the considered human-centric RMS. This scenario is driven by two main factors. First, an over-allocation of resources with non-optimal positions may lead to longer logistic activities. This can be mitigated by the long-mid term planning horizon of the architecture as discussed in [50]. Second, plant supervisors should be encouraged to redistribute logistic activities among the workforce. This point assumes further relevance when manually handled products present considerable weight and risk scores of ergonomic indices (e.g., NIOSH and EAWS) represent valuable weights to be fed into objective functions [124].

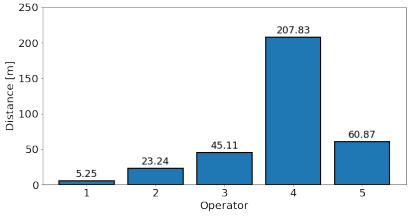


FIGURE 3.15: Distances traveled by operators over the shift

However, not accessing the operator-centric travel activities fails to highlight the most involved resources of production set-ups. Fig. 3.16 fills this gap by depicting the multidimensional from to charts of Op4 in the frequency, time, and spatial domains. It is worth noting that a valid traveling activity between two industrial

resources must contain at least 20 indoor positions. This choice is made to limit the cyber layer's limitations in detecting this event combined with an in-depth process analysis. Starting to analyze the frequency domain, Fig. 3.16 outlines the amount of traveling events or flows among industrial resources.

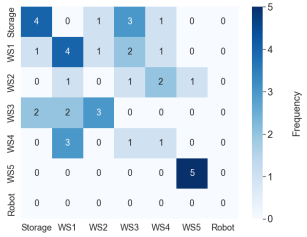


(A) Flow-oriented from to chart


(B) Time-oriented from to chart


(C) Distance-oriented from to chart

FIGURE 3.16: Multidimensional from to charts of Operator 4

It is interesting to note that the 3 out of 5 flows from the storage location are directed to WS3. The same amount of flows from WS3 are then directed to WS2. Analyzing the global picture, WS2 and WS3 are distinguished by a higher amount of incoming and outgoing flows compared to WS4. This flow distribution confirms the utilization ratio of WS4 in this production set-up. Fig. 3.16 (a) confirms that Op4 handles the replenishment of WS2, WS3, and WS4 while feeding to them the blocks to be screwed in the prosthetics halves. Scaling the same approach to the entire workforce, other material handling activities may be detected and thus analyzed. For instance, Op1 presents solely one travel activity from the storage to WS1. This value points out accurate management of wooden blocks because it suggests that the required wooden blocks to produce 3 final products are moved at once. The logistic activities toward the final stages of the production cycles (e.g. robotic WS and quality check in WS5) are managed by Op3 and thus are not discussed further. To

better analyze process functioning and potential inefficiencies, Fig. 3.16 (b) and (c) link the discussed flows with the aggregated distances traveled and the time spent. For example, 12.7 seconds and 18.3 meters that are registered during the 3 flows between the storage location and WS3 may be reduced by changing the replenishment logic. The advantage of knowing a priori the desired output rate should encourage decision-makers to design an adequate buffer size for each WS. This would enhance the material handling times and distances by avoiding multiple and unnecessary interactions with the storage. Considering the parallel operations of the three industrial resources (e.g., WS2, WS3, and WS4), a shared buffer location may be designed as well to limit obstruction among operators during task executions. Another valuable layout modification is to bring closer WS2 and WS3. By doing this, Op4 would slash down the 14.1 seconds and the 23.5 meters during three traveling events. The same approach can be used with WS1 in bringing it closer to WS2 and WS3.

To conclude, the designed CPS can effectively enhance the visibility of human-centric RMS through different multi-criteria variables. On the one hand, performance driven metrics suggest sub-optimal allocation of WS and workers to production setups. This contributes to improving manufacturing systems' economic metrics while minimizing operators' efforts during manual task executions. In addition, these metrics may be complemented by additional data such as market demands and production batches to create families of production setup designs. On the other hand, investigation of logistic activities suggests potential disadvantaged workers and valuable inputs to heuristic optimization to re-balance traveled distances during production cycles. In addition, operator-centric from to charts pinpoint the interdependencies of industrial resources constituting valuable inputs to re-layout production environments. This twofold level of investigation is crucial to meet human-centric and socially sustainable value creations following tue Industry 5.0 vision.

## Chapter 4

# Digital monitoring of internal logistic operations

"There's gonna be opposition
Ain't no way around it
Well, if you are looking for strong and steady
Well, baby, you found it
We'll weather the coldest nights
Baby, we're a dying breed"
*– The Killers, Dying Breed, 2020*

Internal logistics systems operations face huge complexity as the variance in marketed products continues to increase [125, 126]. This scenario is strongly affected by customer orders and shorter product lifecycles. Mass-customized markets challenge warehousing systems to handle and deliver small-batch size of shipments with high varieties [127]. Among the inbound and outbound activities, the order management represents one of the most stressed warehousing operations [128]. Therefore, logistic supervisors are required to manage and optimize these low-standardized environments in order to reinforce in-plant performances at scheduled levels. However, traditional managerial tools such as lean management are utterly inadequate to achieve this challenging goal [48].
Several investigations demonstrate that one of the best approaches is to develop CPS and feed IoT-based data streams in computational algorithms [129]. Among

proposed data-driven solutions, tracking technologies gain traction in low standardized warehousing systems due to their ability to increase the visibility of in-plant operations as discussed and quantitatively demonstrated in the previous Chapters. [130]. The RFID technology represents a pivotal enabling sensor with multiple applications in inbound and outbound logistic operations [131]. For instance, [132] automates the development of the warehousing management system by placing passive RFID-based tags in parts and components. A similar approach is to leverage RFID architectures to optimize the storage assignment into storage locations [133]. Although these tangible operational benefits, RFID-based data gathering is highly affected by human commitment and attention, potentially leading to the loss of relevant logistics operations. [132, 134]. In addition, these approaches fail to identify the system behaviour between two consecutive activities (e.g., traveling activities between picking activities).
Based on these limitations, Chapter 1 already pointed out RTLS as the most adequate candidate to indoor locate forklifts and enhance the visibility of in-plant operations along with their performances [48, 54, 55, 56, 57]. Therefore, the challenge of this Chapter is validate the Industrial DB scan capabilities in detecting forklifts operations during the order management. The IoT acquisition layer is designed to monitor logistic activities by leveraging two tags per manual vehicle. This specific sensors' deployment requires a redesign of the unsupervised-based method firstly presented in Chapter 2 and additional tests to validate the CPS in a different indstrial environment. On the one hand, a quantitative benchmark with traditional clustering methods is performed. The proposed algorithm results in the most effective approach to detect uptime forklift operations. On the other hand, a warehousing system proves the operational functioning of the algorithm by returning in a Tracking Management System several KPIs to monitor the efficiency of the order management.

## 4.1 Cyber-physical system for internal logistic systems

This section presents the original contribution of this Chapter. Fig. 4.1 depicts the digital CPS to monitor the efficiency of manual forklifts operations during order management. To achieve this purpose, an IoT acquisition layer acquires strategic information from whichever internal logistic system. While forklifts' indoor positions are acquired from a UWB-based RTLS, process data (e.g., the logistic role of warehouse regions) are retrieved from informative systems. Following a preprocessing step that identifies logistic vehicles trajectories, the Industrial DB scan automatically classifies the in-plant operations of forklifts. These outputs update a Tracking Management System where customized callback functions develop internal logistics KPIs. Benefitting from this activity-driven information, managers monitor the

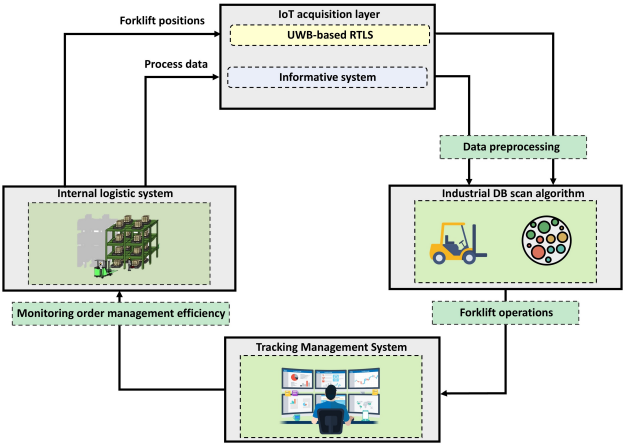


FIGURE 4.1: Qualitative overview of the CPS to monitor the operational efficiency of internal logistic systems

efficiency of internal logistic processes. For instance, the heat maps of uptime operations provide privileged insights into forklift activities over the shift. In addition, the OEE-availability outlines the workload over the shift and as a financial metric may suggest to increase the number of vehicles.

### 4.1.1 IoT acquisition layer

Before going through the steps to mine value within data, it is necessary to describe the required input data by this digital system. As depicted in Fig. 4.1, the proposed digital system is distinguished by two different data streams.
On the one hand, internal logistic system data describe the in-plant functioning of the process under analysis. Meetings with logistics supervisors, process analysis as well as data gathering from informative systems are required to obtain an accurate overview of warehouse operations. For example, the logistics role of warehouse regions is a pivotal insight in investigating manual forklifts' trajectories during orders' fulfillment.
On the other hand, a UWB-based RTLS represents the IoT acquisition layer to gather positioning information of tagged logistic vehicles (Fig. 4.2). The adopted UWB positioning technology is distinguished by a cascade structure, where several subsystems are connected to a single communication line. In particular, subsystems are composed of eight ANs that triangulate the unknown position of moving tags. Similarly to the previous CPS, the proposed system leverages the TDoA method to estimate the 3D time-dependent position of the forklifts [103, 119]. Received messages

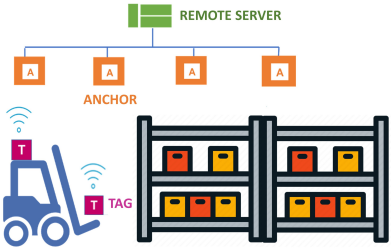


FIGURE 4.2: Conceptual representation of the adopted UWB-based RTLS

are sent to a remote server. As depicted in Fig. 4.2, manual vehicles are equipped with two tags. While the first monitors the cabin movements, the second one acquires the motion patterns of the forks. Regardless of their application, tags are distinguished by variable blink rates ranging from $1Hz$ to $100Hz$ to minimize energy consumption. This dynamic frequency range is driven by onboard accelerometer measurements. During the active mode, these IoT nodes send positioning information to ANs at $10Hz$. However, whether the accelerometer does not register any movement for 5 minutes, the sleep mode is triggered and the refresh rate is decreased to $1Hz$. Therefore, the resulting battery life can last more than one year. It is worth noting that no information is gathered on direct human working activity (e.g., packing a shipping order) and thus fewer privacy concerns may be raised from labor unions in operating warehousing systems [135]. The remote server is the last component of this IoT acquisition layer (see Fig. 4.2). In addition to collecting positioning signals and triangulating the time-dependent positions of forklifts, it preliminary performs a trajectory detection step for any active vehicle and logistic area. Then, the Industrial DB scan is triggered to detect meaningful logistic events during order management (e.g., picking activities). Based on these outputs, a set of KPIs is developed to monitor the efficiency of forklifts in low-standardized internal logistic systems under multiple perspectives.

### 4.1.2 Forklift-centric Industrial DB scan algorithm

Based on the detailed description of positioning data acquired by a UWB-based RTLS, this section quantitatively presents the Industrial DB scan algorithm. This novel density-based ML algorithm classifies manual forklift operations (e.g., picking/depositing activities in storage areas) in internal logistic systems. The proposed algorithm improves the original DB scan formulations under two viewpoints as already discussed in Chapter 2 [26]. To briefly recall to readers' the main novelties, the Industrial DB scan defines additional hyper-parameters and merging criteria to

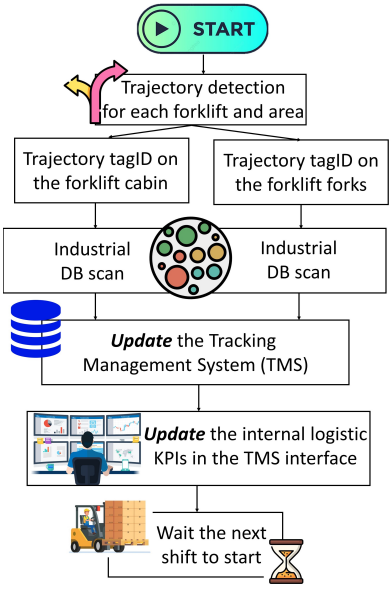


FIGURE 4.3: Qualitative heuristic flow diagram of the proposed Industrial DB scan algorithm for internal logistics processes

model time sensitivity and increase the consistency of process interactions [98, 96]. This features makes the algorithm more robust to positioning outliers driven by ppor line of sight communications between ANs and tags [47, 136]. The Industrial DB scan superior performances in extracting meaningful information from forklift positioning points are quantitatively and discussed in subsection without requiring ground truth labeled data 4.2.2. Contrarly to the previous Chapter, the forklift-centric algorithm formulation is pointed out more in detail due to the peculiar configuration of the IoT acquisition layer and category of manufacturing environment. List of Symbols eases the reading process by listing the indices and parameters of this quantitative discussion.

Starting to analyze the operative functioning of the proposed approach, Fig. 4.3 qualitatively presents the computational steps to mine value within the time dependent positioning information of forklifts. The first algorithm's task targets the trajectory detection for each $l$-th active forklift and $a$-th logistic areas. While logistic areas are defined with managers or downloaded from informative systems, vehicle trajectories are defined as a set of finite and temporally consecutive positioning points within the same $a$-th logistic region. These data streams are processed in the next algorithm steps using nested for loops to ensure that the Industrial DB scan is

triggered in each forklift trajectory. An additional distinction is performed on the $b$-th tag under analysis. Indeed, as depicted in Fig. 4.3 two parallel flow paths are defined to gain insights into the motion patterns of the forklift cabins and forks. It is worth saying that $b$ equal to 1 refers to the tagID placed on the forklift cabin. Although the core functioning and key computations of these two paths are fairly similar, the discussion starts with the left side of the diagram (Fig. 4.3). At this stage, the Industrial DB scan is triggered to classify logistic events based on the motion patterns of forklift cabins (see Algorithm 1).

Each $i$-th cabin trajectory $t_{i,b}^{l,a}$ (e.g., $b = 1$) groups a variable number of frame-dependent and temporally consecutives positioning points $p_{i,f,b}^{l,a}$ (where $f = f', ..., f^*$). In detail any $p_{i,f,b}^{l,a} = (px_{i,f,b}^{l,a}, py_{i,f,b}^{l,a}, ts_{i,f,b}^{l,a})$, where the last parameter represent the corresponding timestamp of the $f$-th frame. For each $t_{i,1}^{l,a}$, the algorithm defines as $\epsilon$ sequences as the number of positioning points in the trajectory. To do so, the pairwise Euclidean Distance is performed between all positioning points. These geometric points are added to lists whether they are spaced at the greatest of $d^*$ between each other (see lines from 6 to 8 in Algorithm 1 ). This first hyper-parameter represents a threshold value in meters to be set concerning the final application and the measured noise of the adopted RTLS. Based on this, a preliminary clustering of $t_{i,b}^{l,a}$ positioning points is achieved. However, potentially grouped data streams in neighbor lists are not subjected to time-driven constraints. This point is addressed by Algorithm 1 in the lines ranging from 10 to 15, where two additional hyperparameters are presented, namely $\delta$t and $NPts$. While $\delta$t checks whether points grouped in the neighbor lists are temporally consecutive, the second hyper-parameter defines the lowest duration of the list. In detail, $\delta$t represents the average sampling rate of the IoT acquisition layer (see subsection 4.1.1), and $NPts$ needs to be set in agreement with plant supervisors based on the expected minimum duration of forklift operations. Based on $\delta$t and $NPts$, $\epsilon$ sequences may be classified as forklift operations (e.g., $C_{z,i,b}^{l,a}$, where $b = 1$ since the focus here is ensured on the tag placed on the cabin). Trivially, the index $z$ orders the classified forklift process interactions or operation from 1 to $Z$.

Although the automatically detected $C_{z,i,b}^{l,a}$ are temporally consistent, these forklift operations may be affected by the uncertainty of manual vehicle trajectories and the acquisition noise of the adopted UWB-based RTLS [135, 47]. To increase the reliability of these logistic events, the if statement in line 19 of the Algorithm 1 defines merging criteria for temporally consecutive operations (e.g., $C_{z,i,b}^{l,a}$ and $C_{z+1,i,b}^{l,a}$). The first criterion analyzes the delta time between $C_{z,i,b}^{l,a}$ and $C_{z+1,i,b}^{l,a}$. In particular, $ts_{i,f',b,z}^{l,a}$ and $ts_{i,f^*,b,z}^{l,a}$ define the starting and ending timestamps of forklift operations based on the clustered positioning points. The temporal difference between $ts_{i,f^*,b,z}^{l,a}$ and $ts_{i,f',b,z+1}^{l,a}$ has to be at longest equal to $\alpha$. This hyper-parameter should be set with logistic supervisors based on the expected average time between two conceptually

different forklift events. The second criterion checks the Euclidean Distance between the geometric centers of consecutive logistic operations (e.g. $O^{l,a}_{i,b,z}$ and $O^{l,a}_{i,b,z}$ ). In particular, $O^{l,a}_{i,b,z} = \{Ox^{l,a}_{i,b,z}, Oy^{l,a}_{i,b,z}\}$ is computed through the weighted average between positioning points grouped in $C^{l,a}_{z,i,b}$ (e.g., $px^{l,a}_{i,f',b}$) and their respective timestamps (e.g., $ts^{l,a}_{i,f',b}$)) (Eq. 4.1).

$$Ox^{l,a}_{z,i,b} = \frac{\sum_{f=f'}^{f^*-1} px^{l,a}_{i,f',z} \left( ts^{l,a}_{i,f'+1,z} - ts^{l,a}_{i,f',z} \right)}{\sum_{f=f'}^{f^*-1} \left( ts^{l,a}_{i,f'+1,z} - ts^{l,a}_{i,f',z} \right)} \tag{4.1}$$

The same approach is adopted to calculate the $y$ dimension of the geometrical center. Therefore, the Industrial DB scan verifies if the Euclidean distance between $O^{l,a}_{z,i,b}$ and $O^{l,a}_{z+1,i,b}$ (e.g., $dist(O^{l,a}_{z,i,b}, O^{l,a}_{z+1,i,b})$ in line 19 of Algorithm 1) is lower than $\gamma$ as threshold in meters. This hyperparameter is strictly related to the design of the monitored logistic environment since it represents the expected average distance between consecutive warehouse operations.
Based on the characteristics of the logistic process under analysis, the $C^{l,a}_{z,i,b}$ can be related to process-driven activities such as P/D and packaging. In addition, the defined hyper-parameter namely $NPts$, $\epsilon$, $\alpha$ and $\gamma$ may be indexed to $a$. Although the detected forklift operations provide valuable insights into internal logistic systems functioning, the motion patterns of forks are completely neglected. For this purpose, the heuristic flow diagram in Fig. 4.3 depicts the parallel computation of data coming from the second tagID placed on the forks (e.g., $b = 2$). The operative functioning of the Industrial DB scan is equal to the one described in the last paragraph and by the Algorithm 1. Contrarly to before, the outputs of these streams of computations return the mean $3D$ positions of the forks. Such a level of detail is particularly useful in storage areas where manual vehicles perform P/D operations. It is worth noting that the hyper-parameters (e.g., $NPts$, $d^*$, $\alpha$ and $\gamma$) may be additionally indexed to the tagID.
Finally, the detected forklift operations combined with the respective mean $3D$ positions of the forks are stored in a Tracking Management System where specific callback functions define strategic internal logistic KPIs to monitor the efficiency of forklifts in low standardized logistic systems.

**Algorithm 1** Industrial DB scan

**Require:** Forklift trajectory in a logistic region $t^{l,a}_{i,b}$, radius $d^*$, minimum points per forklift operation $NPts$

**Ensure:** Current forklift operation result $C^{l,a}_{z,i,b}$

Initialize $C^{l,a}_{z,i,b}$ as an empty list
$z = 1$
**for** each positioning point $\mathbf{p}$ in $t^{l,a}_{i,b}$ **do**
    **for** each positioning point $\mathbf{p}'$ in $T^{f,r}$ **do**
        Compute the Euclidean distance $dist(\mathbf{p}, \mathbf{p}')$
        **if** $dist(\mathbf{p}, \mathbf{p}') \leq \epsilon$ **then**
            Add $\mathbf{p}'$ to the $\epsilon$ sequence of $\mathbf{p}$
        **end if**
    **end for**
    **if** the size of the $\epsilon$ sequence of $\mathbf{p} > NPts$ **and** positioning points are spaced by $\delta$t **then**
        Add $p$ and its temporal consecutive neighbors to $C^{l,a}_{z,i,b}$
        $z = z + 1$
    **else**
        Define $\mathbf{p}$ as noise
    **end if**
**end for**
$z = 1$
**while** $z \leq Z$ **do**
    **if** $ts^{l,a}_{i,f^*,b,z} - ts^{l,a}_{i,f',b,z+1} \leq \alpha$ **and** $dist(O^{l,a}_{z,i,b}, O^{l,a}_{z+1,i,b}) < \gamma$ **then**
        **Merge** $C^{l,a}_{z,i,b}$ and $C^{l,a}_{z+1,i,b}$
        **Update** $C^{l,a}_{z,i,b}$
    **end if**
    $z = z + 1$
**end while**
**return** $C^{l,a}_{z,i,b}, \forall z = 1, ..., Z$

### 4.1.3 Tracking Management System

The classified forklift activities flow in the Tracking Management System. This information provides quantitative insights for plant supervisors to evaluate the functioning and efficiency of whichever RTLS-based logistic system. Tab. 4.1 shows the data structure of detected and thus stored forklift operations.

TABLE 4.1: Example of the tracking management system on an active manual forklift

| Start | End | Duration [sec] | Operation | Distance [m] | X-axis [m] | Y-axis [m] | Z-axis [m] |
|---|---|---|---|---|---|---|---|
| 12:09:08.71 | 12:09:17.44 | 8.73 | P/D - Storage A | 0.00 | 31.14 | 4.96 | 9.66 |
| 12:09:17.45 | 12:09:30.58 | 13.13 | Travel | 16.80 | – | – | – |
| 10:06:26.47 | 10:06:46.09 | 10.00 | Packaging | 0.00 | 20.50 | 7.89 | 2.23 |
| ... | ... | ... | ... | ... | ... | ... | ... |
| 15:04:55.64 | 15:09:08.71 | 253.06 | Parking | 0.00 | 40.89 | 34.60 | 0.31 |

In particular, the informative content of the first five columns is derived by leveraging the Industrial DB scan on the trajectories assumed by the tagID placed on the forklift's cabin (see the left path in Fig. 4.3). Trivially, the distance column is distinguished by values greater than zero whenever the density-based algorithm detects a traveling activity. The last three columns in Tab. 4.1 provide strategic insights about the motion patterns of the second tagID placed on the forks. For instance, let's consider the picking/depositing (P/D in Tab. 4.1 to limit space) operation that occurred in the storage area A of an analyzed internal logistic system (e.g., first row in Tab. 4.1). This information provides the mean forks 3D positions clustered by the Industrial DB scan during the P/D activity. Such valuable insight is obtained by the right path of the algorithm in Fig.4.3.
Starting from these classified operations, customized callback functions develop internal logistic KPIs to monitor the performances of manual forklift activities. The following bullet point lists the automatically updated efficiency metrics taken into account:

- **Timeline of forklifts**
- **Heat map of forklifts uptime operations in logistic areas**
- **Picking/deposit operations in storage areas**
- **OEE-availability of forklifts**

These statistics are hardly achievable without RTLS-based data streams and contribute to improving the visibility and traceability of low-standardized logistic systems. While the timeline of forklifts points out the time horizon where forklifts are in motion, the heat map highlights the distribution of uptime activities during working shifts. Benefitting from this second insight, logistic managers may easily identify the most utilized vehicles to perform order management operations. Supposing higher shipping times compared to historical data, supervisors can discuss with employees to achieve a better understanding of potential bottlenecks. The investigation of in-plant performances is narrowed to P/D operations. In addition to detecting their forklift-based amount over the shift, traveling times among consecutive operations are pointed out. This valuable insight highlights both the learning curve of employees in locating goods and the efficiency of product displacement by

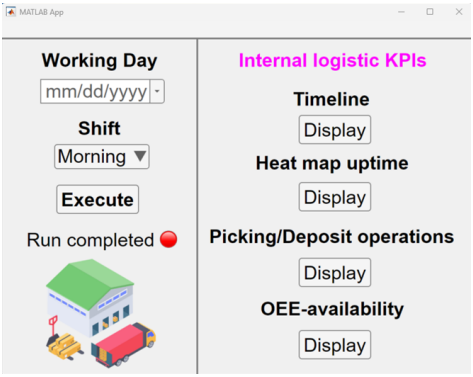


FIGURE 4.4: Tracking management system interface

the management. To ease the identification process of uptime events, logistic supervisors can plot spaghetti charts and even the single activity of forklifts. Finally, these insights on uptime activities are leveraged to assess the OEE-availability of manual vehicles. This KPI can support the economic initiative of expanding the fleet as well.
To achieve a user-friendly performance monitoring of forklift operations, Fig. 4.4 depicts the Tracking Management System interface that mirrors the proposed and discussed KPIs in a digital environment.

## 4.2 Cyber-physical system validation

Based on the conceptualized ML and IoT-based CPS, this section validates its applicability in a European warehouse under distinctive perspectives. First, subsection 4.2.1 describes the functioning of the monitored low-standardized logistic system. Second, the Industrial DB scan classification performances are benchmarked with other density-based formulations (see subsection 4.2.2). Third, subsection 4.3 discusses the managerial implication of monitoring a logistic working shift using the proposed KPIs.

### 4.2.1 Case study

The developed RTLS-based acquisition layer (section 4.1) is successfully tested and validated in a European warehouse that inbounds and outbounds automotive parts and components using manual forklifts. Fig. 4.5 depicts the 8000 $m^2$ plan area of the warehousing systems divided into 9 specific sub-areas based on their logistic role during order management.

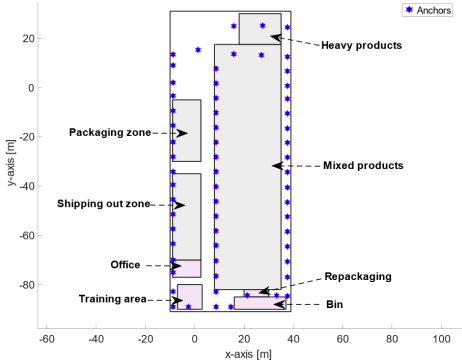


FIGURE 4.5: Referenced warehouse system layout by the UWB-based RTLS

These areas are grouped into two different categories. On the one hand, the process-driven ones that host uptime operations are grey-colored. While the Mixed and Heavy product zones represent storage areas, the other two complete the order management involving orders' packaging and shipping out activities. In detail, both storage areas are rack-based with a maximum height equal to $9.05m$ and a distance between levels ranging from $0.58m$ to $1.28m$. Also, the shipping-out area is rack-based to optimize space during high-demand periods. On the other hand, the remaining pink zones, namely the office, training area, repacking, and bin, are not relevant to the process and thus are not considered further in the analysis. The remaining white spaces represent the corridors.

To better address the seasonality effect, logistic supervisors recognize that process experience and conventional approaches such as lean management were not sufficient to monitor the dynamic performances of forklifts. Therefore, the company required to enhance the visibility of forklifts by automatically detecting their uptime activities using the digital system presented in section 4.1. A UWB-based RTLS is installed in the warehouse implementing a network of 63 ANs. These receivers are placed at a height between $6.43m$ and $10.30m$. Manual forklifts are equipped with two tags to dynamically acquire the positioning information of the cabin and the forks (subsection 4.1.1). It is worth saying that tags are distinguished by unique IDs. For example, the FL01 forklift is equipped with tagIDs 4968 and 5294 on the cabin and the fork, respectively. The resulting accuracy of the presented IoT system is equal on average to $0.5m$. Time-dependent positioning data are stored on an encrypted company server, accessible via WebSockets.

Exploiting the description of the presented warehousing logistic system, the following two subsections validate the digital system from different points of view. While

subsection 4.2.2 justifies the definition of a novel density-based clustering algorithm based on several metrics, the second one presents developed KPIs along with the managerial implications.

### 4.2.2 Comparison of density-based clustering algorithms

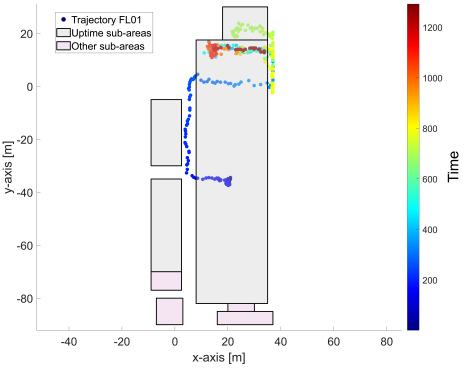


(A) FL01 trajectory

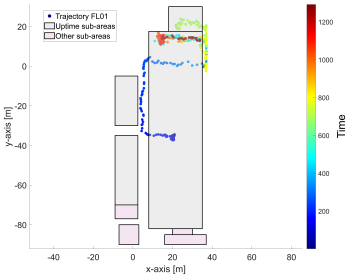


(B) Uptime activities returned by the DB scan

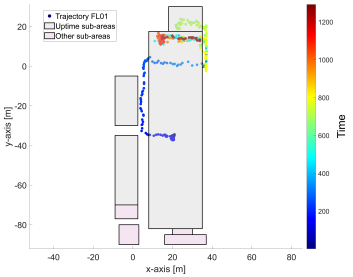


(C) Uptime activities returned by the Industrial DB scan

FIGURE 4.6: Comparison of the analyzed density-based algorithms

This subsection validates the Industrial DB scan by proving its superior detection performance compared to other density-based formulations. In particular, a preliminary investigation analyzes both graphically and quantitatively the weaknesses of the original DB scan formulation, then three clustering metrics validate the proposed clustering approach using as input data a working shift lasting 8 hours.
Starting the discussion, Fig.4.6 (a) shows time-dependent trajectories of the FL01

forklift, which occurred from 07:52:51 to 08:03:00 on $19^{th}$ of December 2022. After the high-spatial density of blue points, the manual vehicle starts a travel activity toward the upper part of the Mixed Products area. However, due to the intrinsic uncertainty of human behavior, FL01 returns around the same sets of indoor locations (see the light red cloud of points in Fig.4.6 (a)). In particular, a similar set of indoor positions is assumed with a time difference approximately equal to 41 seconds. For such scenarios, the application of the DB scan leads to an unrepresentative identification of forklift operations. Fig. 4.6 (b) accurately depicts the time insensitivity of this density-based clustering algorithm. It is worth noting that the uptime activity #2 groups indoor positions belonging to different time windows. On the contrary, the Industrial DB scan correctly addresses such strong limitation by leveraging the time-driven constraints (see subsection 4.1.2). Therefore, an additional uptime operation is detected as shown in Fig. 4.6 (c). While uptime activity #2 clusters indoor positions from 07:58:20 to 08:00:07, the third occurs from 08:01:22 to 08:02:55.
Although these trajectories provide a representative example of the major weaknesses of the traditional DB scan formulation, a more extensive comparison of these density-based methods is required. Hence, two DB scan algorithms are benchmarked to the proposed ML-based clustering method. While the first is the original DB scan formulation, the second one addresses the well-known time weaknesses. In the following this mathematical method is renamed DB scan time-sensitive. It is worth noting that this benchmarking process is performed using the same values of hyper-parameters. $d*$ is equal to 0.5 meters and the minimum duration of a logistic operation (e.g., $NPts$) and $\delta$t are equal to 15 seconds and 10 Hz, respectively. In addition, the motion uncertainty and RTLS acquisition noise hyper-parameters (e.g.,$\alpha$ and $\gamma$) account for 20 seconds and 0.7 meters. The resulting comparison is performed using the number of detected uptime operations and three widely adopted performance metrics for unsupervised problems with unlabeled data [137, 138]. First, the Silhouette Coefficient (SIC) indicates how well logistics operations are clearly distinguished. The value ranges from $-1$ to 1 by taking into account both the average distances between each positioning point within uptime operations and among all operations [139]. Second, the variance of detected activities is measured through the Calinski-Harabasz Index (CHI). This metric measures the ratio of dispersion between uptime operations with the dispersion inter-operations. the dispersion is computed as the sum of squared distances among forklift positioning data [140]. Third, the Davies-Bouldin Index (DBI) evaluates the ratio of the average dissimilarity within a logistic event to the maximum average dissimilarity between events. The returned value represents the worst-case scenario among all logistic operations [138]. Based on this, Tab. 4.2 summarizes the scores of these metrics having as input the indoor positions of five active forklifts during the morning shift on $19^{th}$ of December 2022, lasting 8 hours. The first two formulations of the DB scan have the lowest and highest number of detected uptime operations, respectively. These

values are driven by the time weakness of the original DB scan formulation and the absence of RTLS-based merging criteria for the time-sensitive formulation. Addressing these limitations, the Industrial DB scan returns 1012 uptime operations. However, the detected forklift activities are not sufficient to adequately benchmark the analyzed density-based algorithms. Thus, the last three columns in Tab. 4.2 complete the analysis proving the superior performances of the Industrial DB scan. In particular, the SIC equal to 0.38 indicates better separation and cohesion in clustering forklift operations. The same is valid for the CHI, where the Industrial DB scan is distinguished by a value equal to 99534.53.

TABLE 4.2: Comparison of density-based clustering algorithms

| Algorithm | Uptime operations | SIC | CHI | DBI |
|---|---|---|---|---|
| DB scan | 885 | 0.31 | 92943.22 | 1.70 |
| DB scan time-sensitive | 2826 | 0.35 | 55231.17 | 3.84 |
| **Industrial DB scan** | **1012** | **0.38** | **99534.53** | **5.32** |

This index proves better dispersions between and within uptime operations. The benchmarking ends with the DBI. Although lower values underline better performances, the area of application of these density-based methods requires a different evaluation perspective. Indeed, the increasing DBI values highlight the capabilities of separating operations occurred in the same area but in different time windows.

## 4.3 Results & managerial insights

Following the investigation into clustering performances, this subsection further validates the proposed CPS. The discussion is focused on the morning shift on the $19^{th}$ of December 2022. In particular, the monitored shift starts at 5:50 am lasting 8 hours. The automatically detected forklift operations are stored in a Tracking Management System where callback functions develop strategic KPIs to monitor the efficiency of this internal logistic process. Based on this, the next paragraph discusses the managerial implications carried by this UWB-based layer.
The logistic process monitoring starts with the timeline of active forklifts during the working shift (Fig. 4.7). While pink bars depict the active time of forklifts, white regions suggest the appearance of downtime activities driven by the sleep feature of tags (see subsection 4.1.1). The vast majority of forklifts (e.g., from FL01 to FL04) are distinguished by active times roughly equal to 7 hours. On the contrary, FL05 is used for no more than 2 hours during the working shift (Fig. 4.7). However, these time windows are not necessarily related to the system's under-performances because forklift drivers perform several off-board activities (e.g., manual material handling) during the order management process. In particular, the under-utilized

vehicle (e.g., FL05) is used by a qualified jolly operator shared with the production department during high-demand periods.

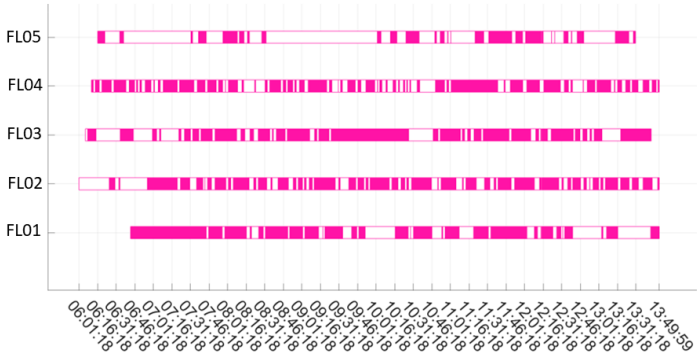


FIGURE 4.7: Timeline of monitored forklifts during the monitored morning shift

Although this level of detail indicates the most used vehicles over the shifts, it fails to automatically detect the duration of uptime operations and their region of occurrence. This two-fold analysis is enabled by the second interactive button in the Tracking Management System interface (Fig. 4.4). First, Fig. 4.8 introduces the heat map of valued added operations in the time domain, where each cell stores the aggregated duration of forklift-driven activities in logistic areas. This KPI enhances the visibility into forklift operations over working shifts. On the one hand, the proposed heat map underlines the most contributing forklift in performing logistic operations. For instance, FL01 is solely involved in picking/depositing operations, spending 119.6 minutes and 23.18 minutes in the Mixed and Heavy Products areas, respectively. In addition, 3 over 5 forklifts (e.g., FL01, FL02, and FL04) spend around 2 hours performing picking/depositing activities in the Mixed Products zone. The third vehicle registers a considerable time duration in performing packaging operations (e.g., almost half an hour). At the same time, no shipping out activities are detected during this morning shift. Therefore, forklifts are exploited to store and when necessary package manufactured components and parts from the production department. On the other hand, shift-driven information can be compared to historical data to detect unexpected deviations from average duration values. In this regard, meetings with the related forklift drivers may be encouraged to discuss potential process weaknesses. This analysis is complemented by highlighting the spatial dimension of forklift activities. Therefore, Fig. 4.9 depicts the detected operations within the logistic system regions. To not burden the presented figure, the colored forklift operations returned by the Industrial DB scan are displayed as

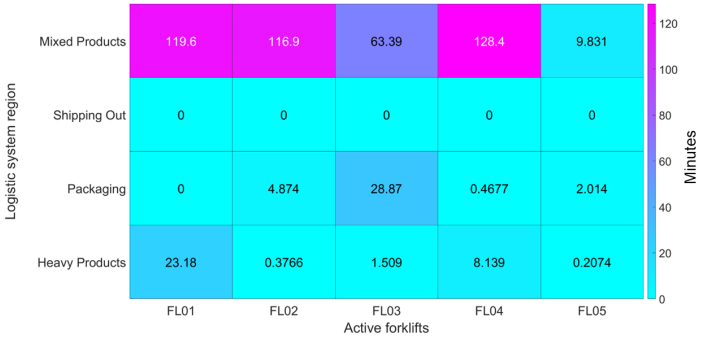


FIGURE 4.8: Aggregated uptime operations in logistic areas

points in the Euclidean space. This second level of analysis provides straightforward insights into the most visited regions of the warehousing system. For instance, the bottom part of the Mixed Products areas is hardly visited compared to the upper one confirming one of the best practices of the analyzed case study. Indeed, logistic supervisors recommend forklift drivers to achieve high occupation levels in the upper area of Mixed Products. This decision is driven by the reduced distances between the production department and the packaging area. It is worth noting that based on supervisor experience more than the 95% of manufactured components and final orders are packaged before being stored and shipped, respectively. Considering the relevance of P/D activities both in the time and frequency domain (see Fig. 4.8 and 4.9), it is extremely relevant to compare the time spent in storage areas with the duration of the mentioned logistic event, where the first includes travel activities as well. In particular, times spent in storage areas are always greater than the related uptime activities than a multiplication factor ranging from 25.3% to 46.7%. The worst-case scenario emerges with the first forklift (e.g., FL01) that visited storage areas for more than 200 minutes over the shift. This insight further enhances the visibility of logistic operations while offering a unique opportunity to logistic supervisors to improve in-plant operations. For instance, the scheduling optimization of P/D activities and optimal material allocation may be investigated using heuristic-based approaches.

At the same time, better training of forklift drivers could reduce unnecessary traveling routes during order management. Regardless of the means, the overall objective needs to narrow down the previously discussed multiplication factors between time spent in storage areas and the related uptime activities. In addition to improving forklift performances, a consistent benefit is to reduce the charging hours of vehicles leading to energy cost savings but most importantly to a reduced carbon footprint.

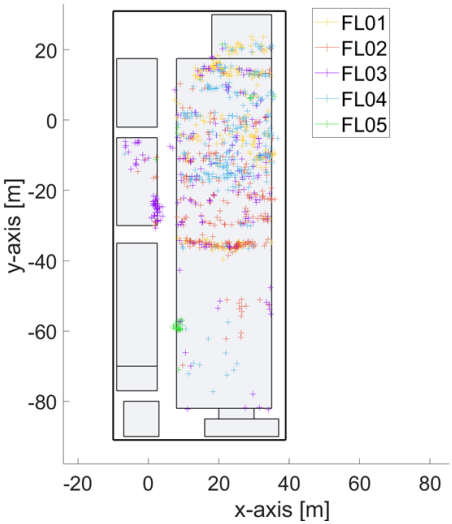


FIGURE 4.9: Detected forklift uptime operations by the Industrial DB scan

This insight proves the CPS capabilities in contributing to design environmentally sustainable warehousing systems.
An additional perspective on P/D operations is given by their forklift-centric frequency over the shift. As depicted by Fig. 4.10, FL01, FL02, and FL04 register the highest statistics accounting for 247, 245, and 268, respectively. In addition, as expected by analyzing the duration of uptime operations (Fig. 4.8), more than 90% of P/D occur in the Mixed Products warehouse region. Similarly to before, more insightful managerial implications are derived by combining this KPI with the duration of uptime activities in storage areas (see Fig.4.8). In particular, FLO1 and FL05 account for the highest and lowest statistic equal to 34.64 and 19.43 seconds per operation, respectively. Taking into account all forklifts, this metric registers 27.76 seconds per operation. This comparison of mean values can be performed among the two storage areas as well. While the averages for FL03, FL04, and FL05 differ solely of 7 seconds at greatest, FL01 offers a striking comparison. The average times account for 32.47 and 53.49 seconds in the Mixed and Heavy Product regions, respectively. These statistics may be related to the intrinsic nature of the products stored requiring slower material handling processes. Overall, average P/D values are valuable information for two different aspects. First, gamification approaches may be implemented to award the best-performing employee on a weekly or monthly basis. To avoid privacy-related concerns, target average picking

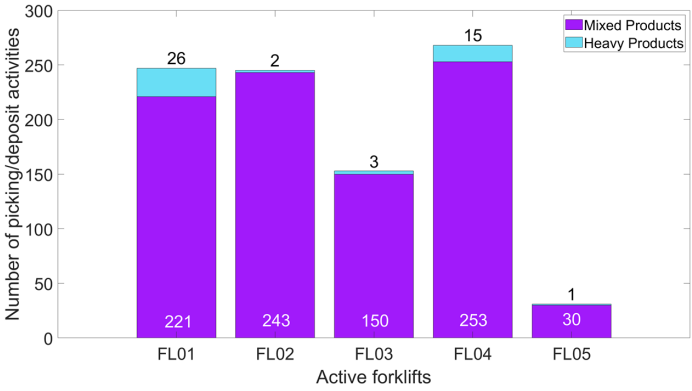


FIGURE 4.10: Amount of P/D operations in different storage areas

values might be set for the entire fleet of vehicles. Second, comparison with historical values effectively detect shift and process-related weaknesses while promoting discussion with employees.

The last KPI integrates the previous information to evaluate the duration of uptime operations and OEE-availability. Fig. 4.11 depicts these two forklift-specific metrics that underline pretty low statistics. While uptime operations never exceed 3 hours, FL01 registers the highest availability equal to 29.76 %. This value is given by dividing the duration of uptime operations to the length of the shift (e.g., 8 hours). These pretty low statistics do not imply system underperformance because human drivers perform several process-driven operations off-board from manual vehicles. Overall, the OEE-availability enhances the monitoring of low standardized logistic environments from two different viewpoints. First, it underlines the saturation of vehicles. In particular, logistic supervisors may combine historical data by taking into account orders' number with OEE-availability to decide the optimal number of forklifts to allocate in each shift.
To conclude, the developed digital immune system demonstrates that RTLS combined with ML-based algorithms can effectively support the monitoring of low-standardized logistics systems. This finding is consistent with the predictions outlined in the Gartner Top Strategic Technology Trends report for 2023 ([141]). Indeed, the Industrial DB scan enhances the visibility of in-plant functioning of logistic environments by extracting uptime activities from forklift trajectories. Based on the analyzed working shift, the detected uptime forklift operations highlight notable time spent in storage areas to perform picking/depositing operations. Three over five vehicles carry out more than 240 picking/depositing operations for more than 2 hours each. However, the OEE-availability never exceeds 30%. The analysis of the

multidimensional KPIs, hardly achievable without this IoT-based digital system, may consolidate the process performances of logistic companies.

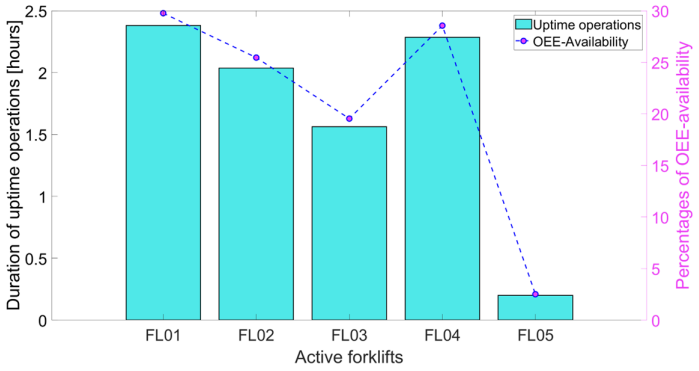


FIGURE 4.11: OEE-availability of the monitored forklifts

## Chapter 5

# Digital European Assembly Worksheet assessment

"Don't you know
They are talking about a revolution?
It sounds like a whisper"
– *Tracy Chapman, Talkin' Bout a Revolution*, 1988

The European manufacturing industries are one of the most labor-intensive sectors, employing over 32.1 million workers in 2022 [142]. However, these human-centrinc working environments have faced various disruptions in recent years, ranging from social to market threats [2]. On the one hand, European population pyramids offer a grim scenario highlighting a notable aging process. Eurostat projections forecast that individuals aged 55 years or older will peak at 40.6% of the European population by 2050, up from 33.6% in 2019 [143]. This phenomenon combined with greater life expectancies is driving European economies to increase the retirement age. Simultaneously, high turnover rates in jobs contribute to increased manufacturing costs related to operator training and replacement [144]; this rate for trade workers reached 7.8% in 2021 [145]. Occupational injuries point out a compelling scenario as well. [145] estimates that more than 10% of the European workforce is affected by work-related health problems where a compelling physical risk targets material handling of loads and repetitive arm movements. Also, the manufacturing sector is the greatest contributor to accident fillings. On the other hand, as already discussed in the previous Chapters, customer preferences are steering smart factories toward

offering high production flexibility with shorter product life cycles [26, 27, 146]. This grim scenario is partially addressed by digital and data-driven approaches to mitigate the share of WMSD. However, as already discussed in Chapter 1, digital ergonomic investigations fall short in digitizing the EAWS. Therefore, the ambitious goal of this Chapter is to design an EAWS-informed CPS to comprehensively safeguard the physical resilience of workers during task executions. For this purpose, a human-centric IoT acquisition layer feeds HPIs, body joint positions and exerted forces into computational algorithms to analyze process safety weaknesses from multiple perspectives. The EAWS based KRIs are embedded in an Ergonomic DSS to enable data-oriented decision-making processes.

## 5.1 EAWS-informed cyber-physical system

This section details the developed digital architecture designed to enhance the physical resilience of Operators 5.0 in human-centric manufacturing systems (refer to Figure 5.1).

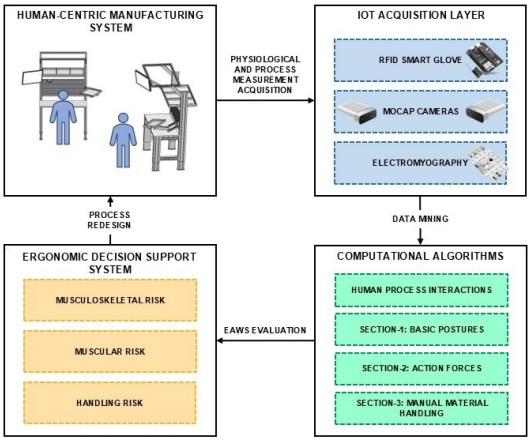


FIGURE 5.1: Overview of the CPS for evaluating the EAWS.

The IoT acquisition layer integrates three enabling technologies to automatically evaluate the Basic Postures, Action Forces, and Manual Material Handling sections of the EAWS screening tool. The RFID technology detects HPIs, while MOCAP cameras and sEMG wearables capture time-driven body joint positions and muscular contractions, respectively. Computational algorithms process these diverse data streams to perform task-driven assessments of the aforementioned EAWS sections. Consequently, an ergonomic DSS presents multidimensional KRIs to identify

operator and process-specific safety weaknesses. For instance, the Musculoskeletal Risk metric, in addition to assigning a global risk score for any manufacturing task, displays the time-dependent body angles for each human posture. This granular level of detail proves invaluable for industrial plant supervisors in initiating process modifications, such as assembly line re-balancing.

### 5.1.1 IoT acquisition layer

Three enabling IoT technologies collect process, physiological, and motion measurements: (i) the RFID smart glove, (ii) the sEMG data acquisition system, and (iii) the MOCAP camera network.
The RFID-based glove identifies HPIs by reading passive tags attached to tools and fasteners. The Radio Frequency reader uses the battery-powered PyScan device [147], which integrates the NXP MFRC63002 RFID transceiver and connects wirelessly to a server via Wi-Fi. The device sends the ID of each scanned RFID tag to the server using the MQTT protocol. On the server, the timestamp associated with the detection moment for each tag is recorded along with its ID and stored in an InfluxDB database.
The sEMG data acquisition system uses the BITalino evaluation kit [148], which incorporates the Atmega 328P microcontroller, the HC-6 Bluetooth transceiver, and the AD8232 instrumentation amplifier. For each sEMG channel, the AD8232 amplifies the provided signal; the signal is acquired by the 10-bit Successive Approximation Register Analog-to-Digital Converter (ADC) embedded in the microcontroller. The data acquisition board exhibits a Signal-to-Noise Ratio (SNR) of 55.72 dB, delivers an Effective Number Of Bits of 8.73 bits, and operates at a sampling rate of 1 kHz [148]. Acquired samples are streamed in real-time via Bluetooth to a gateway and transmitted to the server via Wi-Fi. On the server, each sEMG sample is stored with its acquisition timestamp. The monitored muscles include both the left and right biceps and forearms [149]. The MOCAP system consists of two Microsoft Azure Kinect devices [150] to mitigate acquisition errors in occlusion scenarios [34]. These devices are synchronized with each other using an audio cable. Each device embeds a 1-MP (MegaPixel) depth sensor with a variable field-of-view and a 12-MP RGB (Red, Green, Blue) video camera, operating at a frame rate of 15 fps. The MOCAP network is positioned in the manufacturing layout, synchronized through an absolute clock, and calibrated via a checkerboard pattern. Cameras are placed to maximize the coverage area and minimize potential sources of obstructions. Recordings from each device are processed frame by frame in a loop for identified bodies, to which specific IDs are assigned. Calculations for determining body joint positions start at the pelvis and extend to the ears, ensuring interrelationships using a global approach. The resulting 3D coordinates of body joints, along with associated confidence levels, are saved in separate output files, while timestamps are stored for each data stream.

TABLE 5.1: Role of enabling IoT technologies in digitizing the EAWS index.

| EAWS Section | RFID | MOCAP | sEMG |
|---|---|---|---|
| Basic Postures | ✔ | ✔ | ✘ |
| Action Forces | ✔ | ✘ | ✔ |
| MMH | ✔ | ✔ | ✔ |

The following computational algorithms detail how to fuse the video-based distributed measurements to obtain a reference worker representation (see section 5.1.2). The recorded parameters, such as sEMG signals and body joint coordinates, undergo synchronization during the post-processing stage within the computational steps of HPIs (refer to section 5.1.2). Following this synchronization, the EAWS index is digitally reconstructed by integrating physiological and process-related measurements (see Table 5.1).

### 5.1.2 Computational algorithms

Based on the discussed IoT technologies, this section outlines the computational algorithms for extracting value from the acquired data streams and digitizing the EAWS-driven sections. Despite the synchronous acquisition of physiological and process data, an initial computation utilizes RFID-based measurements to segment workers' activities and recognize tool usage (refer to Subection 5.1.2). For each assembly task, a parallel set of computations is initiated to evaluate three sections of the EAWS: Basic Postures (section 5.1.2), Action Forces (section 5.1.2), and MMH (section 5.1.2). While the first two assessments consider the MOCAP and sEMG data streams independently, the third section integrates the three IoT technologies to compute the KRIs for this ergonomic dimension (refer to Table 5.1). Finally, two Appendices ease the reading process of this methodology. While the List of Symbols summarizes the indices and parameters, Appendix B lists the body joints used to evaluate EAWS postures.

#### Process interactions

This pre-processing step utilizes RFID-based data streams to identify HPIs and synchronize measurements from the other IoT technologies. Specifically, data are downloaded from a server through a SSH connection and divided into task- and tool-driven measurements.

Although the computational steps for mining value from data streams are fairly similar, the discussion starts with task recognition (see Algorithm 2). For assembly activities, time windows are reconstructed based on successive pickings of components, fasteners, or Work-In-Progress (WIP) products. This process depends highly

on the manufacturing workflow and requires consideration of metadata. Therefore, it is crucial to deploy passive tags in strategic locations within the manufacturing system (e.g., supermarket trays). The RFID-based glove continuously reads passive tags' unique strings and associates the corresponding timestamps. $AS_f$ and $AT_f$ represent these parameters during the $f$-th recording frame. $AT_f$ and $AT_{f+1}$ are temporally spaced by $\delta$t, the sampling rate of the RFID-based glove. It is reasonable to gather the same $AS$ multiple times for consecutive frames whenever workers pick components from the activity-related bin. Based on these raw data, Algorithm 2 exploits two while loops to create a scan list for each $r$-th activity of the assembly sequence (e.g., $Scan_r$).

**Algorithm 2** Time-series algorithm to detect activity-oriented HPIs

**Require:** $AT_f$ and $AS_f$ $\forall f = 1, ..., F$

1: Initialize $T_r$ and $S_r$ as empty parameters
2: $f = 1$
3: $r = 0$
4: **while** $f \leq F$ **do**
5: $\quad r = r + 1$
6: $\quad$ **while** $(AT_{f+1} - AT_f \leq \delta)$ **and** $(AS_{f+1} = AS_f)$ **do**
7: $\quad\quad$ **Add** $AT_{f+1}$ to the list $Scan_r$
8: $\quad\quad f = f + 1$
9: $\quad$ **end while**
10: $\quad T_r = min(Scan_r)$
11: $\quad S_r = AS_f$
12: **end while**
13: **return** $T_r$ and $S_r$, $\forall r = 1, ..., R$

In particular, $AT_{f+1}$ values are continuously added to $Scan_r$ if their temporal difference with the current timeframe is at most equal to $\delta$t. To avoid mixing assembly activities, an additional check ensures that $AS_{f+1}$ and $AS_f$ agree (see while statement in line 6). Once the algorithm exits the inner while loop, it computes the starting time of the $r$-th activity and associates the respective tag string (see lines 10 and 11). It is worth noting that $T_{r+1}$ represents both the starting and ending time for the $(r+1)$-th and $r$-th assembly activities, respectively. Therefore, the duration of the $a$-th assembly activity is given by the difference between $T_{r+1}$ and $T_r$.
The automatic detection of tool usage follows similar computational steps to those discussed in Algorithm 2. Assuming each tool is embedded with a passive tag, $TS_{f'}$

and $TT_{f'}$ represent the unique tool strings and the associated timestamps, respectively. These time-driven parameters are processed by the same two while loops. However, these HPIs derive different parameters from $Scan_t$ when the algorithm breaks the inner loop. Each $t$-th tool usage is distinguished by a starting time (i.e., $TTstart_t$), end time (i.e., $TTend_t$), and tool string (i.e., $S_t$). While $TTstart_t$ and $TTend_t$ are equal to the earliest and latest $TT_{f'}$ values belonging to $Scan_t$, $S_t$ corresponds to the tag string currently processed by the inner loop (i.e., $TS_{f'}$). To increase the consistency of the detected tool-driven HPIs, two additional hyperparameters can be introduced to mitigate the intrinsic uncertainty of human factors. First, tool usages with durations shorter than $\lambda$ can be discarded. Second, consecutive tool-driven HPIs are merged if the following condition is met.

$$TTstart_{t+1} - TTend_t \leq \tau; \text{ where } S_t = S_{t+1} \tag{5.1}$$

Benefiting from the evaluated activity- and tool-oriented HPIs, a parallel stream of computations is triggered to calculate the EAWS-based index. The algorithm selects the time-specific measurements from the MOCAP cameras and the sEMG wearable for each $r$-th activity of the assembly sequence. The following sections quantitatively describe the computational steps to digitize the Basic Postures (section 5.1.2), Action Forces (section 5.1.2), and MMH (section 5.1.2) EAWS Sections.

### Section 1: Basic Postures

This first algorithm branch automatically identifies time-dependent body angles and the related human postures to calculate the Basic Postures-informed KRIs, based on the computational steps described in Figure 5.2 (a).

Following the initialization of the MOCAP camera network according to Subection 5.1.1, the first computational step performs human skeleton fusion using the 3D coordinates of body joints (i.e., $Pos^c_{j,q}$) and the related measurement confidence levels (i.e., $CL^c_{j,q}$). These parameters are indexed by $j$, $q$, and $c$, representing the body joint, the recording frame, and the Kinect camera, respectively. The algorithm selects body joint coordinates with the highest confidence level as follows.

$$Pos_{j,q} = \arg\max_{j,c}\{CL^c_{j,q}\};\ \forall\ j = 1, ..., J \text{ and } q = 1, ..., Q \text{ and } c = 1, 2 \tag{5.2}$$

Subsequently, the returned body joint positions are indexed to the detected assembly activities (i.e., $r = 1, ..., R$) based on the computed HPIs (see section 5.1.2). To facilitate the assessment of relevant body angles, the human skeleton is recreated using the hierarchical structure depicted in Figure 5.2 (b), where the pelvis (i.e., Joint

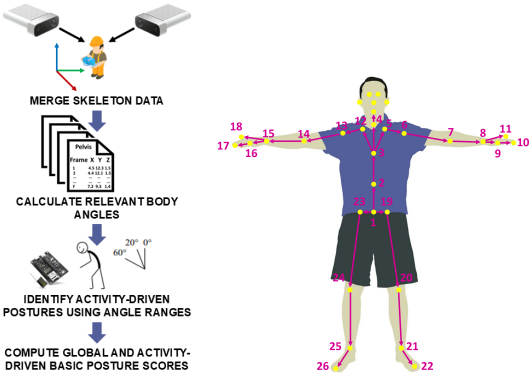


(A) Flow diagram for musculoskeletal risk assessment

(B) Human body joints captured by the Microsoft Azure Kinect cameras

FIGURE 5.2: Musculoskeletal evaluation

1) represents the root node. The EAWS screening tool defines several human movements from lumbar extension to arm positions; therefore, Appendix B lists the body joint groups considered to identify each posture. Based on this, the algorithm traverses the body tree with a depth-first order iterator to calculate two vectors. First, a 3D vector is computed between each joint and its parent (e.g., Joint 1 is the parent of Joint 2). Second, the program creates $G$ vectorial structures of body joint groups (i.e., $V^r_{g,q}$). In particular, $V^r_{1,q}$ represents the back vector between joints ranging from 1 to 4. The vector of the right leg, $V^r_{2,q}$, is formed by considering the body joints 1, 23, 24, and 25. Therefore, the angle between the worker's back and the right leg is given as follows, where $g$ and $g^{'}$ are equal to 1 and 2, respectively:

$$\Theta^r_{g-g',k} = \arccos\left(\frac{\mathbf{V^r_{g,q}} \cdot \mathbf{V^r_{g',q}}}{\|\mathbf{V^r_{g,q}}\|\|\mathbf{V^r_{g',q}}\|}\right);\ \forall q = 1, ..., Q \text{ and } g, g^{'} \in G \tag{5.3}$$

It is worth noting that this angle is computed for all postures and body joint groups in Table B1 of Appendix B, in addition to each $k$-th recording frame of the MOCAP-based network. However, $\Theta^r_{1-2,q}$ is not sufficient to adequately classify back inclinations. $\Theta^r_{1-3,q}$ is computed following the same procedure, where $g$ equal to 3 indexes the left leg. Based on Table B1, the involved joint numbers are 1, 19, 20, and 21.

Using $\Theta^r_{1-2,q}$ and $\Theta^r_{1-3,q}$, the algorithm scans all timeframes and performs activity-driven posture (i.e., $p = 1, ..., P$) recognition through the following if statements:

- **If** $\Theta^r_{1-2,q}$ and $\Theta^r_{1-3,q} < 20° \Rightarrow$ **Standing** (i.e., $p = 2$)

- **If** $20^\circ \leq (\Theta^r_{1-2,q}$ and $\Theta^r_{1-3,q}) \leq 60^\circ \Rightarrow$ **Low Bending** (i.e., $p = 3$)
- **If** $\Theta^r_{1-2,q}$ or $\Theta^r_{1-3,q} > 60^\circ \Rightarrow$ **High Bending** (i.e., $p = 4$)

Based on these statements, a duration is automatically assessed for each $p$-th EAWS posture and $r$-th assembly activity (i.e., $D^r_p$). $Tstart^a_p$ and $Tend^a_p$ represent the starting and ending timestamps, respectively. Subsequently, $D^r_p$ is mapped into risk scores (i.e., $PScore^r_p$) following the EAWS guidelines. For instance, a low bending duration of 16 seconds (i.e., $D^r_3$) corresponds to a $PScore^r_p$ equal to 12. It should be noted that some movements are mutually exclusive (e.g., standing, bending, and strong bending), while other postures can be assumed simultaneously (e.g., standing and trunk rotation). Additionally, posture-related parameters are indexed to $o$ to indicate the temporal occurrence of the $p$-th posture in $r$ (i.e., $D^r_{p,o}$ and $PScore^r_{p,o}$). The last processing step in activity-driven posture identification mitigates the acquisition noise of the MOCAP-based network and the intrinsic motion uncertainty of human workers. For example, consider three consecutive postures with known durations $D^r_{p,o-1}$, $D^r_{p',o}$, and $D^r_{p,o+1}$. The algorithm considers the two $p$-th postures as a single event if the following condition is verified.

$$D^r_{p+1,o} \leq \pi \tag{5.4}$$

where $\pi$ represents the minimum duration to hold an EAWS-driven posture. Trivially, merging postures requires updating all related parameters.

The resulting Activity-Driven and Global Action Forces Scores are computed using Eq. 5.5 and Eq. 5.6, respectively.

$$ADBPS^r = \sum_{o=1}^{R} \sum_{p=1}^{P} PScore^r_{p,o};\ \forall p, a \in r \tag{5.5}$$

$$GBPS = \frac{\sum_{r=1}^{R} ADBPS^r}{R} \tag{5.6}$$

### Section 2 - Action Forces

This algorithmic branch computes the second section of the EAWS index, focusing on the exerted forces of upper limbs (i.e., biceps and radial flexors) during task executions. Traditionally, muscular strength is defined as a subject's capability to apply a force over a given time window. The applied force is a complex phenomenon involving interactions with muscle fibers and the central nervous system [151]. Despite this data usually being acquired by dynamometers, [152] demonstrates, based on limits of agreements, that sEMG data streams are a reliable measure to detect

changes in muscle strength and muscle activity. Therefore, this algorithm leverages sEMG-based signals to assess Voluntary Contractions (%VC) as a function of MVC in workers' upper limbs and then associates these to action force scores defined by the EAWS screening tool [62]. This approach facilitates the development of this section by neglecting assumed postures.
Before evaluating muscular-driven VC and the related KRIs, the algorithm needs to be initialized for each worker according to the right path of Figure 5.3. This initialization involves $N$ sEMG acquisitions, capturing muscular datasets during resting and maximal isometric contraction scenarios. While the initial data streams help determine acquisition noise for each channel (i.e., $noise_m$), the muscle-driven $MVC_m$ (i.e., where $m = 1, ..., 4$) is computed based on the second set of recordings. The evaluated $VC_m$ is normalized using the corresponding $MVC_m$, and thus this parameter is represented as $\% \ VC_m$. Muscular measurements undergo denoising and conditioning through a three-step approach:

1. **Wavelet Package Decomposition (WPD)**: It splits signals into high and low-frequency coefficients (i.e., detail and approximation, respectively). The Daubechies 45 orthogonal mother wavelet is employed, known for its efficacy in handling sEMG data [153]. After decomposition, the sEMG information is recomposed by summing the approximation coefficient of the last order with the detailed ones.
2. **TKEO**: It enhances SNR and onset muscle activation detection [149].
3. 4**th-order low-pass Butterworth filter**: It obtains the envelope, removing frequency components at twice the signal bandwidth.

This three-step approach is applied to incoming sEMG data streams and is not repeated when analyzing the left part of the flow diagram in Figure 5.3. The algorithm computes acquisition $noise_m$ and $MVC_m$. The acquisition noise is approximated to three times the standard deviation of the signal in resting scenarios for any $m$-th active channel or muscle. Multiple acquisitions (i.e., $noise_m^n$, where $n = 1, .., N$) are recommended to enhance the metrological reliability of this parameter. The resulting $noise_m$ is equal to the mean of all acquisitions. $MVC_m^n$ is obtained by performing for a variable duration (i.e., $D_m^n$) isometric contractions of the biceps brachii and radial flexors. Similarly, $MVC_m$ and $D_m$ are obtained by averaging the maximal voluntary contraction and duration of each $n$-th recording and $m$-th sEMG channel, respectively. It's crucial to note that these parameters highly depend on operators' physical features, varying within the workforce and even between subjects' sides.
Following this worker and muscle-specific initialization procedure, the algorithm is ready to analyze sEMG measurements acquired during industrial working cycles as depicted by the left flow part in Figure 5.3. In the following, sEMG data streams are denoted as $x_{u,m}$, where $u$ represents the acquisition frame of the BITalino board. The

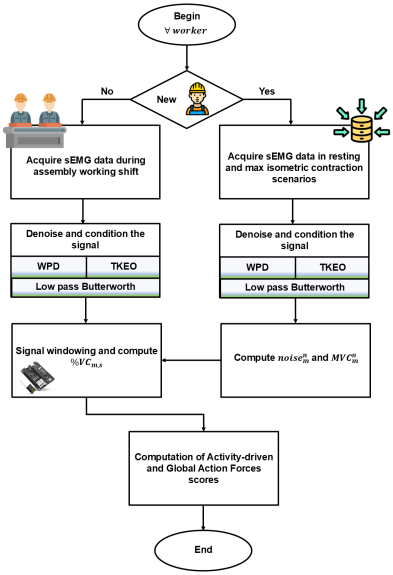


FIGURE 5.3: Flow diagram for evaluating muscular risk.

algorithm performs a signal windowing step to evaluate the $\%\ VC_m$. In particular, it defines muscle-specific overlapping sliding windows with duration (i.e., $Wdur_m$) and overlap (i.e., $over_m$) equal to $D_m$ and $D_m/2$, respectively. Within each $s$-th sliding window, the absolute magnitude of muscular contractions (i.e., $AMMC_{m,s}$) and related duration (i.e., $DMMC_{m,s}$) are computed by thresholding the signal energy as follows.

$$AMMC_{m,s} = \sum_{u=1}^{U} f(x_{u,m});\ \forall\ x_u \geq thr_m \text{ and } m = 1,\ldots,4 \tag{5.7}$$

$$DMMC_{m,s} = \sum_{u=u'}^{U} (x_{u+1,m} - x_{u,m});\ \forall\ x_{u',m} = thr_m \text{ and } m = 1,\ldots,4 \tag{5.8}$$

where $thr_m$ is equal to $noise_m$. As a result, the muscular activation and the $\%VC$ for each muscle and window are computed using the following equations.

$$MA_{m,s} = \frac{AMMS_{m,s}}{DMMC_{m,s}};\ \forall\ s = 1,\ldots,S \text{ and } m = 1,\ldots,4 \tag{5.9}$$

$$\%VC_{m,s} = \frac{MA_{m,s}}{MVC_m};\ \forall\ s = 1, \ldots, S \text{ and } m = 1, \ldots, 4 \tag{5.10}$$

It is worth noting that muscular activations might be dynamic and their distribution may be sparse among muscular groups and assembly tasks. Scaling this computational approach for each *r*-th activity in the assembly sequence, the previously mentioned parameters can be indexed also to *r*. For instance, $MA^r_{m,s}$ represents the muscular activation of the *m*-th recording channel during the *s*-th window of the *r*-th assembly task. Trivially, multiple *s* windows can belong to the same *r*-th assembly activity. Before computing the KRIs for the Action Forces section, $DMMC^r_{m,s}$ and $\%VC^r_{m,s}$ are mapped into EAWS scores based on the ergonomic tool's tabular values [62]. For instance, $\%VC^r_{m,s}$ equal to 17% provides an intensity score (i.e., $FScore^r_{m,s}$) equal to 6 points. Similarly, a duration score (i.e., $DFScore^r_{m,s}$) equal to 1.5 points is associated with a $DMMC^r_{m,s}$ of 10 seconds. The resulting Activity-Driven score is computed using the following equation.

$$ADAFS^r_m = \frac{\sum_{s=1}^{S} FScore^r_{m,s} \times DFScore^r_{m,s}}{S};\ \forall s \in r \tag{5.11}$$

The score for the *r*-th activity (e.g., $ADAFS^r$) is equal to the greatest value of $ADAFS^r_m$. Based on $ADAFS^r$, the Global Action Forces score is given as follows.

$$GAFS = \frac{\sum_{r=1}^{R} ADAFS^r}{R} \tag{5.12}$$

The next section integrates posture-dependent information and muscular activities to evaluate the ergonomic risk in handling heavy loads.

### Section 3 - Manual Material Handling

This third algorithm branch detects MMH events and evaluates the physical resilience of workers through Handling KRIs. To achieve this purpose, the enabling IoT technologies measurements and process metadata are leveraged as conceptually depicted in Figure 5.4. Firstly, the operator-centric manufacturing sequence is divided into *R* assembly activities through the RFID-based automatic recognition of HPIs (refer to Algorithm 2 in section 5.1.2). In particular, this activity segmentation is performed with $T_r$ of detected tasks. The algorithm then iterates over assembly tasks based on $x_r$. This binary variable is equal to 1 if the associated task processes a WIP weighing 3 kg or more; otherwise, it is equal to 0 [62]. The weight is process metadata retrieved from the use case's information systems. Within activities having $x_r$ equal to 1, an additional windowing step is executed (see Figure 5.4). The target is to exclude tool usage time windows using $TTstart_t$ and $TTend_t$. The

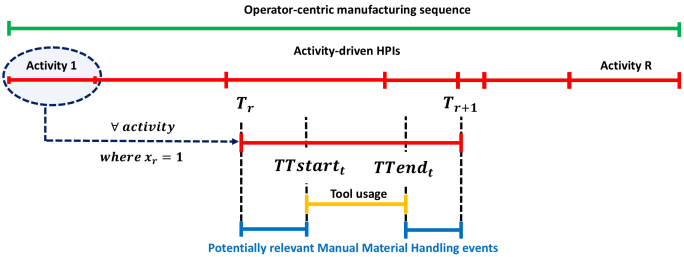


FIGURE 5.4: Time-driven approach to detect potentially relevant MMH events.

complementary time intervals (i.e., the blue-colored ones) represent potentially relevant MMH events. For each event, overlapping sliding windows segment the sEMG-based data streams to compute $\%VC_{m,s}$. Significant MMH windows are distinguished by $\%VC_{m,s}$ greater than a threshold (i.e., $\omega$) for at least one muscular group. Therefore, $Tstart_v^r$ and $Tend_v^r$ represent the starting and ending timestamps of the $v$-th relevant MMH event during the $a$-th assembly activity. Four different postures need to be detected within these windows. These include trunk upright, little trunk bending, deep trunk bending, and asymmetric movements or kneeling. In particular, a score risk (i.e., $MMHPS_{h,v}^r$) is associated with these MMH postures (i.e., $h = 1, ...4$). For instance, while carrying a load in the trunk upright position ($h = 1$) scores 1 posture point, in the deep trunk bending position ($h = 3$), it scores 4 posture points. It is worth noting that multiple postures may occur in the same $v$-th relevant MMH event. The resulting posture score of that MMH event (i.e., $MMHPS_v^r$) is equal to the greatest value of all postures. The second risk metric targets the duration of the entire MMH event (i.e., $D_v^r$ ), derived from $Tstart_v^r$ and $Tend_v^r$. $D_v^r$ is multiplied by the total duration of the work shift, typically set at 480 minutes, and then divided by the duration of the specific manufacturing task under consideration, which is assumed to repeat cyclically. The resulting frequency $F_v$ is mapped into $MMHFS_v$ following the EAWS tabular values. For instance, $F_v^r$ equal to 5 provides an $MMHFS_v$ of 1 point. Finally, $WS^r$ represents the risk score associated with the handled weight during the $r$-th assembly activity with $x_r$ equal to 1. The EAWS lists different risk scores for carried loads based on the worker's gender. This metadata is not considered to ensure the privacy of final users and facilitate the architecture adoption in unionized industries. Therefore, carried load risk scores always refer to the female gender, which is distinguished by higher values. For instance, lifting a 5 kg weight corresponds to 1.5 load points (i.e., $WS^r$). Finally, the Activity-driven and Global MMH scores are computed using:

$$ADMMHS^a = \frac{\sum_{v'=1}^{V}(MMHPS_v^r + WS^r) \times MMHFS_v}{V}; \ \forall v' \in r \tag{5.13}$$

$$GMMHS = \frac{\sum_{r=1}^{R} ADMMHS^{r}}{R} \tag{5.14}$$

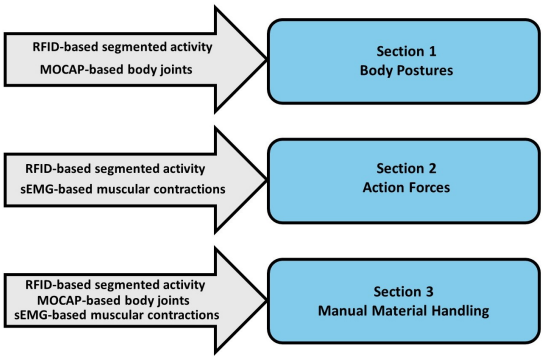


FIGURE 5.5: Data model of the proposed digital architecture.

To conclude this high-detailed and quantitative section, Figure 5.5, combined with List of Symbols and Appendix B, highlights the key steps to calculate three EAWS sections. After the data acquisition of HPIs, workers' body joints, and upper limbs' muscular contractions, the computational algorithms are triggered to extract EAWS-informed KRIs. The first processing step targets the segmentation of assembly tasks and tool usage in human-centric manufacturing systems (see Algorithm 2). The activity recognition is a strategic output of the algorithm since it enables the development of task-specific risk metrics. Subsequently, three parallel computational streams are triggered to digitize the following EAWS sections:

- **Section** 1 **- Basic Postures:** After reconstructing the worker's skeleton using MOCAP cameras' confidence levels (see Eq.5.2), this algorithm branch iterates over the body joints to create muscular group vectors and then evaluate angles among them (see Eq. 5.3). Appendix B lists the body joint groups to successfully identify relevant body angles. These parameters are exploited to detect EAWS-driven postures. For example, section 5.1.2 presents three If-statements to identify *standing*, *bent forward*, and *strongly bent forward* based on angles formed between the back and the legs. Finally, Eq. 5.5 and 5.6 formalize the Activity-driven and Global Basic Posture KRIs.
- **Section** 2 **- Action Forces:** This algorithm branch leverages sEMG-based upper limbs' contractions to evaluate exerted forces during task executions. Following a pre-processing step that acquires worker-specific hyperparameters such as $noise_m$ and $MVC_m$, sEMG-based data streams are leveraged by overlapping windows. For each muscle-driven $w$-th window, the program

extracts $\%VC_{m,w}$ in four different steps (see from Eq. 5.7 to Eq. 5.10). Finally, EAWS scores of relative voluntary contractions and related durations are leveraged to compute the Activity-driven and Global Action Forces KRIs (i.e., Eq. 5.11 and 5.12).

- **Section 3 - Manual Material Handling:** This third computational stream evaluates workers' risk during handling operations. First, the algorithm iterates over assembly activities with products weighing more than 3 kg and identifies potentially relevant MMH events by removing tool usage time windows (see Figure 5.4). The mentioned events are labeled as relevant if at least one muscular $\%VC_{m,w}$ is greater than a threshold. It is worth noting that the calculation of relative voluntary contractions follows the same procedure described to digitize the previous EAWS section. Within relevant MMH events, the algorithm assigns EAWS scores to the assumed posture (i.e., $MMHPS_v^a$), the frequency of the $v$-th event (i.e., $MMHFS_v^a$), and the load weight (i.e., $WS^a$). Based on these parameters, the Activity-Driven and Global Manual Material Handling KRIs (i.e., Eq. 5.13 and 5.14) are computed.

### 5.1.3 Ergonomic Decision Support System

Benefiting from the discussed computational steps to digitize the EAWS ergonomic tool, Table 5.2 summarizes how time-dependent assembly activities can be structured for a given working time window. The first five columns are generated by

TABLE 5.2: Example of time-dependent assembly activities for a monitored worker.

| Task ID | Start | End | Tool | Tool usage [sec] | Basic Posture | Action Forces | MMH | Whole Body |
|---|---|---|---|---|---|---|---|---|
| Task 1 | 14:31:23 | 14:37:00 | Screwdriver | 215.4 | 37 | 22.9 | 0 | 37 |
| Task 2 | 14:42:28 | 14:43:59 | Manual | 91.0 | 35 | 127.5 | 0 | 127.5 |
| Task 3 | 14:57:40 | 14:58:18 | Manual | 38.3 | 29 | 51 | 2.2 | 51 |
| ... | ... | ... | ... | ... | ... | ... | ... | |
| Task N | 15:12:35 | 15:13:56 | Hammer | 21.1 | 22 | 0 | 0 | 22 |

automatically identifying HPIs. Task segmentation is facilitated by RFID passive tags placed on components and WIP products, while continuous readings of tool tags provide information on their activity-based usage. A task is trivially labeled as *Manual* when no tools are detected during its duration. The columns for Basic Posture, Action Forces, and MMH are developed based on the algorithms described from section 5.1.2 to section 5.1.2. Finally, the last field (i.e., Whole Body) integrates the EAWS scores from the previous three categories to yield an aggregate risk metric. EAWS rules dictate that each manufacturing activity should be associated with just one score: a task can be identified as risky either due to the postures, the forces exerted, or the load lifted by the operator [62]. Therefore, the Whole Body Activity-Driven Score is determined from the highest score among the three. The Global Whole Body Score, on the other hand, is the average of the Whole Body

Activity-Driven Scores. This EAWS-based scoring system is crucial for identifying operator-driven safety weaknesses in manufacturing systems. However, it falls short of revealing the root causes of potentially hazardous events affecting workers' physical resilience. For instance, a high Basic Posture score may be driven either by bending postures or by the arms' positions above shoulder level; depending on the case, there are different considerations to make regarding the musculoskeletal risk to which the operator is subjected. Time-driven insights are also overlooked, and underestimating the effect of posture duration can lead to sub-optimal workplace redesign approaches and strategies. These limitations also apply to Action Forces and MMH scores. For example, the latter fails to highlight the most exposed muscles and their % VC during task executions. To address this gap, callback functions are developed to complement the discussed scores with additional KRIs. These KRIs are grouped into three different levels of detail, as follows:

- **Musculoskeletal**: Global Basic Posture Score; Activity-Driven Basic Posture Score; Fine-Grained Posture Score; Body Angle Evolution.
- **Muscular**: Global Action Forces Score; Activity-Driven Action Forces Score; Muscle-Specific and Time-Oriented % VC; Muscle-Specific Action Forces Score.
- **Handling**: Global MMH Score; Activity-Driven MMH Score; Activity-Driven Load Data; Muscle-Specific and Time-Oriented % VC; Postures Time in MMH Windows.

The effectiveness of this digital architecture in automating the EAWS assessment is substantiated in the industrial-like pilot environment described in section 5.2. Subsequently, section 5.3 delves into the managerial implications of monitoring workers' physical resilience through the proposed multi-dimensional KRIs.

## 5.2 Case Study

An extensive experimental campaign was conducted in the industrial-related pilot environment depicted in Figure 5.6 to validate the IoT-based digital architecture. The objective is to automatically evaluate the operator-centric EAWS index and the related KRIs during the assembly of a drawer at an industrial-like WS. The selected piece of home furniture has the following dimensions: 67 cm $\times$ 69 cm $\times$ 39 cm (i.e., H $\times$ L $\times$ W). The assembly sequence involves 22 distinct tasks; for a detailed explanation of the process, interested readers are invited to refer to Appendix B. Operators perform the sequence using four manual tools: a hammer, a Phillips screwdriver, a slotted screwdriver, and a hexagonal Allen key. The human factor is digitized through the set of IoT technologies discussed in section 5.1.1. The monitored operator wears an RFID smart glove to automatically detect HPIs (see Figure 5.7). Assembly tasks and tool usage are automatically recognized based on

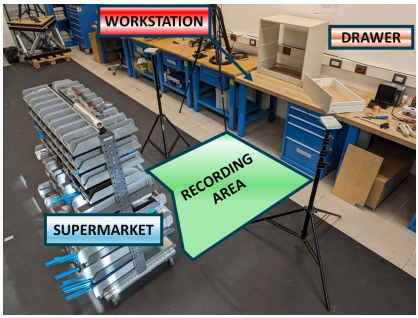


FIGURE 5.6: Industrial-like pilot environment.

components (e.g., fasteners) and tools retrieved from the supermarket and the WS, thanks to RFID tagging in the pilot environment. Passive tags are placed in these storage locations, enabling the recognition of fine components picking and facilitating the activity segmentation process in the assembly sequence. Tools are also passively tagged to track their usage. For instance, the assembly process begins with the operator interacting with screw tags, which initiates the first activity. Following the predefined sequence, the worker uses a Phillips screwdriver to attach plastic plates onto drawer boards. Throughout this task, the RFID antenna inside the smart glove continuously scans the tool's code as long as it remains in the operator's hand. The activity concludes as the operator picks the next components required in the assembly sequence.

The RFID datasets stored in InfluxDB are imported into MATLAB and temporally synchronized with the other measurements. The MOCAP videos are converted to 3D human body joints using a C# script, while the 4-channel sEMG data streams are acquired using a Python script and imported into MATLAB in CSV format. To limit potential body joint occlusion that may affect EAWS scores [34], the MOCAP network consists of two cameras placed to the sides of the recording area (see Figure 5.6). Concerning sEMG data, Ag–AgCl disc-type disposable electrodes are used to record muscular contractions. Each BITalino channel is connected to a cable that splits into three ends for electrode attachments. The electrodes are carefully positioned on relevant muscle groups on the operator's upper limbs. As illustrated in Figure 5.7, they are divided equally on the biceps and radial flexors of each body side.

Based on the extensive discussion of the algorithms reported in section 5.1.2, the following part validates this digital architecture, demonstrating that the KRIs for Basic Postures, Action Forces, and MMH offer valuable insights for assessing the well-being of operators in human-centric manufacturing systems, according to Industry 5.0 pillars.

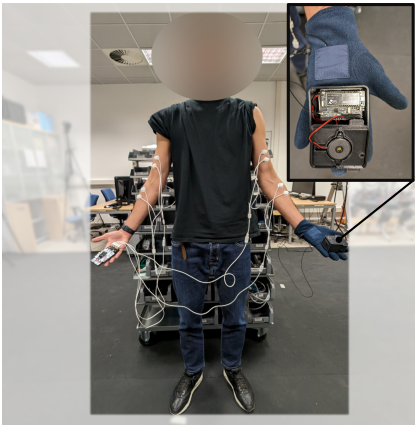

FIGURE 5.7: The subject is wearing the RFID smart glove on the left hand (with a detailed view of the Pyscan board in the inset) and the BITalino electrodes positioned on the upper limb muscles.

## 5.3 Results & managerial insights

The digital architecture proposed for assessing the physical resilience of manufacturing operators undergoes validation during the assembly of the home furniture drawer described in section 5.2. The example sequence presented in this part, which lasts 51.7 minutes, is decomposed into 22 assembly tasks by the automatic detection of RFID-driven HPIs. In Figure 5.8, which shows this time-dependent subdivision, also including tool usage, some of the activities are repeated more than once. A detailed description of the task sequence can be found in Appendix B. This process-

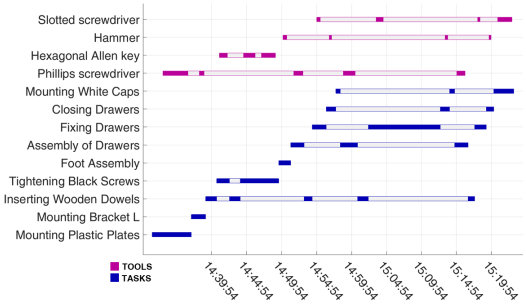


FIGURE 5.8: The segmented manufacturing sequence, denoted as HPIs, along with tool usage: some of the 22 blue tasks are repeated over time, and each of the 4 violet tools is utilized multiple times.

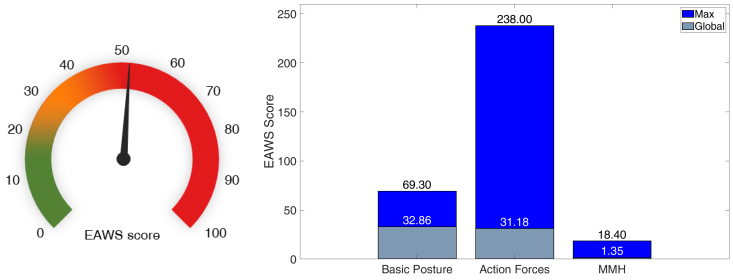


(A) Global Whole Body Score.

(B) Global Section-Driven Scores.

FIGURE 5.9: Preliminary insights into operator-centric physical resilience.

oriented insight provides two significant managerial implications. On the one hand, the architecture identifies the maximum, minimum, and average duration of assembly tasks. For instance, while one of the *Fixing Drawers* activities presents the longest execution time of 615.0 seconds, which involves the use of a slotted screwdriver for 61.3 seconds, the fastest assembly activity is one of the *Mounting White Caps*, which lasts 38.3 seconds. This information is relevant for identifying manufacturing weaknesses since task duration can be compared with historical data. In this regard, discussions with employees may reveal hazardous ergonomic scenarios. On the other hand, the architecture provides valuable information on tool usage. For example, in this assembly sequence, more than a third of the tasks are executed without tools. While the hexagonal Allen key is the least utilized tool, accounting for 9 % of the total time of the process, the Phillips screwdriver is the most employed tool, reaching 23 %. These insights are important in monitoring multiple WSs for a given manufacturing sequence. Indeed, utilization ratios can justify the economic initiative of purchasing additional tools to avoid potential bottlenecks.

Concerning the operator's ergonomic aspects, the digital architecture firstly returns the overall EAWS score. Figure 5.9 (a) highlights the Global Whole Body Score of 51.03 points, indicating a high-risk level. However, this initial ergonomic insight fails to pinpoint the most hazardous EAWS scores for the health of the monitored worker. Figure 5.9 (b) fills this gap by outlining the Global Section-Driven Scores, which include the Global Basic Posture score, the Global Action Forces Score, and the Global MMH Score, comparing them with the maximum section points totaled by the different assembly tasks. This insight, which is strategic to prioritize areas of improvement in the manufacturing system design, does not detail the riskiest tasks in the assembly sequence nor their worrisome parameters. Without this information, production supervisors have no valid basis to reconfigure the WS design or

the assembly process. To avoid such a notable limitation, the following sections discuss the effectiveness of monitoring assembly sequences through the proposed KRIs and demonstrate the benefits of digitizing the EAWS index to increase the visibility of ergonomic weaknesses and safeguard the physical resilience of manufacturing operators.

### 5.3.1 Muscoloskeletal Risk

Four postures significantly contribute to the Global Basic Posture Score, totaling 32.8 out of 69.3 EAWS points (refer to Figure 5.9 (b)). Specifically, these postures involve two levels of lumbar extension and asymmetric movements. While standing and bending scenarios account for 21.4% and 64.3% of the total score, the remaining 14% is linked to trunk rotation and far-reach movements, with 3 and 1 points assigned to them, respectively. Although this score suggests a moderate risk according to the EAWS index [62], it fails to highlight the most critical tasks in the musculoskeletal dimension. Leveraging RFID-enabled HPIs, Figure 5.10 displays the Activity-Driven Posture Score in the time domain. It is evident that most of the

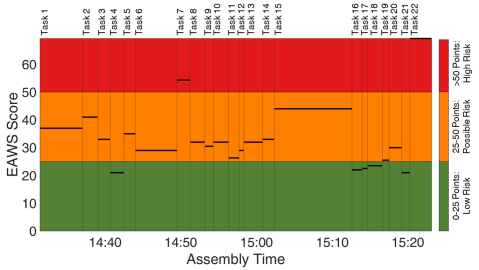


FIGURE 5.10: Activity-Driven Basic Posture Score: the sequence of tasks and the associated EAWS risk levels are reported.

assembly task scores fall within the medium-risk category (i.e., the range between 25 and 50 EAWS points), while 2 tasks stand out with scores exceeding 50 points, indicating high ergonomic risk. In effectively redesigning the manufacturing process, plant supervisors should prioritize the analysis of the most concerning tasks from a musculoskeletal perspective. For instance, the last assembly activity (i.e., *Mounting White Caps*) records the highest score, contributing 69.3 EAWS points over 171.7 seconds. In addition to enhancing visibility into operator and activity-driven musculoskeletal risk, pinpointing the most impactful postures on each task score is strategic. Therefore, Figure 5.11 depicts the Fine-Grained Posture Score for every movement performed by the operator during the last assembly activity: light and dark blue bars represent actual (i.e., measured) and maximum EAWS scores, respectively. This task involves three main steps: a) Retrieve the two previously

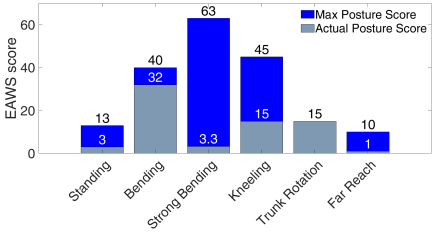


FIGURE 5.11: Fine-Grained Posture Score: the actual (i.e., measured) and maximum achievable scores according to the EAWS database are reported for the pertinent postures of task #22.

assembled drawers from the adjacent worktable and place them inside the dresser, b) Secure all the drawers using a slotted screwdriver, and c) Insert the last drawer into the dresser. For further details, refer to Appendix B. This scenario may have critical implications for the physical resilience of workers since it might trigger potentially relevant bending postures (see Figure 5.11) or burden the muscular activation of the upper limbs; the second implication will be better highlighted later. The fine-grained KRI outlines that the bending and trunk rotation postures are the most critical movements, accounting together for 47 EAWS points. However, this risk metric falls short of suggesting the most appropriate operator-centric process reconfiguration approaches. Hazardous musculoskeletal scenarios may be driven by extremely worrisome body angles for a limited duration or safer body angles for longer time windows, requiring different managerial approaches. While the former can be addressed with visual management instructions, the latter suggests the need to redesign the entire WS or even the workplace. To enable an informed decision-making process, Figure 5.12 depicts the evolution of the operator's back angle during the last assembly task. According to EAWS ranges, this angle influences the detection and score of three basic movements: the standing posture falls between $0^\circ$ and $20^\circ$, the bending posture ranges from $20^\circ$ to $60^\circ$, and the strong bending posture is beyond $60^\circ$. As depicted in Figure 5.12, the majority of time-driven back angles fall within the bending range. Specifically, the standing posture lasts 39.6 seconds (i.e., 23.1% of the assembly activity time), and the two bending scenarios account for 120.8 and 11.1 seconds, respectively. These musculoskeletal-driven values indicate significant stress on the worker's physical resilience during the final assembly task, with the last part being the most critical for the operator's back. The graph in Figure 5.12 demonstrates frequent bending by the worker to insert the last drawer, suggesting that placing the furniture on the floor is not ergonomically optimal. To mitigate this, plant supervisors should consider introducing a height-adjustable support for the drawer unit, aiming to maintain the operator's back angle below $20^\circ$ whenever possible. Conversely, the trunk rotation posture is distinguished by an average lumbar angle of $25.5^\circ$. The high EAWS score is due

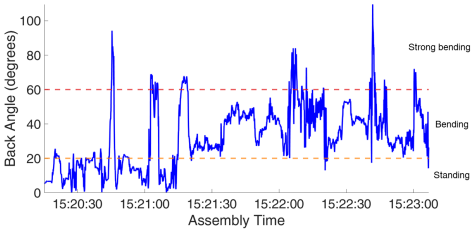


FIGURE 5.12: Body Angle Evolution: the lumbar extension angle for task #22 is monitored. Postures are identified based on the angle's value over time: *standing* if the angle is less than 20°, *bending* if the angle is between 20° and 60°, and *strong bending* if the angle exceeds 60°. To ensure posture recognition accuracy, the algorithm corrects fluctuations by requiring the angle to remain within the same range for a certain number of consecutive frames.

to critical angle values lasting for a prolonged period of 125.5 out of 171.7 seconds, accounting for 73.1% of the activity duration. These metrics suggest different managerial implications compared to the bending postures. Potential trunk rotation disorders can be prevented by ensuring that frequently accessed tools and components are within easy reach. This first ergonomic dimension is complemented in the following two sections by monitoring the Muscular and Handling Risks.

### 5.3.2 Muscular Risk

This second set of EAWS-oriented KRIs delves deeper into the ergonomic analysis by examining potentially hazardous muscular efforts during the assembly tasks. While the Global Action Forces Score of 31.1 EAWS points suggests a medium overall risk, it is crucial to adopt a top-down approach to identify specific activities that may impact operators' muscular risk. The analysis begins with the RFID-enabled Activity-Driven Action Forces Score. As illustrated in Figure 5.13, approximately 68.1% of the monitored activities fall within the low-risk band. The highest score among these tasks is observed in the first activity (i.e., *Mounting Plastic Plates*), which totals 22.9 EAWS points. This task involves inserting and screwing plastic plates onto the lateral axes of the drawer (see Appendix B) and does not entail significant arm exertion. However, its extended duration of 336.8 seconds induces some muscular stress during the final screwing phase. Further prolonging this activity would escalate the muscular risk level. Conversely, the lowest EAWS values group the manual tasks ranging from 8 to 11, where the monitored worker assembles drawers on the WS without significant muscular activation (% VC) in the upper limbs. However, three assembly activities account for more than 100 EAWS points, requiring in-depth evaluations. In particular, the third task (i.e., *Inserting Wooden Dowels*) has the highest score, equal to 238 EAWS points. This activity involves the

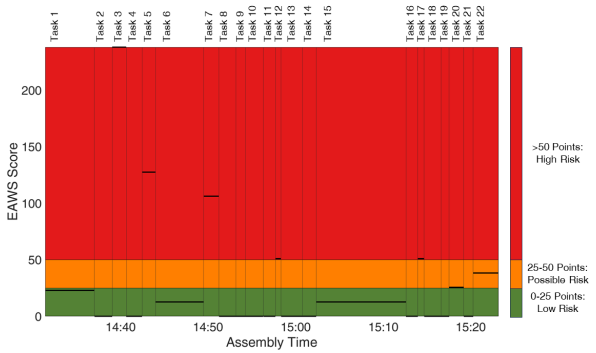


FIGURE 5.13: Activity-Driven Action Forces Score: the sequence of tasks and their associated EAWS risk ranges are presented.

manual insertion of fixing dowels into the narrow axes of the drawers. Despite its brief duration of 95.3 seconds, it requires considerable muscular effort from the monitored operator. The intrinsic limitation of this first KRI is its inability to highlight the most physically stressed muscular groups. To address this, the amplitude in mV of the sEMG-based muscular contraction is shown in Figure 5.14 for the right (R) and left (L) upper limbs, where the colors of the denoised signals correspond to the channel-associated EAWS risk level [62]. It can be seen that both radial flexors experience significant stress over the activity time. However, focusing solely on the acquired sEMG signal fails to highlight the muscle-specific % VC. These outputs are obtained by leveraging the second algorithm branch discussed in section 5.1.2: the computations define sliding windows and assign each of them a % VC, as reported in Figure 5.15. These non-overlapping windows facilitate a detailed assessment of muscle activation during specific intervals in the assembly tasks. The comparison between the KRIs reported in Figures 5.14 and 5.15 reveals two distinct scenarios. First, the amplitude of the R radial flexor sEMG signal is high during the initial time window, corresponding to a 66.7% VC. Second, the sEMG signal is visually intense in the last two Channel-4 windows, which, however, correspond to 5.5% and 1.5% VC. Here it is important to underline that since % VC is a function of the maximum muscle effort, large signal amplitudes do not necessarily correlate with high muscle activation. Furthermore, the third KRI (see Figure 5.15) points out valuable insights on the time domain. While the muscular activation of the R forearm (i.e., 66.7% VC) is registered for 57.3 seconds, the L forearm accounts for 40.5% VC over the entire task. These prolonged muscular stresses are mirrored in the Muscle-Specific Action Forces Score reported in Figure 5.16. While the R and L forearms accumulate 238 and 127.5 EAWS points, respectively, both biceps are green-colored since their greatest score is 17 points. It can be concluded that the risk level for the operator's forearm muscles is highly critical in this activity. The EAWS score

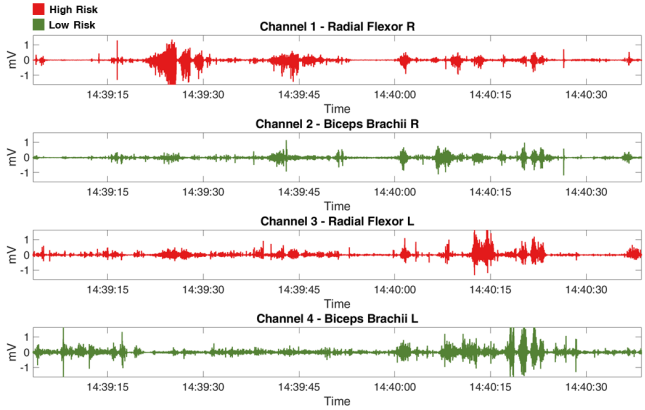


FIGURE 5.14: EMG Raw Signal: The normalized signals recorded by the four surface electrodes positioned on the operator's upper limbs are depicted for task #3. The signals are color-coded according to the EAWS risk level associated with the channel-specific score.

of the right arm, likely the dominant one in this case, becomes the definitive risk measure of the task. A potential solution to lowering the analyzed score is to adopt tools that can facilitate the manual insertion of wooden dowels. The musculoskeletal and muscular dimensions of physical resilience are finally complemented by the handling risk that quantifies the safety of workers in process-related load-lifting operations.

### 5.3.3 Handling Risk

The assessment of the operator's physical resilience concludes with a discussion on Handling KRIs. Although the Global MMH Score, equal to 1.3 EAWS points, suggests a low-risk level (see Figure 5.9 (b)), it is essential to note that the Handling Risk is solely computed when the operator's activities involve moving, lifting, holding, pushing, or pulling loads exceeding 3 kg (refer to section 5.1.2).

In the considered assembly sequence, 4 out of 22 tasks fall into this category (i.e., tasks 7, 12, 17, and 22). Therefore, the average of the scores is not informative. Following the same top-down approach discussed in the previous risk metrics, the analysis is refined by the Activity-Driven MMH Score. Inspecting Figure 5.17, it is evident that the assembly sequence considered does not report major critical MMH issues for the monitored operator, as the four relevant activities have an EAWS score lower than 25. However, proceeding with the analysis is necessary to illustrate the validity of the approach.

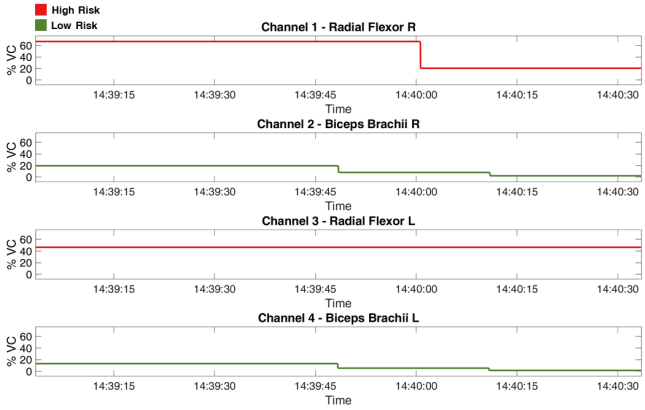


FIGURE 5.15: Muscle-Specific and Time-Oriented % VC: The % VC computed for the four surface electrodes placed on the operator's upper limbs is depicted for task #3. The values are color-coded based on the EAWS risk level associated with the channel-specific score.

Figure 5.17 highlights that the last task (i.e., *Mounting White Caps*) registers the highest MMH score, corresponding to 18.4 EAWS points. This task, as previously outlined in section 5.3.1, entails placing two drawers inside the dresser, securing all drawers using a slotted screwdriver, and inserting the final drawer into the dresser (refer to Appendix B). As the task has been already identified as critical from the musculoskeletal perspective, it is pivotal to further investigate other potential assembly-related weaknesses. For instance, Figure 5.18 correlates the handled loads with the associated load points. It is worth noting that the seventh task registers the highest lifted load, which corresponds to the furniture without drawers, weighing 7.18 kg. The remaining activities (i.e., tasks 12, 17, and 22) handle the drawers and thus manage lower weights (i.e., 3 kg). Therefore, to understand why the most critical activity is the last one, it is necessary to identify the MMH time windows within this task. The analysis narrows down to identify the muscle-dependent activation to assess the postures assumed by the operator during the MMH events. Figure 5.19 presents the Muscle-Specific and Time-Oriented % VC, highlighting potentially hazardous activation in two different time windows, from 15:20:15 to 15:20:49 and from 15:22:50 to 15:23:06. In both these time intervals, the R forearm activation exceeds the MMH threshold of 16.7 %, ranging from 20.7% to 17% VC. The threshold of 16.7% VC was selected as it is the minimum value necessary to attribute an intensity score to the applied forces [62]. Specifically, the analyzed KRI demonstrates two aspects. Firstly, it confirms that the radial flexor muscular group is the most

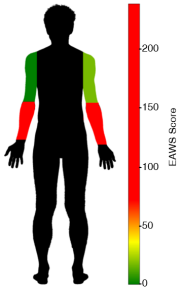


FIGURE 5.16: Muscle-Specific Action Forces Score: The four analyzed muscle groups (i.e., radial flexors and biceps brachii) are depicted for task #3. Each group is associated with a color corresponding to the intensity of the EAWS score.

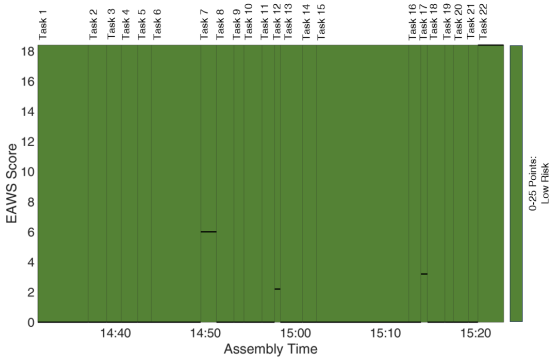


FIGURE 5.17: Activity-Driven MMH Score: the sequence of tasks and the associated EAWS risk ranges are reported.

stressed over the entire assembly process. To lower such activation, plant supervisors may consider purchasing lifters, or eventually cobots, to complement the physical capabilities of the workforce. Secondly, MMH events occur during both the considered time windows. In the initial time window, the operator retrieves the two previously assembled drawers from the adjacent worktable and positions them inside the dresser; in the subsequent time frame, the operator inserts the last drawer into the dresser. The algorithm for posture detection is executed on these particular time intervals of the analyzed activity. Postures Time in MMH Windows indicates the duration of postures, obtained as a percentage of the ratio between the number of frames for which a certain movement lasts and the total frames contained in the time windows. Notably, the first three bars in Figure 5.20 represent mutually exclusive postures (i.e., the percentage sum of these movements is 100),

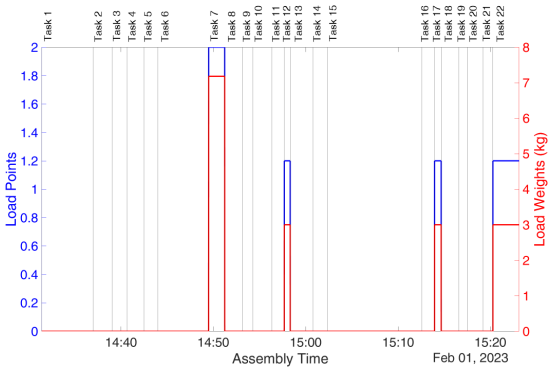


FIGURE 5.18: Activity-Driven Load Data: the EAWS scores and weights of loads that the operator lifts during the execution of assembly tasks are provided.

while the last four bars contain postures that can be cumulative with each other or with the first three. However, the posture considered in the final activity score is the one posing the highest risk among those assumed by the operator during the task (see section 5.1.2). In this instance, the trunk rotation posture emerges as the most hazardous, comprising 92.3% of the total task duration, with an average critical angle of 31.3 °. Although overlooked in the final score, the bending movement also has a significant impact, occupying 92% of the time with an average angle of 29.7 °. These postures are the most critical in the assembly test and also affect the musculoskeletal risk perspective. Possible ergonomic enhancements include organizing tools and materials for easy access without unnatural movements, ensuring workbenches are adjusted to the correct height, and utilizing ergonomic equipment such as assisted mechanical arms to reduce the required physical effort. Additionally, raising awareness among operators about health risks associated with incorrect postures and implementing work rotation policies can help diversify tasks and reduce the repetitiveness of motion, thereby mitigating accidents.


FIGURE 5.19: Muscle-Specific and Time-Oriented % VC: the graph displays the % VC computed for the four surface electrodes positioned on the operator's upper limbs for task #22. The values are color-coded based on the EAWS risk level associated with the channel-specific score, with highlighted time windows of interest.

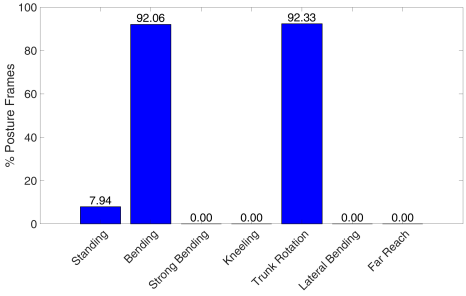


FIGURE 5.20: Posture Time in MMH Windows: the percentage of time spent in MMH postures relative to the total duration of task #22 is reported.

# Chapter 6

# PhD activities

"The streets I used to walk on
Are full of broken glass
And everywhere I'm looking
There's memories of my past"
– *The Rolling Stones, Whole Wide World, 2023*

The scientific contribution and activities conducted during the PhD are reported in the following sections.

**Journal papers**

- Tomelleri, F., **Sbaragli, A.**, Picariello, F., & Pilati, F. (2024). Digital ergonomic assessment to enhance the physical resilience of human-centric manufacturing systems in Industry 5.0. Journal of Manufacturing Systems, 77, 246-265.
- Pilati, F., **Sbaragli, A.**, Ruppert, T., & Abonyi, J. (2024). Goal-oriented clustering algorithm to monitor the efficiency of logistic processes through real-time locating systems. International Journal of Computer Integrated Manufacturing, 1-17.
- Pilati, F., & **Sbaragli, A.** (2023). Learning human-process interaction in manual manufacturing job shops through indoor positioning systems. Computers in Industry, 151, 103984.

**Conference proceedings**

- **Sbaragli, A.**, Tomelleri, F., Picariello, F., Picariello, E., & Pilati, F. (2024). Safe Operator 5.0 digital architecture: towards resilient human-centric manufacturing systems. IFAC-PapersOnLine, 58(19), 265-270.
- Tomelleri, F., **Sbaragli, A.**, Picariello, F., & Pilati, F. (2024). Safe Assembly in Industry 5.0: Digital Architecture for the Ergonomic Assembly Worksheet. Procedia CIRP, 127, 68-73.
- De Vito, L., Picariello, E., Picariello, F., Rapuano, S., Tudosa, I., **Sbaragli, A.**, & Pilati, F. (2024, June). IoT-Based System for Monitoring the Well-Being of Industrial Operators Through Wearable Devices. In 2024 IEEE International Symposium on Medical Measurements and Applications (MeMeA) (pp. 1-6). IEEE.
- Ghafoorpoor Yazdi, P., **Sbaragli, A.**, Peters, L., Pilati, F., & Thiede, S. (2024, April). Cyber Physical System for Reconfigurable Learning Factories: Combining 3D Simulations, Reconfigurable Layouts and Real-Time Locating Systems. In Conference on Learning Factories (pp. 28-35). Cham: Springer Nature Switzerland.
- Pilati, F., **Sbaragli, A.**, Papini, G. P. R., & Capuccini, P. (2023, June). An Artificial Neural Network Architecture to Classify Workers' Operations in Manual Production Processes. In International Conference on Flexible Automation and Intelligent Manufacturing (pp. 805-812). Cham: Springer Nature Switzerland.
- De Vito, L., Picariello, E., Picariello, F., Tudosa, I., **Sbaragli, A.**, Papini, G. P. R., & Pilati, F. (2023, June). Measurement System for Operator 5.0: a Learning Fatigue Recognition based on sEMG Signals. In 2023 IEEE International Symposium on Medical Measurements and Applications (MeMeA) (pp. 1-6). IEEE.
- Pilati, F., **Sbaragli, A.**, Tomelleri, F., Picariello, E., Picariello, F., Tudosa, I., & Nardello, M. (2023, June). Operator 5.0: Enhancing the Physical Resilience of Workers in Assembly Lines. In 2023 IEEE International Workshop on Metrology for Industry 4.0 & IoT (MetroInd4. 0&IoT) (pp. 177-182). IEEE.
- Wolf, M., Rantschl, M., Auberger, E., Preising, H., **Sbaragli, A.**, Pilati, F., & Ramsauer, C. (2022). Real time locating systems for human centered production planning and monitoring. IFAC-PapersOnLine, 55(2), 366-371.
- Pilati, F., **Sbaragli, A.**, & Brunelli, D. (2022). Indoor positioning systems to digitalize manual production processes. SUMMER SCHOOL FRANCESCO TURCO. PROCEEDINGS.

- Pilati, F., **Sbaragli, A.**, Nardello, M., Santoro, L., Fontanelli, D., & Brunelli, D. (2022). Indoor positioning systems to prevent the COVID19 transmission in manufacturing environments. Procedia Cirp, 107, 1588-1593.

**Contributions in press/under review**

- **Sbaragli, A.**, Ghafoorpoor Yazdi, P., Thiede, S. & Pilati, F. (2024) A cyber-physical architecture to monitor human-centric reconfigurable manufacturing systems. Journal of Intelligent Manufacturing, 3rd round of reviews ongoing.
- **Sbaragli, A.**, Santoro, L., Nardello, M., Brunelli, D. & Pilati, F. (2024) SHIELD4US: how to prevent pandemics in manufacturing systems. Flexible Services and Manufacturing Journal, 1st round of reviews ongoing.

**Conference presentations**

- 32nd International Conference on Flexible Automation and Intelligent Manufacturing (FAIM), Porto, Portugal (2023)
- 1st Operator 4.0 Symposium, Veszprèm, Hungary (2023)
- XXVII Summer school "Francesco Turco", Riviera dei Fiori (Italy), 7-9 settembre 2022
- 55th CIRP Conference on Manufacturing Systems, Lugano, Switzerland (2022)
- 14th IFAC Workshop on Intelligent Manufacturing Systems (IMS), Online (2022)
- 11th Conference on Learning Factories, Online (2021)

**Visiting scholar at University of Twente**

Development of a cyber-physical system to monitor human-centric reconfigurable manufacturing systems opertions (Supervisors: Prof. Sebastian Thiede & Dr. P. Ghafoorpoor Yazdi).

**Teaching activities**

Teaching assistant for the Master Course in Management and Industrial Systems Engineering of Digital production and Logistic Systems for three accademic years, from 2021-22 to 2023-24.

**Fundings**

The visiting period at the University of Twente has been partially funded by the SMART-ER seeds SPA1 of the ECIU consortium.

## Chapter 7

# Conclusions

"Maybe I just wanna fly
Wanna live I don't wanna die
Maybe I just wanna breathe
Maybe I just don't believe"
*– Oasis, Live Forever, 1994*

This thesis explores and further remarks on the importance of developing data-driven solutions to monitor industrial operations in human-centric environments. In this regard, multiple CPS has been tested and validated to fill several gaps in the scientific literature demonstrating that it is feasible to take into account sustainability drivers while ensuring the desired rate of in-plant efficiency. This closing discussion pinpoints how these digital solutions answer the research questions conceptualized in Chapter 1 (e.g., RQ in the bullet point).

- *RQ1 – How can cyber-physical systems powered by Real Time Locating Systems and machine learning algorithms digitize human-centric processes executions?*

  RTLS are distinguished by notable performances in locating industrial assets during process executions. Although indoor positions enhance the visibility of operations, these raw data fall short of providing decision-makers with multidimensional metrics to monitor and eventually optimize industrial environments. Indeed, the reviewed RTLS-driven investigations leverage assets' positioning information combined with process metadata (e.g.,

storage area location) with algorithms. However, these contributions are distinguished by two notable limitations as already pointed out in Chapter 1. In short, the cyber layers performances are not investigated and they solely focus on efficiency, neglecting sustainability drivers. The three presented CPS offers a reliable path to trigger multidimensional process monitoring in human-centric manufacturing systems. These intelligent systems digitize the human factor and are validated in both logistic and production environments with peculiar process configurations. Besides the RTLS flexibility and metrological reliability, ML-based algorithms turns out as the best computational method to detect process interactions with strategic industrial assets (e.g., shelves, machines, etc.). This thesis leverages both supervised and unsupervised approaches. On the one hand, the Industrial DB scan fills the limitations of its standard formulation and cluster worker positions to identify HPIs. This novel learning algorithm is firstly defined to monitor human-centric job shops (see Chapter 2) and afterward validated in RMS and warehousing systems. Chapter 4 demonstrates the fast deployment of this method because its performance validation in detecting forklift interactions can avoid the time-consuming process of labeling ground truth data. On the other hand, the LSTM-based neural network proposed in [20] is benchmarked with the Industrial DB scan to monitor HPIs in human-centric RMS (see Chapter 3). Also, the digital monitoring of RMS proves ML algorithms' modularity and flexibility structure. These features accommodate different industrial environments configurations while avoiding time-consuming retraining and/or fine-tuning processes. The returned HPIs are embedded into DSS and dashboard where specific callback functions compute strategic metrics metrics to monitor the operations of these environments. The value added of these multicriteria variables is discussed while addressing the last research question (e.g., RQ3).

- *RQ2 – How can digital ergonomic assessment safeguard workers' physical resilience?*
  A recurrent item of discussion of this thesis pinpoints the importance of digitizing manual operations in human-centric environments, according to Industry 4.0 principles. This paradigm shift replaces conventional managerial approaches based on manager experience and commitment. Besides time-consuming processes analysis, variable manufacturing configurations and process designs affects the validity of such investigations. Ergonomic indices represent a stark example of the digital transformation of manufacturing operations. In recent years, several contributions have leveraged CPS to digitize ergonomic checklists and screening tools. However, the vast majority of these solutions consider a limited set of features to evaluate the physical resilience of workers during task executions (see section 1.3 and Tab. 1.2). The EAWS widely used in the (German) automotive sector is the most complete

one focusing on a heterogeneous set of parameters ranging from body postures to exerted forces. Chapter 5 fills the limitations of reviewed scientific literature and proposes a CPS that following a Pareto approach automates the EAWS assessment. In this regard, the lowest number of sensors was used to digitize as much as possible the ergonomic tool sections. While the RFID-based smart glove identifies HPIs to segment workers' activities, a network of MOCAP cameras and a four-channel sEMG-based wearable monitor working postures and exerted forces, respectively. These measurements are fed into computational algorithms to digitize the Whole Body sections of the EAWS, namely Basic Postures, Action Forces, and Manual Material Handling. This data-driven system is distinguished by two strategic strengths. First, the synergy between the IoT enabling technologies and algorithms can trigger ergonomic investigations in whichever assembly process. This activity insensitiveness facilitates decision-making processes in variable production environments with high rotating product batches. Second, this CPS analyzes ergonomic weaknesses for diversified workforces. The obtained KRIs flow into a time-dependent ergonomic DSS that offers valuable insight to operations managers under different perspectives following a top-down approach. The managerial insights of these risk-oriented metrics are discussed in the next research question (e.g., RQ3).

- *RQ3 – How can key performance and risk indicators be exploited to monitor the operations of industrial environments?*

  IoT acquisition layers and computational algorithms are a necessary conditions to embrace a digital transformation of industrial operations. However, these cyber-physical entities do not represent a sufficient condition to monitor human-centric environments. DSS or dashboards are required to facilitate managers' decision-making processes. In this regard, all four CPS embedd this final layer to close the monitoring loop of industrial environments. The discussed managerial insights provide accurate and targeted information on systems' status as well as hints to eventually optimize manufacturing systems design. To better analyze these implications, it is beneficial to separate into two different sets the validated CPS.
  On the one hand, the RTLS-oriented investigations present two complementary viewpoints to evaluate industries' operations (see Chapters 2, 3 and 4). These solutions demonstrate that indoor positioning data leveraged by ML algorithms can derive KPIs to monitor the efficiency and sustainability of human-centered manufacturing systems. The digital dashboard of Chapter 2 segments the activities of workers highlighting the different production routines of monitored workers. In detail, the operator 2 spends the 44% of his/her working time performing deburring operations while the percentages of the other operator are fairly balanced among the industrial resources.

The activity segmentation evaluates the resources utilization ratio as well, where the deburring workbench registers the highest statistics accounting for 55.9%. At the same time, the investigation into P/D activities suggests a weak material allocation in storage areas. Indeed, worker 2 travels from sub-area 1 to the defined SKUs 2.2 times the meters of worker 1, resulting in a source of inefficiency and social unfairness. A similar take is offered by the DSS in Chapter 3. Besides pointing out the utilization ratio of WS, the distribution of value-added operations suggests that the third operator is the least involved in the production process. Overallocations of workers are detrimental to in-plant performances, especially in scenarios with interconnected job shops. Similarly, the investigation on WS interdependencies highlights that the RMS should improve its social inclusiveness. In particular, the fourth operator is in charge of the vast majority of logistic activities leading to increased travelling times compared to his/her colleagues. Finally, Chapter 4 combines efficiency investigations with the environmental drivers. While the amount of value-added operations (e.g., P/D) and the OEE suggest that the last forklift (e.g., FL05) is the least exploited, the comparison between time spent in activity-driven areas with the duration in performing the operations itself highlights the compelling need to better schedule activities during the order management and eventually a better material allocation in storage areas. This last aspect contributes to reducing the electric consumption of vehicles and reducing operating costs but most importantly the carbon footprint of this logistic environment.
On the other hand, the EAWS-driven KRIs demonstrate the capability of the digital solution to recognize the most risk-prone activities in the manufacturing sequence (see Chapter 5). The CPS highlights process weaknesses based on a wide spectrum of parameters. First, it identifies postures that may exert significant strain on the operators' musculoskeletal system. Second, a muscle-specific assessment of exerted forces points out the most stressed muscular group in assembly activities. Third, the system seamlessly detects time windows when operators perform MMH activities, providing insights into both muscular stress and body postures and reconstructing. Most importantly, these KRIs are activity-driven and thus offer a strategic level of detail for process redesigns. This feature is combined with a traffic light-based system that intuitively suggests the intensity of risk. Therefore, different reconfiguration actions may be implemented. For instance, low repetitive scenarios with considerable risk could be addressed with lean approaches such as visual management. On the contrary, increasing the frequency rate at the same risk intensity may require structural changes. For instance, lowering the workload of operators might involve better line balancing using heuristic problems and/or the introduction of automation (e.g., robotic arms) to

safeguard workforce stamina over time.

## Further research opportunities

The discussed digital solutions yield significant advances in the development of CPS to digitize industrial operations. These improvements target both the design of cyber layers to derive insightful KRIs and KPIs as well as automate the development of conventional managerial tools such as the EAWS. Most importantly, RTLS-driven investigations prove it is possible to achieve the desired rate of in-plant productivity while considering sustainability drivers, according to Industry 5.0 principles. However, improvements are always possible to further refine the proposed methodologies. I hope this final paragraph will inspire researchers to advance the development of CPS in human-centric environments as well as be a good reminder if I will investigate these exciting topics in the future.
A first potential improvement is to design human digital twin and thus scale in real-time or close to the operative functioning of cyber layers. This different time resolution combined with early warning drastically reduces the impact of bottlenecks or more in general operational disruption and hazardous events on process efficiency and workers' well-being. Interested readers may appreciate more details on this approch in [154]. An additional upgrade is to bundle optimization approaches (e.g., heuristic-based) with the existing monitoring modules. In this regard, these CPS would be capable of suggesting the sub-optimal or even optimal process reconfiguration for efficiency and sustainability drivers. This algorithm-oriented discussion can be enhanced by the introduction of additional IoT measurements. For instance, proximity-based technologies can upgrade the solutions presented in Chapters 2 and 4. RFID-based sensors could provide additional information on P/D activities and especially identify carried weight in MMH. In logistic environments, these datastreams can automate the stock managment and increase the productivity of warehousing systems operations. At the same time, workers may wear additional IMUs and/or WS-specific MOCAP cameras to better classify value-added activities in static manual tasks of human-centric RMS (see Chapter 3). Similarly, additional measurands are required to digitize the fourth EAWS section, namely upper limbs load in repetitive tasks (see Chapter 5).

# *Acknowledgements*

It is one of the biggest pleasures to close this work unconventionally. This thesis is fragmented. Readers are encouraged to reconstruct this natural fragmentation in an ecosystem of scientific investigation practices and knowledge. What has been researched and eventually published is part of a mosaic that constitutes a necessary condition for exploring the unknown. In addition to these scientific influences, this work is surrounded and thus affected by permeating social and cultural drivers that exacerbate fragmentation. The not written is present as implicit conditions and part of inclusion, exclusion, and control dynamics[1].

Along such a steep road, academia provides state-of-the-art equipment and facilities as a lantern to propel scientific novelty. This constant search might be a function of metaphysical thinking. Such abstract process tends to attribute to external factors the raison d'être and thus the scientific impact of some contributions. Transposing this concept to society's values in encoding relationships with the world, ourselves, and society, it produces arbitrary fictions necessary for human beings to make life easier for themselves[2]. At the same time, these high degrees of freedom in the liquid post-modern era enable individuals to explore scenario-based creative ethical solutions and promote inclusion, mutual respect, and progress[3].

To conclude, it is my moral duty to thank all double-minded human beings[4] that shared these years and facilitated such investigations by sharing knowledge, pieces of advice and foremost time and empathy. Nothing was taken for granted, and I hope to have shown you the right appreciation. This work is also yours. You will not be forgotten.

♦♦♦

[1] Michel Foucault, *L'Archéologie du savoir* (Paris: Gallimard, 1969).
[2] Friedrich Nietzsche, *Die fröhliche Wissenschaft*, Chemnitz: Ernst Schmeitzner, 1882.
[3] Zygmunt Bauman, *Postmodern Ethics*, Cambridge: Blackwell, 1993.
[4] Simon Baron-Cohen, *Zero Degrees of Empathy*, Penguin Books, 2012.

# Appendix A

This appendix provides additional information on the CPS developed to monitor operations in RMS (see Chapter 3).

**ML-based cyber layer hyper-parameters**

The following table list the relevant sets of hyper-parameters to be optimized during the reconfiguration and operation-oriented computations (see subsubsection 3.1.2 and 3.1.2).

TABLE A1: LSTM hyper-parameters

| Parameter | Value |
|---|---|
| Window Size | 50,128,256 |
| Layer | 1,2 |
| Hidden Size | 100,128,256 |
| Learning Rate | $1e^{-2}$,$1e^{-3}$,$1e^{-4}$ |
| Batch Size | 64,128 |
| Dropout | 0,0.3,0.5 |

TABLE A2: Industrial DBSCAN hyper-parameters

| Parameter | Value |
|---|---|
| $\epsilon$ | [0.1, 0.6] meters |
| NPts | [10, 100] points |
| $\delta$t | [10 100]Hz |
| $\alpha$ | [1, 10] second |
| $\beta$ | [0.1, 2] meters |
| $\phi$ | [0.1, 2] meters |

TABLE A3: Random Forest hyper-parameters

| Parameter | Value |
|---|---|
| Estimators number | 50,70,100,150 |
| Criterion | Gini, Entropy |
| Maximum Features | sqrt, log2 |
| Minimum sample split | 2,3,4 |

TABLE A4: Gaussian Support Vector hyper-parameters

| Parameter | Value |
|---|---|
| C | 1, 10, 100, 1000 |
| $\gamma$ | 0.001 , 0.01, 0.1, 1,10 |

TABLE A5: Gradient Boosting hyper-parameters

| Parameter | Value |
|---|---|
| Estimators number | 50,70,100,150 |
| Loss | Logarithmic |
| Learning rate | $1e^{-1}$,$1e^{-2}$,$1e^{-3}$ |
| Maximum Features | sqrt, log2 |
| Minimum sample split | 2,3,4 |

**Production setups & dataset**

These tables provide additional insights related to production setups. In particular, the 2D indoor positions of WS and the dimension of the feature-engineered workers' motion pattern are highlighted.

TABLE A6: Absolute positions of industrial resources in different production setups

| | | WS1 | | WS2 | | WS3 | | WS4 | | WS5 | | Robot | |
|---|---|---|---|---|---|---|---|---|---|---|---|---|---|
| Setup | Workers | X | Y | X | Y | X | Y | X | Y | X | Y | X | Y |
| 1 | 6 | 4.57 | 3.35 | 4.43 | 1.22 | 6.76 | 4.13 | 6.56 | 2.34 | 6.23 | 1.03 | 6.37 | 3.12 |
| 2 | 6 | 4.40 | 2.79 | 6.23 | 4.29 | 6.17 | 1.39 | 4.7 | 5.12 | 9.82 | 3.26 | 8.44 | 3.36 |
| 3 | 5 | 8.20 | 3.27 | 6.35 | 3.96 | 6.63 | 1.84 | 4.94 | 1.06 | 4.29 | 1.73 | 4.05 | 3.08 |
| 4 | 4 | 5.00 | 3.11 | 6.24 | 4.23 | 6.10 | 2.03 | 4.51 | 5.21 | 8.87 | 3.61 | 9.01 | 1.86 |
| 5 | 5 | 4.50 | 3.31 | 4.32 | 1.29 | 6.23 | 4.51 | 5.85 | 2.08 | 8.25 | 3.77 | 8.04 | 1.75 |
| 6 | 4 | 4.57 | 3.35 | 4.43 | 1.22 | 6.76 | 4.13 | 6.56 | 2.34 | 6.23 | 1.03 | 6.37 | 3.12 |
| **7** | **5** | **4.75** | **0.91** | **4.30** | **3.61** | **7.34** | **4.25** | **5.97** | **3.82** | **4.78** | **5.07** | **6.30** | **5.70** |
| 8 | 6 | 4.53 | 3.37 | 6.13 | 2.46 | 6.34 | 4.21 | 4.56 | 0.88 | 8.72 | 3.19 | 7.98 | 3.42 |

TABLE A7: Operator-based dataset dimension

| Operator | Number of input data |
|---|---|
| 1 | 92435 |
| 2 | 94147 |
| 3 | 99320 |
| 4 | 90947 |
| 5 | 68380 |
| 6 | 27118 |

**ML-based cyber layer performances**

These illustrations details the confusion matrices related to the best classifiers for the operation-oriented computations' binary classification (e.g., working in a WS and Idle state). Then, a bullet point lists the grid-search optimized set of hyper-parameters.

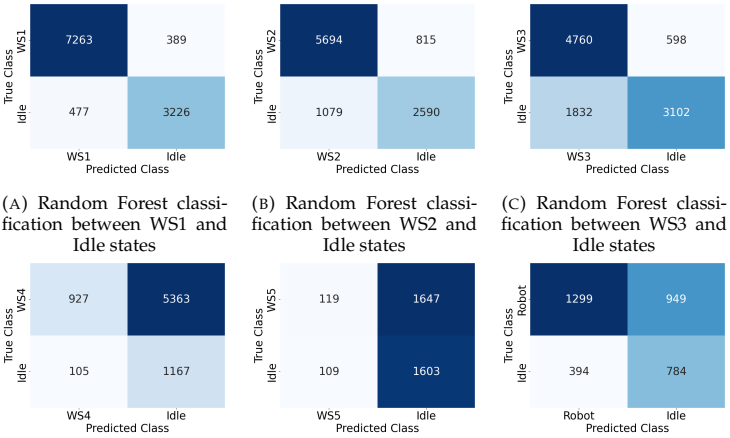


(A) Random Forest classification between WS1 and Idle states

(B) Random Forest classification between WS2 and Idle states

(C) Random Forest classification between WS3 and Idle states

(D) Gradient Boosting classification between WS4 and Idle states

(E) Gradient Boosting classification between WS5 and Idle states

(F) Gradient Boosting classification between Robot and Idle states

FIGURE A1: Confusion matrices of the best performing classifiers for the operation oriented computations

- **Support Vector Machine:**
  - C: 1
  - $\gamma$: 0.001
- **Random Forest:**
  - Estimators number: 70
  - Criterion: *entropy*
  - Maximum Features: *sqtr*
  - Minimum sample split: 3
- **Gradient Boosting:**
  - Estimators number: 100
  - Learning rate: $1e^{-}1$
  - Maximum Features: *sqrt*
  - Minimum sample split: 2

# Appendix B

This Appendix details the body joint to evaluate workers' body postures as well as the sequence of activities performed by the operator during the assembly of the dresser. At the beginning of each Task, the operator retrieves the necessary components from the supermarket, as illustrated in Figure B1. The tools are already conveniently positioned on the table of the workstation.

**Task ID - Assembly Process Activities**

- **Task 1 - Mounting Plastic Plates**: Collect screws and plastic plates, and place them on the worktable. Retrieve two wooden panels (i.e., the sides of the dresser) from under the table and place them on top. Position the sliding plates on the wooden panels and secure them with screws using a Phillips screwdriver, as indicated in Figure B2 (a). Move the panels aside to make space on the table.
- **Task 2 - Mounting Bracket L**: Collect L-brackets and fastening screws, and place them on the worktable. Retrieve a third wooden panel (i.e., the back of the dresser) from under the table and place it on top. Position the L-brackets on the wooden panel and secure them with screws using a Phillips screwdriver, as indicated in Figure B2 (b).
- **Task 3 - Inserting Wooden Dowels**: Collect wooden dowels and stand in front of the worktable. Manually insert the dowels into the sides of the back panel of the dresser as indicated in Figure B2 (c).
- **Task 4 - Tightening Black Screws**: Collect black screws and place them on the worktable. Retrieve two wooden panels (i.e., a side and the back of the dresser) and align them. Secure the two parts with black screws using a hexagonal Allen key as depicted in Figure B2 (d). Move the semi-assembled piece aside to make space on the table.
- **Task 5 - Inserting Wooden Dowels**: Collect additional wooden dowels and place them on the worktable. Retrieve two thin wooden panels (i.e., the supports of the dresser) from under the table and place them on top. Manually

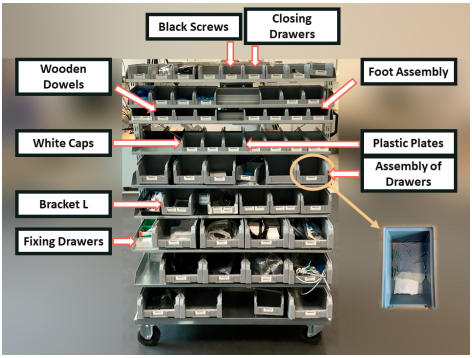


FIGURE B1: Layout of the supermarket showing the locations of components required for the different assembly tasks.

insert the wooden dowels into the indicated spots as in Figure B2 (e) and move the supports aside to make space on the table.

- **Task 6 - Tightening Black Screws**: Collect more black screws and place them on the worktable. Bring the semi-assembled piece and the two support panels closer, fitting the pieces one at a time. Secure the various parts with black screws using a hexagonal Allen key. Align the remaining wooden panel (i.e., the other side of the dresser) with the semi-assembled piece and secure it with black screws using a hexagonal Allen key (see Figure B2 (f)).
- **Task 7 - Foot Assembly**: Collect the specific nails and place them on the worktable. Lift, turn, and move the semi-assembled dresser to the floor to secure the nails with a hammer (see Figure B2 (g)). Turn and reposition the dresser upright on the floor.
- **Task 8 - Assembly of Drawer (1)**: Collect appropriate screws and place them on the worktable. Retrieve a thin wooden panel (i.e., the outer face of the drawer) from under the table and place it on top. Secure the screws with a Phillips screwdriver in the spots indicated in Figure B2 (h) to allow the insertion of the drawer's side panels.
- **Task 9 - Inserting Wooden Dowels (1)**: Collect additional wooden dowels and place them on the worktable. Retrieve two thin wooden panels (i.e., the sides of the drawer) from under the table and place them on top. Manually insert the dowels into the appropriate spots and slide the drawer's side panels onto the previously screwed front panel as in Figure B2 (i).
- **Task 10 - Fixing Drawer (1)**: Collect appropriate screws and insert them into the drawer's side panels using a slotted screwdriver, securing them to the previously prepared front panel (see Figure B2 (j)). Retrieve the drawer base

and back panel, slide the base into the slots inside, and fit the back panel into the free part of the base.

- **Task 11 - Closing Drawer (1)**: Collect specific nails and secure the drawer back with a hammer, fitting the side panels with the closing panel as indicated in Figure B2 (k).
- **Task 12 - Mounting White Caps (1)**: Collect white screws and manually insert them into the drawer's side panels without fully securing them. Move the drawer to the adjacent worktable to make space on the main table.
- **Task 13 - Assembly of Drawer (2)**: Repeat the same steps as Task 8 for the second drawer.
- **Task 14 - Inserting Wooden Dowels (2)**: Repeat the same steps as Task 9 for the second drawer.
- **Task 15 - Fixing Drawer (2)**: Repeat the same steps as Task 10 for the second drawer.
- **Task 16 - Closing Drawer (2)**: Repeat the same steps as Task 11 for the second drawer.
- **Task 17 - Mounting White Caps (2)**: Repeat the same steps as Task 12 for the second drawer.
- **Task 18 - Assembly of Drawer (3)**: Repeat the same steps as Task 8 for the third drawer.
- **Task 19 - Inserting Wooden Dowels (3)**: Repeat the same steps as Task 9 for the third drawer.
- **Task 20 - Fixing Drawer (3)**: Repeat the same steps as Task 10 for the third drawer.
- **Task 21 - Closing Drawer (3)**: Repeat the same steps as Task 11 for the third drawer.
- **Task 22 - Mounting White Caps (3)**: Collect white screws and manually insert them into the third drawer's side panels without fully securing them. Retrieve the two previously assembled drawers from the adjacent worktable and place them inside the dresser (see Figure B2 (l)). Secure the already inserted drawers in the dresser using a slotted screwdriver, then secure the white screws on the last drawer. Insert the last drawer into the dresser, completing the assembly process. *Note*: Securing all the drawers at the end optimizes tool usage. Securing two drawers inside and one on the table is for the operator's convenience.

(A) Task 1

(B) Task 2

(C) Task 3

(D) Task 4

(E) Task 5

(F) Task 6

(G) Task 7

(H) Task 8

(I) Task 9

(J) Task 10

(K) Task 11

(L) Task 22

(M) Tools

FIGURE B2: Visual representation of assembly tasks, showcasing the operator's interactions with components and tools at different stages.

TABLE B1: Posture-dependent body joints.

| **Posture** | **Body Joint Group** | **Number** |
|---|---|---|
| Walking | Pelvis | 1 |
| Standing | Back | 1, 2, 3, 4 |
| | Leg (R) | 1, 23, 24, 25 |
| | Leg (L) | 1, 19, 20, 21 |
| Low Bending ($20 - 60°$) | Back | 1, 2, 3, 4 |
| | Leg (R) | 1, 23, 24, 25 |
| | Leg (L) | 1, 19, 20, 21 |
| High Bending ($> 60°$) | Back | 1, 2, 3, 4 |
| | Leg (R) | 1, 23, 24, 25 |
| | Leg (L) | 1, 19, 20, 21 |
| Elbows Above Shoulders | Back | 1, 2, 3, 4 |
| | Arm (R) | 12, 13, 14, 15 |
| | Arm (L) | 5, 6, 7, 8 |
| Hands Above Head | Back | 1, 2, 3, 4 |
| | Arm (R) | 12, 13, 14, 15 |
| | Arm (L) | 5, 6, 7, 8 |
| Upright (Kneeling) | Back | 1, 2, 3, 4 |
| | Knee (R) | 23, 24 |
| | Knee (L) | 19, 20 |
| | Ankle (R) | 24, 25 |
| | Ankle (L) | 20, 21 |
| Bent Forward (Kneeling) | Back | 1, 2, 3, 4 |
| | Knee (R) | 23, 24 |
| | Knee (L) | 19, 20 |
| | Ankle (R) | 24, 25 |
| | Ankle (L) | 20, 21 |
| Elbows Above Shoulders (Kneeling) | Knee (R) | 23, 24 |
| | Knee (L) | 19, 20 |
| | Ankle (R) | 24, 25 |
| | Ankle (L) | 20, 21 |
| | Arm (R) | 12, 13, 14, 15 |
| | Arm (L) | 5, 6, 7, 8 |
| Trunk Rotation (Asymmetric) | Spine Naval, Hips | 2, 19, 23 |
| | Spine Chest, Shoulders | 3, 6, 13 |
| Lateral Bending (Asymmetric) | Back | 1, 2, 3, 4 |
| | Hip (R) | 1, 23 |
| Far Reach (Asymmetric) | Arm (R) | 12, 13, 14, 15 |
| | Arm (L) | 5, 6, 7, 8 |

# Bibliography


[1] Sin-Moh Cheah and Helene Leong. "Relevance of CDIO to industry 4.0–proposal for 2 new standards". In: (2018).

[2] European Commission et al. *Enabling Technologies for Industry 5.0 : results of a workshop with Europe's technology leaders*. Publications Office, 2020.

[3] Bartlomiej Gladysz et al. "Current development on the Operator 4.0 and transition towards the Operator 5.0: A systematic literature review in light of Industry 5.0". In: *Journal of Manufacturing Systems* 70 (2023), pp. 160–185.

[4] Tuan-Anh Tran, Tamás Ruppert, and János Abonyi. "Indoor positioning systems can revolutionise digital lean". In: *Applied Sciences* 11.11 (2021), p. 5291.

[5] Mangesh Joshi and Vishwas Deshpande. "A systematic review of comparative studies on ergonomic assessment techniques". In: *International Journal of Industrial Ergonomics* 74 (2019), p. 102865.

[6] Marco Bortolini et al. "Automatic assessment of the ergonomic risk for manual manufacturing and assembly activities through optical motion capture technology". In: *Procedia CIRP* 72 (2018), pp. 81–86.

[7] Elena G Popkova, Yulia V Ragulina, and Aleksei V Bogoviz. "Fundamental differences of transition to industry 4.0 from previous industrial revolutions". In: *Industry 4.0: Industrial revolution of the 21st century* (2019), pp. 21–29.

[8] Elena G Popkova, Yulia V Ragulina, and Aleksei V Bogoviz. *Industry 4.0: Industrial revolution of the 21st century*. Vol. 169. Springer, 2019.

[9] Francisco Almada-Lobo. "The Industry 4.0 revolution and the future of Manufacturing Execution Systems (MES)". In: *Journal of innovation management* 3.4 (2015), pp. 16–21.

[10] Olivier Cardin. "Classification of cyber-physical production systems applications: Proposition of an analysis framework". In: *Computers in Industry* 104 (2019), pp. 11–21.

[11] Sebastian Thiede, Max Juraschek, and Christoph Herrmann. "Implementing cyber-physical production systems in learning factories". In: *Procedia Cirp* 54 (2016), pp. 7–12.

[12] László Monostori. "Cyber-physical production systems: Roots, expectations and R&D challenges". In: *Procedia Cirp* 17 (2014), pp. 9–13.

[13] Thomas H-J Uhlemann, Christian Lehmann, and Rolf Steinhilper. "The digital twin: Realizing the cyber-physical production system for industry 4.0". In: *Procedia Cirp* 61 (2017), pp. 335–340.

[14] Sebastian Thiede. "Cyber physical production systems and their role for decarbonization of industry". In: (2022), pp. 75–86.

[15] Tahera Kalsoom et al. "Impact of IOT on Manufacturing Industry 4.0: A new triangular systematic review". In: *Sustainability* 13.22 (2021), p. 12506.

[16] Dimitris Mourtzis, Ekaterini Vlachou, and NJPC Milas. "Industrial big data as a result of IoT adoption in manufacturing". In: *Procedia cirp* 55 (2016), pp. 290–295.

[17] Margherita Peruzzini, Fabio Grandi, and Marcello Pellicciari. "Exploring the potential of Operator 4.0 interface and monitoring". In: *Computers & Industrial Engineering* 139 (2020), p. 105600.

[18] David Romero, Johan Stahre, and Marco Taisch. *The Operator 4.0: Towards socially sustainable factories of the future*. 2020.

[19] David Romero et al. "Towards an operator 4.0 typology: a human-centric perspective on the fourth industrial revolution technologies". In: *proceedings of the international conference on computers and industrial engineering (CIE46), Tianjin, China*. 2016, pp. 29–31.

[20] Francesco Pilati et al. "An Artificial Neural Network Architecture to Classify Workers' Operations in Manual Production Processes".

In: *International Conference on Flexible Automation and Intelligent Manufacturing*. Springer. 2023, pp. 805–812.

[21] Jim Davis et al. "Smart manufacturing". In: *Annual review of chemical and biomolecular engineering* 6.1 (2015), pp. 141–160.

[22] Thorsten Wuest et al. "Machine learning in manufacturing: advantages, challenges, and applications". In: *Production & Manufacturing Research* 4.1 (2016), pp. 23–45.

[23] Andrea Albanese et al. "Tiny machine learning for high accuracy product quality inspection". In: *IEEE Sensors Journal* 23.2 (2022), pp. 1575–1583.

[24] Siby Jose Plathottam et al. "A review of artificial intelligence applications in manufacturing operations". In: *Journal of Advanced Manufacturing and Processing* 5.3 (2023), e10159.

[25] Sotiris B Kotsiantis, Ioannis Zaharakis, P Pintelas, et al. "Supervised machine learning: A review of classification techniques". In: *Emerging artificial intelligence applications in computer engineering* 160.1 (2007), pp. 3–24.

[26] Francesco Pilati and Andrea Sbaragli. "Learning human-process interaction in manual manufacturing job shops through indoor positioning systems". In: *Computers in Industry* 151 (2023), p. 103984.

[27] Francesco Pilati et al. "Goal-oriented clustering algorithm to monitor the efficiency of logistic processes through real-time locating systems". In: *International Journal of Computer Integrated Manufacturing* (2024), pp. 1–17.

[28] Shaohua Huang et al. "A weighted fuzzy C-means clustering method with density peak for anomaly detection in IoT-enabled manufacturing process". In: *Journal of Intelligent Manufacturing* 32 (2021), pp. 1845–1861.

[29] Yuchen Jiang et al. "A2-LSTM for predictive maintenance of industrial equipment based on machine learning". In: *Computers & Industrial Engineering* 172 (2022), p. 108560.

[30] Lars Köttner et al. "Process monitoring using machine learning for semi-automatic drilling of rivet holes in the aerospace industry". In: *Production at the leading edge of technology: Proceedings of the 10th*

*Congress of the German Academic Association for Production Technology (WGP), Dresden, 23-24 September 2020*. Springer. 2021, pp. 497–507.

[31] Nicholas Jeffrey, Qing Tan, and José R Villar. "Using Ensemble Learning for Anomaly Detection in Cyber–Physical Systems". In: *Electronics* 13.7 (2024), p. 1391.

[32] Sebastian Thiede. "Cyber physical production systems and their role for decarbonization of industry". In: *Intelligent Decarbonisation: Can Artificial Intelligence and Cyber-Physical Systems Help Achieve Climate Mitigation Targets?* Springer, 2022, pp. 75–86.

[33] Enrico Cagno and Andrea Trianni. "Exploring drivers for energy efficiency within small-and medium-sized enterprises: First evidences from Italian manufacturing enterprises". In: *Applied Energy* 104 (2013), pp. 276–285.

[34] Francesco Pilati et al. "Operator 5.0: Enhancing the Physical Resilience of Workers in Assembly Lines". In: *2023 IEEE International Workshop on Metrology for Industry 4.0 & IoT (MetroInd4. 0&IoT)*. IEEE. 2023, pp. 177–182.

[35] Christian Bechinie et al. "Toward human-centered intelligent assistance system in manufacturing: challenges and potentials for operator 5.0". In: *Procedia Computer Science* 232 (2024), pp. 1584–1596.

[36] David Romero and Johan Stahre. "Towards the resilient operator 5.0: The future of work in smart resilient manufacturing systems". In: *Procedia cirp* 104 (2021), pp. 1089–1094.

[37] Duygu Ersol and Nilgun Fescioglu-Unver. "Heuristic policies for mobile asset sharing within hospitals". In: *Computers & Industrial Engineering* 111 (2017), pp. 352–363.

[38] Yunze Zeng, Parth H Pathak, and Prasant Mohapatra. "Analyzing shopper's behavior through wifi signals". In: *Proceedings of the 2nd workshop on Workshop on Physical Analytics*. 2015, pp. 13–18.

[39] Zhiheng Zhao et al. "Digital twin-enabled dynamic spatial-temporal knowledge graph for production logistics resource allocation". In: *Computers & Industrial Engineering* 171 (2022), p. 108454.

[40] Changwei Miao et al. “Path planning optimization of indoor mobile robot based on adaptive ant colony algorithm”. In: *Computers & Industrial Engineering* 156 (2021), p. 107230.

[41] Matthias Wolf et al. “Real time locating systems for human centered production planning and monitoring”. In: *IFAC-PapersOnLine* 55.2 (2022), pp. 366–371.

[42] Faheem Zafari, Athanasios Gkelias, and Kin K Leung. “A survey of indoor localization systems and technologies”. In: *IEEE Communications Surveys & Tutorials* 21.3 (2019), pp. 2568–2599.

[43] Fazeelat Mazhar, Muhammad Gufran Khan, and Benny Sällberg. “Precise indoor positioning using UWB: A review of methods, algorithms and implementations”. In: *Wireless Personal Communications* 97.3 (2017), pp. 4467–4491.

[44] Noor Abdul Khaleq Zghair, Muayad Sadik Croock, and Ali Abdul Razzaq Taresh. “Indoor localization system using Wi-Fi technology”. In: *Iraqi J. Comput. Commun. Control Syst. Eng.* 19.2 (2019), pp. 69–77.

[45] Cung Lian Sang et al. “An analytical study of time of flight error estimation in two-way ranging methods”. In: *2018 International Conference on Indoor Positioning and Indoor Navigation (IPIN)*. IEEE. 2018, pp. 1–8.

[46] Yun Cheng and Taoyun Zhou. “UWB indoor positioning algorithm based on TDOA technology”. In: *2019 10th international conference on information technology in medicine and education (ITME)*. IEEE. 2019, pp. 777–782.

[47] Luca Santoro et al. “Scale up to infinity: The UWB indoor global positioning system”. In: (2021), pp. 1–8.

[48] András Rácz-Szabó et al. “Real-time locating system in production management”. In: *Sensors* 20.23 (2020), p. 6766.

[49] Brendan P Sullivan et al. “Digital value stream mapping: Application of UWB real time location systems”. In: *Procedia CIRP* 107 (2022), pp. 1186–1191.

[50] Poorya Ghafoorpoor Yazdi et al. “Cyber Physical System for Reconfigurable Learning Factories: Combining 3D Simulations, Reconfigurable Layouts and Real-Time Locating Systems”. In: *Conference on Learning Factories*. Springer. 2024, pp. 28–35.

[51] Juraj Slovák et al. “RTLS tracking of material flow in order to reveal weak spots in production process”. In: *2019 22nd International Conference on Process Control (PC19)*. IEEE. 2019, pp. 234–238.

[52] Thomas Kelepouris and Duncan McFarlane. “Determining the value of asset location information systems in a manufacturing environment”. In: *International Journal of Production Economics* 126.2 (2010), pp. 324–334.

[53] András Darányi et al. “Processing indoor positioning data by goal-oriented supervised fuzzy clustering for tool management”. In: *Journal of Manufacturing Systems* 63 (2022), pp. 15–22.

[54] Csaba Hegedűs, Attila Frankó, and Pál Varga. “Asset and production tracking through value chains for Industry 4.0 using the arrowhead framework”. In: *2019 IEEE International Conference on Industrial Cyber Physical Systems (ICPS)*. IEEE. 2019, pp. 655–660.

[55] Bartlomiej Gladysz, Krzysztof Santarek, and Cezary Lysiak. “Dynamic spaghetti diagrams. A case study of pilot RTLS implementation”. In: *Intelligent Systems in Production Engineering and Maintenance–ISPEM 2017: Proceedings of the First International Conference on Intelligent Systems in Production Engineering and Maintenance ISPEM 2017 1*. Springer. 2018, pp. 238–248.

[56] Xiangguo Ma and Tongjuan Liu. “The application of Wi-Fi RTLS in automatic warehouse management system”. In: *2011 IEEE International conference on automation and logistics (ICAL)*. IEEE. 2011, pp. 64–69.

[57] Bence Pallai, Péter Tamás, and Henriett Matyi. “Order Picking System Evaluation Using Rtls Method”. In: *Advanced Logistic Systems-Theory and Practice* 17.1 (2023), pp. 62–70.

[58] Farouq Halawa et al. “Introduction of a real time location system to enhance the warehouse safety and operational efficiency”. In: *International Journal of Production Economics* 224 (2020), p. 107541.

[59] Andreas Löcklin et al. "Trajectory prediction of workers to improve AGV and AMR operation based on the manufacturing schedule". In: *Procedia CIRP* 107 (2022), pp. 283–288.

[60] M Wassell et al. "Electronic health records for predicting outcomes to work-related musculoskeletal disorders: a scoping review". In: *Journal of Occupational Rehabilitation* (2024), pp. 1–13.

[61] Marco Bortolini et al. "Motion Analysis System (MAS) for production and ergonomics assessment in the manufacturing processes". In: *Computers & Industrial Engineering* 139 (2020), p. 105485.

[62] Karlheinz Schaub et al. "The European assembly worksheet". In: *Theoretical Issues in Ergonomics Science* 14.6 (2013), pp. 616–639.

[63] Michael Spitzhirn, Peter Kuhlang, and Angelika C Bullinger. "Digitalization of the Ergonomic Assessment Worksheet–User Requirements for EAWS Digital Evaluation Functions". In: *Proceedings of the 20th Congress of the International Ergonomics Association (IEA 2018) Volume VII: Ergonomics in Design, Design for All, Activity Theories for Work Analysis and Design, Affective Design 20*. Springer. 2019, pp. 272–282.

[64] Chika Edith Mgbemena et al. "Ergonomic evaluation on the manufacturing shop floor: A review of hardware and software technologies". In: *CIRP Journal of Manufacturing Science and Technology* 30 (2020), pp. 68–78.

[65] Mario Caterino, Marta Rinaldi, and Marcello Fera. "Digital ergonomics: an evaluation framework for the ergonomic risk assessment of heterogeneous workers". In: *International Journal of Computer Integrated Manufacturing* 36.2 (2023), pp. 239–259.

[66] Francesco Caputo et al. "Imu-based motion capture wearable system for ergonomic assessment in industrial environment". In: *Advances in Human Factors in Wearable Technologies and Game Design: Proceedings of the AHFE 2018 International Conferences on Human Factors and Wearable Technologies, and Human Factors in Game Design and Virtual Environments, Held on July 21–25, 2018, in Loews Sapphire Falls Resort at Universal Studios, Orlando, Florida, USA 9*. Springer. 2019, pp. 215–225.

[67] Woojoo Kim et al. "Comparison of joint angle measurements from three types of motion capture systems for ergonomic postural assessment". In: *Advances in Physical, Social & Occupational Ergonomics: Proceedings of the AHFE 2020 Virtual Conferences on Physical Ergonomics and Human Factors, Social & Occupational Ergonomics and Cross-Cultural Decision Making, July 16–20, 2020, USA*. Springer. 2020, pp. 3–11.

[68] Yann Desmarais et al. "A review of 3D human pose estimation algorithms for markerless motion capture". In: *Computer Vision and Image Understanding* 212 (2021), p. 103275.

[69] Robert M Kanko et al. "Concurrent assessment of gait kinematics using marker-based and markerless motion capture". In: *Journal of biomechanics* 127 (2021), p. 110665.

[70] Stephen Bao et al. "Force measurement in field ergonomics research and application". In: *International Journal of Industrial Ergonomics* 39.2 (2009), pp. 333–340.

[71] Robert Paulsen et al. "The inter-rater reliability of Strain Index and OCRA Checklist task assessments in cheese processing". In: *Applied ergonomics* 51 (2015), pp. 199–204.

[72] Geoffrey C David. "Ergonomic methods for assessing exposure to risk factors for work-related musculoskeletal disorders". In: *Occupational medicine* 55.3 (2005), pp. 190–199.

[73] Peter Konrad. "The abc of EMG". In: *A practical introduction to kinesiological electromyography* 1 (2005).

[74] Sunisa Chaiklieng and Worawan Poochada. "Assessment of Muscle Fatigue and Potential Health Risk of Low Back Pain Among Call Center Workers". In: *Advances in Physical, Social & Occupational Ergonomics: Proceedings of the AHFE 2021 Virtual Conferences on Physical Ergonomics and Human Factors, Social & Occupational Ergonomics, and Cross-Cultural Decision Making, July 25-29, 2021, USA*. Springer. 2021, pp. 54–61.

[75] Goksu Avdan, Sinan Onal, and Bryan K Smith. "Normalization of EMG Signals: Optimal MVC Positions for the Lower Limb Muscle Groups in Healthy Subjects". In: *Journal of Medical and Biological Engineering* 43.2 (2023), pp. 195–202.

[76] Oluwalogbon O Akinnola, Vasiliki Vardakastani, and Angela E Kedgley. "Identifying tasks to elicit maximum voluntary contraction in the muscles of the forearm". In: *Journal of Electromyography and Kinesiology* 55 (2020), p. 102463.

[77] Camilla Dahlqvist et al. "Comparing two methods to record maximal voluntary contractions and different electrode positions in recordings of forearm extensor muscle activity: Refining risk assessments for work-related wrist disorders". In: *Work* 59.2 (2018), pp. 231–242.

[78] Manikandan Rajendran et al. "Ergonomic evaluation of workers during manual material handling". In: *Materials Today: Proceedings* 46 (2021), pp. 7770–7776.

[79] Indah Pratiwi and Hartanto Hartanto. "Manual material handling analysis of work posture in biomemechanics aspect using key indicator method (KIM) and ergonomic assessment worksheet (EAWS) in barecore workers". In: *AIP Conference Proceedings*. Vol. 2727. 1. AIP Publishing. 2023.

[80] Jindong Wang et al. "Deep learning for sensor-based activity recognition: A survey". In: *Pattern recognition letters* 119 (2019), pp. 3–11.

[81] Hanife Mehmet, Angela WH Yang, and Stephen R Robinson. "Measurement of hand grip strength in the elderly: A scoping review with recommendations". In: *Journal of bodywork and movement therapies* 24.1 (2020), pp. 235–243.

[82] Mahnaz Saremi and Sajjad Rostamzadeh. "Hand dimensions and grip strength: a comparison of manual and non-manual workers". In: *Proceedings of the 20th Congress of the International Ergonomics Association (IEA 2018) Volume IX: Aging, Gender and Work, Anthropometry, Ergonomics for Children and Educational Environments 20*. Springer. 2019, pp. 520–529.

[83] Health. Division of Physical Sciences. *NIOSH, Manual of Analytical Methods*. US Department of Health and Human Services, Public Health Service, Centers …, 1994.

[84] Stover H Snook and Vincent M Ciriello. "The design of manual handling tasks: revised tables of maximum acceptable weights and forces". In: *Ergonomics* 34.9 (1991), pp. 1197–1213.

[85] Sue Hignett and Lynn McAtamney. "Rapid entire body assessment (REBA)". In: *Applied ergonomics* 31.2 (2000), pp. 201–205.

[86] Lynn McAtamney and E Nigel Corlett. "RULA: a survey method for the investigation of work-related upper limb disorders". In: *Applied ergonomics* 24.2 (1993), pp. 91–99.

[87] Enrico Occhipinti. "OCRA: a concise index for the assessment of exposure to repetitive movements of the upper limbs". In: *Ergonomics* 41.9 (1998), pp. 1290–1311.

[88] J Steven Moore and Arun Garg. "The strain index: a proposed method to analyze jobs for risk of distal upper extremity disorders". In: *American Industrial Hygiene Association Journal* 56.5 (1995), pp. 443–458.

[89] Osmo Karhu, Pekka Kansi, and Iikka Kuorinka. "Correcting working postures in industry: A practical method for analysis". In: *Applied ergonomics* 8.4 (1977), pp. 199–201.

[90] Yoram Koren et al. "Reconfigurable manufacturing systems". In: *CIRP annals* 48.2 (1999), pp. 527–540.

[91] Min Zhang et al. "Linking supply chain quality integration with mass customization and product modularity". In: *International journal of production economics* 207 (2019), pp. 227–235.

[92] Nikola Suzić et al. "Implementation guidelines for mass customization: current characteristics and suggestions for improvement". In: *Production Planning & Control* 29.10 (2018), pp. 856–871.

[93] K Shyam Sunder Reddy and C Shoba Bindu. "StreamSW: A density-based approach for clustering data streams over sliding windows". In: *Measurement* 144 (2019), pp. 14–19.

[94] Hailei Zou. "Clustering algorithm and its application in data mining". In: *Wireless Personal Communications* 110.1 (2020), pp. 21–30.

[95] Miklós Mezei et al. "Goal-oriented possibilistic fuzzy C-Medoid clustering of human mobility patterns—Illustrative application for the Taxicab trips-based enrichment of public transport services". In: *Plos one* 17.10 (2022), e0274779.

[96] Longgang Xiang, Meng Gao, and Tao Wu. "Extracting stops from noisy trajectories: A sequence oriented clustering approach". In: *ISPRS International Journal of Geo-Information* 5.3 (2016), p. 29.

[97] Hari Krishna Kanagala and VV Jaya Rama Krishnaiah. "A comparative study of K-Means, DBSCAN and OPTICS". In: *2016 International Conference on Computer Communication and Informatics (ICCCI)*. IEEE. 2016, pp. 1–6.

[98] Harsh Vardhan Singh, Ashwin Girdhar, and Sonika Dahiya. "A Literature survey based on DBSCAN algorithms". In: *2022 6th International Conference on Intelligent Computing and Control Systems (ICICCS)*. IEEE. 2022, pp. 751–758.

[99] Yikai Gong, Richard O Sinnott, and Paul Rimba. "RT-DBSCAN: real-time parallel clustering of spatio-temporal data using spark-streaming". In: *Computational Science–ICCS 2018: 18th International Conference, Wuxi, China, June 11–13, 2018, Proceedings, Part I 18*. Springer. 2018, pp. 524–539.

[100] James Williams et al. "Context for Leisure Walking Routes: A Vision For a Spatial-Platial Approach". In: (2022).

[101] Qorvo. *Decawave DWM1000*. `https://www.decawave.com/product/dwm1000-module/`. Accessed: 2022-09-05. 2022.

[102] Qorvo. *Decawave DWM1001*. `https://www.decawave.com/product/dwm1001-module/`. Accessed: 2022-09-05. 2022.

[103] Luca Santoro et al. "Scalable centimetric tracking system for team sports". In: *2022 IEEE International Workshop on Sport, Technology and Research (STAR)*. IEEE. 2022, pp. 1–6.

[104] Ronald W Schafer. "What is a Savitzky-Golay filter?[lecture notes]". In: *IEEE Signal processing magazine* 28.4 (2011), pp. 111–117.

[105] Long Cheng et al. "Real time indoor positioning system for smart grid based on uwb and artificial intelligence techniques". In: *2020 IEEE Conference on Technologies for Sustainability (SusTech)*. IEEE. 2020, pp. 1–7.

[106] Alessandro Antonucci et al. "Performance assessment of a people tracker for social robots". In: *2019 IEEE International Instrumentation*

*and Measurement Technology Conference (I2MTC)*. IEEE. 2019, pp. 1–6.

[107] Jeff Miller. *Advanced Stochastic Modeling — jwmi.github.io*. `https://jwmi.github.io/ASM/index.html`. Accessed 31-Aug-2022. 2016.

[108] Andrea Albanese, Matteo Nardello, and Davide Brunelli. "Automated pest detection with DNN on the edge for precision agriculture". In: *IEEE Journal on Emerging and Selected Topics in Circuits and Systems* 11.3 (2021), pp. 458–467.

[109] Hsuan-Tien Lin, Chih-Jen Lin, and Ruby C Weng. "A note on Platt's probabilistic outputs for support vector machines". In: *Machine learning* 68.3 (2007), pp. 267–276.

[110] David Romero et al. "The operator 4.0: Human cyber-physical systems & adaptive automation towards human-automation symbiosis work systems". In: *IFIP international conference on advances in production management systems*. Springer. 2016, pp. 677–686.

[111] Abdelkrim R Yelles-Chaouche et al. "Reconfigurable manufacturing systems from an optimisation perspective: a focused review of literature". In: *International Journal of Production Research* 59.21 (2021), pp. 6400–6418.

[112] Faisal Hasan, Pramod Kumar Jain, and Dinesh Kumar. "Service level as performance index for reconfigurable manufacturing system involving multiple part families". In: *Procedia Engineering* 69 (2014), pp. 814–821.

[113] Marco Bortolini, Francesco Gabriele Galizia, and Cristina Mora. "Reconfigurable manufacturing systems: Literature review and research trend". In: *Journal of manufacturing systems* 49 (2018), pp. 93–106.

[114] Mostafa G Mehrabi, A Galip Ulsoy, and Yoram Koren. "Reconfigurable manufacturing systems: Key to future manufacturing". In: *Journal of Intelligent manufacturing* 11 (2000), pp. 403–419.

[115] Bea Xing et al. "Reconfigurable manufacturing system for agile mass customization manufacturing". In: Springer, 2006.

[116] Guo-xin Wang et al. "Formation of part family for reconfigurable manufacturing systems considering bypassing moves and idle machines". In: *Journal of Manufacturing Systems* 41 (2016), pp. 120–129.

[117] Alessia Napoleone et al. "Towards human-centric reconfigurable manufacturing systems: Literature review of reconfigurability enablers for reduced reconfiguration effort and classification frameworks". In: *Journal of Manufacturing Systems* 67 (2023), pp. 23–34.

[118] David Tremblet et al. "Optimizing task reassignments for reconfigurable multi-model assembly lines with unknown order of product arrival". In: *Journal of Manufacturing Systems* 67 (2023), pp. 190–200.

[119] Luca Santoro et al. "UWB-based indoor positioning system with infinite scalability". In: *IEEE Transactions on Instrumentation and Measurement* 72 (2023), pp. 1–11.

[120] Weishan Zhang et al. "LSTM-based analysis of industrial IoT equipment". In: *IEEE Access* 6 (2018), pp. 23551–23560.

[121] Steven J Rigatti. "Random forest". In: *Journal of Insurance Medicine* 47.1 (2017), pp. 31–39.

[122] S Sathiya Keerthi and Chih-Jen Lin. "Asymptotic behaviors of support vector machines with Gaussian kernel". In: *Neural computation* 15.7 (2003), pp. 1667–1689.

[123] Shi Qiang Liu, Jun Chang Zhang, and Rong Zhu. "A Wearable Human Motion Tracking Device Using Micro Flow Sensor Incorporating a Micro Accelerometer". In: *IEEE Transactions on Biomedical Engineering* 67.4 (2020), pp. 940–948. DOI: 10.1109/TBME.2019.2924689.

[124] Sorawit Yaoyuenyong and Suebsak Nanthavanij. "Heuristic job rotation procedures for reducing daily exposure to occupational hazards". In: *International Journal of Occupational Safety and Ergonomics* 14.2 (2008), pp. 195–206.

[125] Jose Alejandro Cano et al. "Disruptive and conventional technologies for the support of logistics processes: a literature review". In: *International Journal of Technology, 12 (3), 448-460.* (2021).

[126] Yangho Park, Jungyub Woo, and SangSu Choi. "A cloud-based digital twin manufacturing system based on an interoperable data schema

for smart manufacturing". In: *International Journal of Computer Integrated Manufacturing* 33.12 (2020), pp. 1259–1276.

[127] Sara Ceschia et al. "The on-demand warehousing problem". In: *International Journal of Production Research* 61.10 (2023), pp. 3152–3170.

[128] Na Liu, Pui-Sze Chow, and Hongshan Zhao. "Challenges and critical successful factors for apparel mass customization operations: recent development and case study". In: *Annals of Operations Research* 291 (2020), pp. 531–563.

[129] Ercan Oztemel and Samet Gursev. "Literature review of Industry 4.0 and related technologies". In: *Journal of intelligent manufacturing* 31 (2020), pp. 127–182.

[130] Tariq Alsahfi, Mousa Almotairi, and Ramez Elmasri. "A survey on trajectory data warehouse". In: *Spatial Information Research* 28 (2020), pp. 53–66.

[131] Ming K Lim, Witold Bahr, and Stephen CH Leung. "RFID in the warehouse: A literature analysis (1995–2010) of its applications, benefits, challenges and future trends". In: *International Journal of Production Economics* 145.1 (2013), pp. 409–430.

[132] Carman KM Lee et al. "Design and application of Internet of things-based warehouse management system for smart logistics". In: *International Journal of Production Research* 56.8 (2018), pp. 2753–2768.

[133] King Lun Choy, George TS Ho, and CKH Lee. "A RFID-based storage assignment system for enhancing the efficiency of order picking". In: *Journal of Intelligent Manufacturing* 28 (2017), pp. 111–129.

[134] Xiulong Liu et al. "RFID and camera fusion for recognition of human-object interactions". In: *Proceedings of the 27th Annual International Conference on Mobile Computing and Networking*. 2021, pp. 296–308.

[135] F Pilati et al. "Indoor positioning systems to prevent the COVID19 transmission in manufacturing environments". In: *Procedia CIRP* 107 (2022), pp. 1588–1593.

[136] Matteo Nardello et al. "Preventing covid-19 contagion in industrial environments through anonymous contact tracing". In: *2021 IEEE International Workshop on Metrology for Industry 4.0 & IoT (MetroInd4.0&IoT)*. IEEE. 2021, pp. 99–104.

[137] Xu Wang and Yusheng Xu. "An improved index for clustering validation based on Silhouette index and Calinski-Harabasz index". In: *IOP Conference Series: Materials Science and Engineering*. Vol. 569. 5. IOP Publishing. 2019, p. 052024.

[138] David L Davies and Donald W Bouldin. "A cluster separation measure". In: *IEEE transactions on pattern analysis and machine intelligence* 2 (1979), pp. 224–227.

[139] Duy-Tai Dinh, Tsutomu Fujinami, and Van-Nam Huynh. "Estimating the optimal number of clusters in categorical data clustering by silhouette coefficient". In: *Knowledge and Systems Sciences: 20th International Symposium, KSS 2019, Da Nang, Vietnam, November 29–December 1, 2019, Proceedings 20*. Springer. 2019, pp. 1–17.

[140] Wenbo Zhang et al. "Modulation format identification using the Calinski–Harabasz index". In: *Applied Optics* 61.3 (2022), pp. 851–857.

[141] David Groombridge. *Gartner Top 10 Strategic Technology Trends for 2023*. 2023.

[142] Eurostat. *Employment by sex, age, occupation and economic activity (from 2008 onwards, NACE Rev. 2) (1 000)*.

[143] Eurostat. *Ageing Europe - statistics on population developments*. 2023.

[144] Dimitrios Chatzoudes and Prodromos Chatzoglou. "Factors affecting employee retention: Proposing an original conceptual framework". In: *International Journal of Economics and Business Administration* 10.1 (2022), pp. 49–76.

[145] Lothar Lieck. *Occupational safety and health in Europe: state and trends 2023*. 2023.

[146] Nikola Suzic and Cipriano Forza. "Development of mass customization implementation guidelines for small and medium enterprises (SMEs)". In: *Production Planning & Control* 34.6 (2023), pp. 543–571.

[147] Pycom. *PyScan*. `https://docs.pycom.io/datasheets/expansionboards/pyscan/`. Accessed: 2023-11-20.

[148] José Guerreiro et al. "Performance Comparison of Low-cost Hardware Platforms Targeting Physiological Computing Applications".

In: *Procedia Technology* 17 (2014). Conference on Electronics, Telecommunications and Computers – CETC 2013., pp. 399–406. ISSN: 2212-0173. DOI: https://doi.org/10.1016/j.protcy.2014.10.204.

[149] Luca De Vito et al. "Measurement System for Operator 5.0: a Learning Fatigue Recognition based on sEMG Signals". In: *2023 IEEE International Symposium on Medical Measurements and Applications (MeMeA)*. 2023, pp. 1–6. DOI: 10.1109/MeMeA57477.2023.10171933.

[150] *Azure Kinect DK Fact Sheet*. https://news.microsoft.com/wp-content/uploads/prod/2019/06/Factsheet-Azure-Kinect-DK.pdf. Accessed: 2023-12-05.

[151] KHE Kroemer and William S Marras. "Towards an objective assessment of the "maximal voluntary contraction" component in routine muscle strength measurements". In: *European journal of applied physiology and occupational physiology* 45 (1980), pp. 1–9.

[152] Kathrine S Andersen et al. "Between-day reliability of a hand-held dynamometer and surface electromyography recordings during isometric submaximal contractions in different shoulder positions". In: *Journal of Electromyography and Kinesiology* 24.5 (2014), pp. 579–587.

[153] Ghada Kareem. "LOWER LIMB SEMG DENOISING USING DAUBECHIES WAVELETS". In: *International Journal of Intelligent Computing and Information Sciences* 23.2 (2023), pp. 145–156.

[154] Baicun Wang et al. "Human Digital Twin in the context of Industry 5.0". In: *Robotics and Computer-Integrated Manufacturing* 85 (2024), p. 102626.